Mechanotransduction of Substrate Stiffness in Endothelial Cell Collective Migration

A Thesis

Submitted to the Faculty

of

Drexel University

by

Adam Charles Canver

in partial fulfillment of the

requirements for the degree

of

Doctorate of Philosophy in Biomedical Engineering

June 2015

Acknowledgements

I would like to thank all the people involved in supporting my pursuit of completing this doctoral thesis dissertation. I have grown professionally and personally more than any other period in my life. During these formidable years, I learned a great deal about how to strive for success as a researcher while also balancing personal and social affairs. My growth during these years will serve as the basis for my future career and personal life, and for that I am sincerely grateful.

First and foremost, I would like to thank Dr. Alisa Morss Clyne, my thesis advisor, without whom none of this would have been possible. She was extremely patient and understanding throughout the highs and lows of my graduate years. She provided an unparalleled level of support. She taught me many intangible skills required of an independent researcher. She will remain an inspiring role model balancing her family with a successful career in academic basic science and engineering. It is my sincere wish that I am able to continue our research relationship through future collaborations. Thank you for everything Alisa!

I would also like to thank the members of my thesis committee: Dr. Kenneth A. Barbee, Dr. Paul A. Janmey, Dr. J. Yasha Kresh, Dr. Mauricio J. Reginato, and Dr. Adrien C. Shieh. I am grateful to each member for serving on my committee since the beginning. I was very fortunate to be among experts in endothelial cell biology, integrin biology, and mechanotransduction, three key areas in my thesis work. Their comments, feedback, and suggestions during each of our meetings were invaluable in tailoring focus of my work.

I am truly thankful to Dr. Jane Clifford, director of the MD/PhD program at the Drexel University College of Medicine. Without her, I would not be here and I am truly grateful to her and the rest of the admissions and advisory committees for providing me the opportunity to

complete my graduate work and ultimately enabling me to help others through a career of medical and research service. She has provided endless support to me and all other MD/PhD candidates, which was particularly helpful as the guidelines for the Biomedical Engineering track were being developed in the early part of my graduate years.

Of course my day-to-day sanity in the lab was kept in check by the awesome colleagues and friends with whom I've had the privilege to work and interact. I would like to first highlight Becky Urbano and Dr. Justin Mathew. Becky and I joined the lab at the same time and were just one year behind Justin. Together, the three of us endured the tumultuous pursuit-of-a-doctorate ride. I greatly benefited from our social interactions outside of lab as well as collaborative efforts in lab, both of which helped keep me enthusiastic and motivated. I would also like to thank Gary Tang, the heart and soul of the lab. I would like to thank other students for their guidance and commiseration: Dr. Danni Figueroa, Dr. Steve Kemeny, Dr. Anant Chopra, Dr. Lenny Urbano, Dr. Pina Lamberti, Dr. Amrit Misra, Aniel Padrino, Nisha Patel, Stephanie Cicalese, Isabel Buckner, Martin Johnson, Christina Furia, Patrick Lenahen, Rabia Qureshi, Claudia Gutierrez, and Tania Cai. Over the years I had the great pleasure of working with fantastic undergraduate students. I would like to thank Olivia Ngo, Soumya Iyer, and Elizabeth Krawczun. Due to arbitrary space limitations, I cannot include a comprehensive list of all people who were important figures throughout my graduate experience. But know that I am extremely grateful to all current and former Drexel Dragons!

Last, but arguably negative first, I would like to thank my family, especially my parents, Dr. Charles and Renee Canver. Without them, I would not exist nor would I have been able to have all the opportunities to reach this point in my education and career. They have been a constant source of love, support, and inspiration, and have always been my first resource for emotional counsel. I would also like to thank my wonderful siblings: Bethany Canver, Matthew Canver, and

John Canver. They provide love and support constantly, like too much actually--enough is enough guys. I love you all!

Table of Contents

List of Tables

List of Figures

Abstract

Mechanotransduction of Substrate Stiffness in Endothelial Cell Collective Migration

Adam Charles Canver

Endothelial damage during life-saving percutaneous angioplasty contributes to re-stenosis rates of nearly 20% within 5 years. Re-endothelialization, the collective endothelial cell migration over exposed extracellular matrix (ECM) and stent struts, can restore a continuous, functional endothelium. During atherosclerotic disease, vascular ECM becomes stiffer. ECM stiffness affects epithelial cell collective migration in other pathogenic contexts. However, substrate stiffness effects on endothelial cell collective migration have yet to be explored.

We developed quantitative computational image processing algorithms for assessing collective migration. We then used these image analysis techniques to measure the effect of substrate stiffness on critical aspects of porcine aortic endothelial cell (PAEC) two-dimensional collective migration: (1) migration distance, (2) directedness, and (3) togetherness. PAEC were seeded on collagen-coated polyacrylamide hydrogels (4-50 kPa) in a 5 mm cloning ring and then allowed to migrate outwards. We found that migration distance increased with substrate stiffness and that there was a concomitant increase in PAEC alignment. We found that decreased togetherness on stiffer substrates led to enhanced proliferation at the migratory interface. We used the specific Rho kinase (ROCK) inhibitor Y27632 to show that ROCK-mediated contractility limited endothelial cell collective migration on soft substrates. We observed that PAEC secrete and remodel fibronectin on collagen-coated substrates. Interestingly, α_5 integrin, but not fibronectin, was important for directed collective migration on stiff substrates.

These findings provide insight into how substrate stiffness affects endothelial cell collective migration. This work will inform how the mechanical properties of tissue and tissue engineered construct could be designed to promote a functional endothelium.

This page was left intentionally blank.

1. Background

1.1. Clinical Relevance and Motivation: Endothelial Injury

Cardiovascular disease, which encompasses hypertension, myocardial infarction, angina pectoris, congestive heart failure, stroke, and congenital defects, affects over 80 million Americans in 2015, which is nearly one third of the United States population.[1] Of those, nearly 16 million suffer from chest pain (angina pectoris) and myocardial infarction (heart attack), clinical complications of coronary heart disease. Deaths related to cardiovascular disease remain the largest contributor to global mortality each year, with more than 750,000 deaths in 2011. The total healthcare cost of cardiovascular disease was over $300 million in 2011 and is predicted to be nearly $1 billion by 2030.[1]

Despite the extensive cardiovascular disease burden, people with cardiovascular disease live longer, more productive lives due to a wide range of available therapies. Balloon angioplasty was developed to open stenotic vessels by inserting a deflated balloon through the site of stenosis using a guide wire, inflate the balloon to force open the arterial walls, and then remove the balloon. This approach has led to re-stenosis rates of 30-60%.[2] To address the shortcomings of recoil and re-stenosis after balloon angioplasty, percutaneous angioplasty with stenting was developed. The procedure is similar, except a cylindrical stent surrounds the balloon and remains locked open at the site of stenosis after balloon inflation. The re-stenosis rates dropped to 16-44%, primarily due to neointimal hyperplasia.[2] Drug-eluting stents were introduced to provide release of anti-proliferative compounds from the stent, reducing re-stenosis rates to below 16%.[2] Despite these advances, there are an estimated 200,000 revascularization procedures performed each year in the United States.[2, 3] Indeed, restenosis rates are nearly 20% within 5 years of drug-eluting stent placement.[4] Vessel bypass surgery provides another surgical approach to reversing

the effects of stenosis. In this procedure, vessels are autologously transplanted from the patient's legs, arms, or trunk and sutured above and below the blockage to provide a parallel route for perfusion. Host vessels typically used include the greater saphenous vein, internal thoracic artery, and radial artery.[5, 6] While percutaneous angioplasty has become the gold standard for single or double vessel coronary stenosis, coronary artery bypass graft surgery (CABG) results in better patient survival for 3-vessel stenoses.[7]

These therapies can resolve many vascular problems, yet each injures the blood vessel in a specific way. The post-stented endothelium has been shown to have elevated levels of dysfunction, including increased permeability and proliferation.[8] Since sirolimus-eluting stents and others aimed at limiting proliferation do not sufficiently reduce re-stenosis rates, other approaches have been explored. Namely, the importance of re-endothelialization after luminal injury has become an important target. The current hypothesis is that if the endothelium can be restored over the site of initial stenosis and stent deployment, it would decrease a chronic inflammatory response that ultimately leads to subsequent re-stenosis.[9] We know little about how the blood vessels heal following therapy, in particular in diseased blood vessels. Since many of these therapies are done in people with hypertension, diabetes, atherosclerosis, and in the elderly—all conditions that alter the mechanical properties of blood vessels—we decided to study how vascular healing is altered by the blood vessel stiffness.

1.2. The Endothelium

Blood vessels are a major component of the circulatory system that transports nutrients, waste, and immune cells to and from all tissues and organs. Arteries transport oxygen-rich blood away from the heart to peripheral tissues and experience the highest intravascular pressure. Arteries are highly muscular to withstand the high intravascular pressures after each stroke of

cardiac contractility. They are made up of a tunica intima, tunica media, and tunica adventitia and have lumen diameters ranging from 4 mm to 10 µm. They withstand intraluminal pressures of 50 to 120 mm Hg under normal physiologic conditions. The outermost adventitia layer contains connective tissue and, in larger vessels, nerves and small vessels called vasa vasorum that perfuse the media layer. The tunica media is muscular with transversely oriented smooth muscle cells that change the lumen cross-sectional area to ultimately control intraluminal volume, pressure, and flow rate. The innermost layer, the tunica intima, contains the endothelium on top of a basement membrane containing elastin fibers. Larger arteries connect to small arteries, then arterioles, which have diameters of ~10 µm. Atherosclerosis occurs in arteries starting in adolescence,[10] and can ultimately result in chronic vascular disease requiring intervention. Disease progression begins with and is prolonged by chronic damage to the endothelial lining, allowing immune cell extravasation and subluminal plaque growth.

The endothelium, a single-layer sheet of endothelial cells that lines the lumen of all blood vessels, serves as the barrier between circulating blood and other tissues. Endothelial cells (EC) have important functions in vascular tone, inflammation & permeability, hemostasis, and new blood vessel growth.

Systemic and endothelial control of vascular tone maintains systemic blood pressure and controls local blood flow. Vasoconstriction and vasodilation are controlled systemically via neurotransmitter release from efferent neurons.[11] Vasodilation is controlled locally via nitric oxide (NO) synthesis and release.[12] Consequently, EC contain high levels of endothelial NO synthase (eNOS).[13] NO causes local vasodilation and is released in response to paracrine signals and shear stress.[14, 15] Vasoconstriction is controlled locally by the absence of NO or other signaling factors, such as endothelin-1.[16] Decreasing vascular resistance via vasodilation increases blood flow to target tissues while increasing resistance elevates systemic blood pressure.

Endothelial cells also mediate vascular inflammation and permeability. Endothelial cells are the first site of injury for many diseases. Endothelial damage induces a local inflammatory response. Vascular endothelial calcium-dependent adhesion (VE-cadherin) junctions are the primary functional intercellular adherens junction protein. VE-cadherin is up-regulated during phases of quiescence to keep the endothelial layer continuous.[17] During phases of endothelial injury or an inflammatory response, VE-cadherin along with other intercellular junctions are antagonized to promote intercellular permeability.[18] This allows space for leukocyte diapedesis, the process of white blood cell (WBC) extravasation from the blood to the inflammation site. In response to endothelial injury, EC release stores of cytokines and adhesion proteins stored in Weibel-Palade bodies, von Willebrand Factor (vWF) and p-selectin, respectively. vWF activates platelets during the early phase of aggregation and clotting. P-selectin is expressed on the luminal membrane of EC to promote diapedesis. In the early stage, WBC form weak interactions with selectins to slow their rolling until they can form stronger bonds with integrins before extravasating between neighboring EC into the subendothelial interstitial area.

EC regulate hemostasis. Hemostasis, or clotting, occurs after a vascular injury that results in blood escaping from the intravascular space.[19] An intact endothelium prevents thrombosis by expressing surface heparan sulfate proteoglycans and thrombomodulin as well as secreting prostacyclins.[20] However, injured or activated EC express p-selectin and vWF just as in the inflammatory response. These activated EC along with activated circulating platelets create a fibrous plug at the site of injury that becomes bolstered by fibrin crosslinking in final blood coagulation.[21] EC also act to limit inflammation by secreting thrombolytic factors, such as tissue plasminogen activator.[22]

EC are essential for ongoing vessel growth and repair during and after development. The processes of making new blood vessels in development and in adulthood are called

vasculogenesis and angiogenesis, respectively.[23] Angiogenesis begins with EC degrading the basement membrane via matrix metalloproteinase (MMP) synthesis and release. Once there is open space, EC begin to migrate outward toward a pro-angiogenic stimulus, such as a vascular endothelial growth factor (VEGF) source. EC migrate along a provisional scaffold primarily consisting of fibronectin. EC form a growing stalk that actively migrates at the tip and proliferates in the following stalk. Once the EC meet another vessel to form the anastomoses, pericytes migrate around the vessel and provide stability and larger collagen fibers to replace the provisional basement membrane.[24]

EC need to proliferate to populate the new vessel during angiogenesis. The level of proliferation depends on how many cell-to-cell contacts are maintained. Contact inhibition of proliferation occurs in over-confluent non-neoplastic cell groups to regulate mitosis. VE-cadherin, in particular, has been shown to be a signaling switch between proliferation and survival in EC. For example, confluent EC with upregulated VE-cadherin expression respond to VEGF by maintaining pro-survival pathways while also inhibiting mitotic signaling. The opposite is true for sparse EC exposed to VEGF.[25-27] It has been suggested that contact inhibition occurs via β-catenin signaling. β-catenin is complexed with VE-cadherin after it is synthesized and as it is trafficked to the membrane. β-catenin also binds to α-catenin, which tethers to actin fibers. Therefore, in a cell with well-maintained VE-cadherin-catenin complexes, the cell-to-cell contacts are physically linked to the cytoskeleton and β-catenin is sequestered to the membrane. As these complexes become internalized and degraded in response to phosphorylation of VE-cadherin and β-catenin, free β-catenin translocates through the cytosol to the nucleus where it complexes with T cell factor/lymphoid enhancer factor (TCF/LEF) to promote mitosis and differentiation.[28-31]

1.3. Endothelial Cell Migration

Endothelial cell (EC) migration has been extensively studied because it is important in many developmental and pathologic processes. In development, EC migrate during vasculogenesis to build more vessels to perfuse organs and peripheral tissues. In adulthood, EC migrate during angiogenesis, which is required for wound healing and to make collateral connections to restore perfusion after infarction. In addition, EC migration is essential for re-endothelialization after luminal injury and vascularizing tissue-engineered structures.

Single cell migration begins by cells probing the environment. Lamellopodia are small projections of the cell membrane and filopodia are longer and thinner membrane projections. Cells polarize with lamellopodia and filopodia on the front edge and a trailing edge behind. Cellular motility depends on the ability of the cell to organize actin filaments and pull against them using the myosin contractility apparatus. In addition, cells need to be able to make new contacts on their surface at the front edge while turning over cell contacts at the trailing edge. Therefore, cell migration is an imbalance between focal adhesion (FA) synthesis and disassembly, leading to cell polarity and net movement. It has been shown that FA disassembly is mediated by focal adhesion kinase (FAK) through both myosin light chain kinase (MLCK) and the Rho/Rho-associated Kinase (ROCK) pathways.[32] In keratinocytes from FAK-null mice, FAs were well-maintained, limiting cell motility.[33] However, endothelial cells from FAK-null mice had only diminished survival, impaired lamellopodial formation, and diminished polarity without any differences in proliferation and single-cell random migration.[34] Therefore, the role of FAK in regulating FA during single-cell migration differs between cell types.

However, many cells migrate collectively. Collective migration is defined as a group of cells (1) being directed toward a similar target, (2) being physically linked throughout the movement, and (3) depositing and remodeling the underlying extracellular matrix (ECM).[35-37]

Collective migration has been demonstrated to occur in many non-neoplastic tissue movements, including development, angiogenesis, and epithelialization in wound closure. When cells lose the restrictions of maintaining cell-to-cell contacts, non-collective migration often occurs in epithelial-to-mesenchymal transition (EMT),[38] a mode of single-cell migration that occurs in metastatic neoplasms.

Whereas many research studies have been conducted to study the mechanics of individual cell migration, less work has been done to elucidate the mechanisms underlying how cells collectively migrate when forming or repairing tissue. The conventional theory is that cells in direct contact with the free interface (i.e. with a free front edge) have increased sensitivity to chemotactic molecules, such as growth factor and cytokine gradients. These are called "tip cells" and are phenotypically distinct from the "follower cells."[39-42] Follower cells are completely surrounded by neighboring cells, causing them to be desensitized to the actions of pro-migratory factors.[25] In response to specific growth factors like vascular growth factor (VEGF) and fibroblast growth factor 2 (FGF2), tip cells respective membrane-bound tyrosine kinase receptors induce the expression of Delta-like ligand 4 (DLL4) and Jagged 1.[35, 40, 41, 43-45] Both of these are expressed at the rear end of the cell and bind to Notch receptors on neighboring follower cells. In the follower cells, Notch signaling inhibits VEGF receptor signaling, thus decreasing follower cell sensitivity to VEGF and preventing follower cells from expressing an actively migrating "tip cell" phenotype. The tip cells are responsible for responding to chemokine gradients, developing membrane ruffles and protrusions called lamellopodia and filopodia, respectively, and degrading ECM via matrix metalloproteinases (MMPs). The follower cells are responsible for producing and depositing ECM as well as proliferation.[35, 40, 41, 43-45] Thus, the theory states that tip cells respond to the environment and help direct the follower cells, which passively follow because they are being "pulled" along.

More recently, research groups have introduced the idea that collectively migrating cells may be less dependent upon cell-cell cues than previously hypothesized. Bindschadler, *et al*. showed that confluent fibroblasts expanded as a sheet in response to the removal of their confinement.[46] The findings suggest that fibroblasts move as connected single cells within the monolayer sheet in a wound healing model. The group further suggested that the driving force for "collective" migration, just as with proliferation, is an inverse function of cell density. This study confirms an earlier study by Farooqui and Fenteany, which showed that MDCK epithelial cells within the migratory front extend "cryptic" lamellopodia beneath cells closer to the interface.[47] However, Ng, *et al*. showed that when myosin II contractility or cadherin complexes were impaired, epithelial cells were less coordinated and moved slower within the migratory front.[48] This suggests that single cell motor apparatuses, such as myosin II, as well as cell-cell apparatuses, such as stable cadherin complexes, are essential for collective migration. However, we do not yet understand how these theories apply to EC.

1.4. Endothelial Cell Mechanotransduction

Endothelial cells (EC) sense mechanical stimuli, especially substrate stiffness, via integrins. Integrins are transmembrane cell receptors made up of one α and one β subunit. There are 18 α and 8 β subunits that combine to form 24 different receptors, each with different specificity to their extracellular matrix (ECM) ligands.[49] For example, $\alpha_5\beta_1$ and $\alpha_2\beta_1$ have high affinities for fibronectin and collagen, respectively. Upon binding to the ECM, integrins undergo a conformational change and initiate intracellular signaling. As the substrate stiffens, EC aggregate integrins in groups at focal contacts.[50] EC pull on the substrate at these focal contacts, which then further recruits and activates integrins until large focal adhesions (FA) form. Integrins form catch bonds, meaning they increase in strength in response to tension. To accomplish this, a cryptic

binding site in talin becomes exposed under tension allowing vinculin to bind and stabilize the FA.[51, 52] Thus, integrin affinity is tunable based on the adaptor protein availability.[53]

FA are an important signaling apparatus. For example, EC require cell-ECM adhesion in order to survive, which implies that integrin signaling promotes cell survival.[50] At the FA site, focal adhesion kinase (FAK) forms a complex with Src, a tyrosine kinase.[54] The FAK/Src complex autophosphorylates to further phosphorylate and activate downstream signaling molecules. FAK/Src activates the PI3K/Akt survival pathway[54, 55] and the Ras/MEK/ERK proliferation pathway.[54, 56] The mechanical stiffness of the substrate results in strong, well-established FA, which then activate RhoA kinase, a small GTPase.[57] RhoA kinase activates Rho-associated protein kinase (ROCK), a serine/threonine kinase. ROCK has dual functions to activate myosin light chain (MLC) directly and inhibit MLC phosphatase (MLCP), leading to indirect MLC activation. MLC kinase (MLCK), a serine/threonine kinase that can be activated by FAK/Src,[58, 59] activates MLC. Activated MLC moves along polymerized actin filaments to increase cell contractility. EC that have high intracellular tension develop actin stress fibers, which are bundles of actin filaments stretching across the cell.[60] Therefore, one of the primary consequences of increased substrate stiffness is increased cell contractility.

Substrate stiffness is measured by its elastic modulus and ranges from 10 Pa to 300 MPa in human tissue.[61] Fat and brain tissue are soft, in the 10-500 Pa range. Liver and kidney tissue are ~2 kPa stiffness and that stiffness can double after pathologic fibrosis. Skeletal muscle is in the 20-150 kPa stiffness range. The stiffest tissues in the body are tendon, ligaments, and bone which are in the MPa to GPa stiffness range. EC experience the stiffness of their basement membrane in larger vessels or surrounding organs for capillaries. Vessel stiffness progressively increases with aging and vascular disease.[62, 63] After stenting, it is important that EC re-endothelialize the lumen by covering up the stent struts. Stents are made of metal or other polymers that are very stiff to

maintain luminal patency after implantation. In order to study the cell response to substrate stiffness, research groups use polyacrylamide (PA) gels, an inert material historically used in gel electrophoresis. PA gels were first introduced as cellular substrates in 1997 by Drs. Pelham and Wang.[64] A range of mechanical stiffnesses of 20-150,000 Pa can be achieved based on the ratio of acrylamide to bis-acrylamide.[65, 66] PA gels are nanoporous, meaning micron-sized cells are unable to migrate through the gel.[65]

Substrate stiffness has been shown to affect a variety of cellular functions and signaling.[67-69] Cells tend to spread more on stiffer substrates, which decreases apoptosis.[70] Fibroblasts make stress fibers on substrates with stiffness greater than 1.6 kPa, but not below that threshold.[71] Fibroblasts also appear to mimic the stiffness of their substrate on relatively soft substrates below 5 kPa, but not above that.[72] Sparsely seeded aortic endothelial cell spreading varied with stiffness, showing round morphology on 0.18 kPa substrates and elongated morphology on stiffnesses above 2.9 kPa. However, these morphological differences were lost once a confluent monolayer was established.[71] Substrate stiffness has been shown to be a switch for adult neural stem cell differentiation. When cultured on substrates with elastic moduli below 1 kPa and above 7 kPa, neuronal and oligodendrocyte differentiations were favored, respectively.[73] A similar substrate stiffness switch is seen in hepatic stellate cells, which become myofibroblasts on stiff substrates ($E > 8$ kPa) and remain undifferentiated on compliant substrates ($E < 1$ kPa).[74] Mesenchymal stem cells (MSC), multipotent cells that are precursors for neurons, muscle, and connective tissue, also differentiate in a stiffness-dependent manner. MSC become neuron-like, muscle-like, and bone-like in *in vitro* models when substrate stiffnesses are below 1 kPa, between 8 and 17 kPa, and above 25 kPa, respectively.[48] Substrate stiffness can affect cellular sensitivity to exogenous signals, ultimately affecting cell function. For example, human pulmonary artery EC and human

lung microvascular EC show more actin stress fibers in response to thrombin when cultured on 42 kPa substrates compared to 0.55 kPa substrates.[75]

Cells within a monolayer experience two primary forces: (1) cell-to-ECM traction forces and (2) cell-to-cell forces. In a migrating monolayer, these forces are often opposing as traction forces develop at the front end of the cell in the forward direction and cell-to-cell forces develop at the rear end of the cell in the backward direction.[76, 77] If they are in balance, then the cell most likely has no net displacement or polarity. In response to a stiffer ECM substrate, the front-end FA are bolstered with more integrin recruitment, aggregation, and activation. The same occurs with cell-to-cell adhesions under increasing force;[78] cadherin-catenin complexes become stronger with the recruitment of vinculin to an exposed binding site on β-catenin.

Epithelial cell contractility during collective migration has been shown to be substrate stiffness-dependent.[48] Epithelial cells cultured on 65 kPa substrates had much higher levels of phosphorylated myosin light chain compared to epithelial cells on 3 kPa substrates. Epithelial cells also tended to be more aligned with the migration direction and be more coordinated with neighboring cells on stiffer substrates.[48]

There has been recent interest in how substrate stiffness is sensed in a confluent monolayer, as in the case of collective cell migration. Using traction force microscopy (TFM), research groups have been able to probe the forces cells experience based on input from their substrate's mechanical properties.[79, 80] Trepat, *et al.* studied the traction forces (i.e. forces between cells and their substrate) and cell-to-cell forces within cellular monolayers. They described plithotaxis, or the tendency of cells to migrate along the local orientation of maximal normal stress and equivalently minimal shear stress, as shown in breast cancer cell lines.[81, 82] They describe it as a tug-of-war model between propellant traction forces and resistive cell-to-cell forces.[77, 83] Trepat, *et al*. further challenged the conventional theory of collective migration by

showing evidence that forces are not greatest at the migratory front and that cells farther from the migratory interface have greater traction forces.[77] This interesting finding suggests that "tip cells" are not simply pulling the "follower cells" along, but that cells may be pushing interface cells forward.[47, 84]

1.5. Extracellular Matrix and Integrins

Extracellular matrix (ECM) is a network of large structural proteins that is found underneath endothelial cells (EC). The most common ECM protein is collagen, a fibrillar structure of three intertwined α chains. A great body of research has focused on understanding how cells function based on the composition and micro- and nano-structure of the surrounding ECM. This has been important for understanding pathologies as well as recreating "ideal" structures and environments for tissue engineering therapeutics. Fiber orientation is an important factor affecting cell direction and speed during migration.[85] In particular, collagen fibers that are aligned perpendicular to a tumor basement membrane result in greater breast carcinoma cell invasion than fibers aligned parallel to the basement membrane.[86] Using micropatterning techniques, collagen fibers were oriented in parallel or randomly. EC stretched more in the direction of the parallel, oriented fibers while EC on randomly-oriented fibers were more rounded.[87] Another group varied the density of micropatterned grooves, finding that fibroblasts elongated parallel to the grooves.[88] They further showed that fibroblasts migrated fastest when the groove density was at an intermediate level, with groove widths of 5.6-6.3 μm.[88]

Fibronectin is secreted by EC[89] and is polymerized into larger fibers. Fibronectin is a provisional matrix protein with increased secretion during migration.[89-92] It has the greatest affinity to $\alpha_5\beta_1$ and $\alpha_V\beta_3$ integrins and can also bind to collagen.[93-95] Although both integrins are said to bind primarily to fibronectin, they serve different purposes in fibroblasts. Whereas $\alpha_5\beta_1$

integrins can withstanding high forces,[96] $\alpha_V\beta_3$ integrins are generally weaker, frequently going in and out of binding to fibronectin. Thus there is evidence that $\alpha_5\beta_1$ integrins are primarily for attachment and $\alpha_V\beta_3$ integrins are for mechanotransduction, probing the stiffness of the local environment.[97] Furthermore, $\alpha_V\beta_3$ integrin has been shown to exist primarily in developing focal contacts that are at the cell edges during migration. This is due to much quicker integrin recycling of the $\alpha_V\beta_3$ integrin compared to the $\alpha_5\beta_1$ integrin.[98] When cells stretch, adhered fibronectin also stretches, revealing cryptic binding sites for collagen and other fibronectin fibers.[99, 100] Thus, the stiffness of the underlying substrate, which affects intracellular tension, affects the availability of certain fibronectin binding sites.[101-103] Fibronectin matrix assembly has been shown to be enhanced on stiff and inhibited on soft substrates.[104] Fibrillogenesis begins at peripheral focal contacts and adhesions at sites of integrin clustering. As cells pull on the substrate in a stiffness-dependent manner, fibronectin fibers grow toward the center of the cell in the direction of cell tension.[105]

Polyacrylamide hydrogels used as mechanically-tunable substrates are chemically inert. In order to allow cellular adhesion, the PA surface must be functionalized with a protein.[64, 65] Most often an extracellular matrix (ECM) protein is chosen, such as collagen, fibronectin, or laminin. These proteins comprise the native stroma and basement membranes in many tissues and are obvious choices for cellular adhesion.[106] Pelham and Wang showed that the surface chemistry and binding sites of the protein layer do not significantly vary with substrate stiffness.[64] The final result is a protein-coated PA gel with a particular stiffness that can be easily measured by atomic force microscopy (AFM).

1.6. Image Analysis

High resolution microscopy has been invaluable in providing spatial information about collectively migrating tissues. Effective, robust analysis has lagged behind researchers' abilities to generate images. Regardless of the approach, be it manual cell tracing and counting or highly automated computational algorithms, there is a dissatisfying level of detail about how measures were specifically made in methods sections of biological and biomedical publications. This lack in method transparency limits the conclusive power and reproducibility of findings. Open-source algorithms are required for understanding and trusting new measurements taken from the large banks of images that researchers are able to produce.[107]

Historically, the image analysis approach has been to use fluorescent signal intensity as a semi-quantitative measure. However, fluorescent signal intensity is subject to many variables making it a weak measurement for making robust and convincing conclusions. A preferred approach is through extraction of features such as the area, aspect ratio, and orientation of cells; subcellular or extracellular components; or multicellular clusters. It is also often important to count the number or shape of a particular feature, such as cellular protrusions. Human error and bias often taint manually collected measurements, and thus computationally-assisted methods have become more common to standardize the error and allow for more consistent and reliable measurements. For single-cell analysis, measuring cell morphology is relatively straight-forward. However, to accurately measure cell morphology in confluent monolayers is much less trivial and remains an on-going challenge due to low intercellular contrast, even with the help of intercellular fluorescent markers.

Studying collective migration, which is inherently subject to this analysis problem, has been difficult and standardized methods have yet to be established. Lee, *et al*. tracked nucleoli of epithelial cell sheets using adapted MATLAB algorithms to ultimately report cell velocities within

the migrating sheet.[108] Ng, *et al*. describe in great detail MATLAB algorithms for measuring wound edge advancement, nuclear detection and tracking, velocity, persistence, cell-pair separation distance, polarity, and lamellopodial directionality. However, individual cell morphology was conducted by hand-tracing a select number of cells.[48] Bindschadler, *et al*. show segmentation of sub-confluent fibroblast monolayers using a MATLAB-based approach.[46]

1.7. Objective, Hypothesis, and Organization

While a great deal of knowledge exists about how substrate stiffness affects cell shape, signaling, and function, mechanisms for many of these processes are still lacking. In particular, how substrate stiffness affects endothelial cell collective migration in the contexts of angiogenesis and endothelialization remains unclear. Gaining a better understanding of how substrate stiffness affects endothelial cell collective migration will provide crucial insights into potential therapies for re-endothelialization after endothelial injury and inform approaches to vascularization of tissue engineered constructs. **The objective of this thesis is to examine how substrate stiffness affects endothelial cell collective migration.** The underlying hypotheses for this thesis are:

- Computational algorithms reduce human error and bias in measuring morphology of confluent cell monolayers, and allow for standardized, high-throughput image processing and subsequent analysis.
- Endothelial cells collectively migrate farther and are more aligned with the migration direction on stiffer substrates due to their enhanced ROCK-mediated contractility.

This thesis is organized into three more chapters. In chapter 2, we discuss the development of the computational methods used to quantify aspects of collective migration from imaging the migratory front. In chapter 3, we discuss how substrate stiffness affects collective

endothelial cell migration through differential dependencies on the α_5 integrin and ROCK contractility. In chapter 4, we discuss preliminary findings about how substrate stiffness affects the endothelial response to exogenous stimuli, including pro-inflammtory cytokines as well as EndMT-inducing and pro-migratory growth factors. Lastly, in chapter 5 we discuss the conclusions and overall significance of this work.

2. MATLAB Quantification Methods For Measuring Collective Migration

2.1. Introduction

Collective cell migration requires cell groups to be oriented toward a common goal (i.e. directed) and maintain cell-cell contacts (i.e. together) as they move through or across a tissue.[35] Collective migration has recently been shown to be important in the context of physiology and pathophysiology, specifically in angiogenesis, wound healing, and metastasis. It is clear that it is no longer sufficient to merely measure how far cells within tissues migrate, but *how* they migrate far.

To understand collective cell migration processes, both when and where events happen within the migrating tissue front must be considered. Immunofluorescence imaging has become a staple for such studies, producing detailed, high-resolution images for qualitative analysis of both living and fixed cells. However, quantitative image analysis for rigorous feature comparison among samples has fallen by the wayside due to four main challenges.

The first challenge is that image analysis largely remains semi-quantitative because it relies on pixel intensity. Unfortunately, pixel intensity is highly variable due to non-uniformity in the immunolabeling process and user manipulation of camera exposure settings. In addition, pixel intensity can be significantly affected by photobleaching and may become contaminated by autofluorescence and spectral bleed-through. Currently, the primary method for addressing pixel intensity variability is by normalizing fluorescent intensity to a control within the image.

The second challenge is that many feature extraction approaches can currently only be achieved manually. For example, morphometrics (shape measurements) can be more informative and reliable measures than pixel intensity. However, image morphometrics typically involve manually tracing cells or their features. Not only is this extremely tedious and time-consuming, it is highly susceptible to human error and bias.

The third challenge is that segmentation of confluent cell monolayers is non-trivial. Low contrast among neighboring cells makes it especially challenging to distinguish where one cell ends and another cell begins with the human eye much less computationally. Inconsistency among image inputs and desired measurements pose additional problems for creating an algorithm that can be applied to any image. While parameters such as cell area are commonly measured in single cells, even such seemingly simple measurements are extremely challenging in confluent cell monolayers.

The fourth challenge is that image quantification procedures are rarely transparent. While it is becoming less acceptable to publish results without clearly describing how images were acquired and analyzed, many papers do not describe image analysis techniques in enough detail that they can easily be reproduced by others conducting similar research. Without reproducible application-specific algorithms, data comparison across different published experiments is impossible. By creating reliable, standardized, and transparent image quantification tools as collective cell migration is emerging as a field, we can greatly enhance the conclusive strength of research coming from a wide array of research laboratories.

In this chapter, we present novel, semi-automated approaches to overcome these challenges and quantify a variety of cell features within collectively migrating 2D cell monolayers. Using common biomolecular fluorescent markers, we describe techniques to quantify spatial changes in average collective migration distance, nuclear orientation, subcellular compartmenalization, cell morphology, interface roughness, and extracellular matrix protein structure. Although our group's application focus is on collective cell migration, these high-throughput methods can be adapted to a wide array of cell image types and applications.

2.2. Methods

2.2.1. Cell Culture

Porcine aortic endothelial cells (PAEC) were isolated by the collagenase dispersion method.[109] PAEC from passages 5 to 8 were used for all experiments. Cells were cultured in Dulbecco's Modified Eagle Medium supplemented with 5% fetal bovine serum, 2 mM L-glutamine, 100 U/mL penicillin, and 100 µg/mL streptomycin. Dishes were incubated in a humidified incubator at 37°C and 5% CO_2. Medium was changed every 2 days.

2.2.2. Cage Migration Assay

A cage assay based on previous studies[110, 111] was modified for our experiments (Figure 2.1).

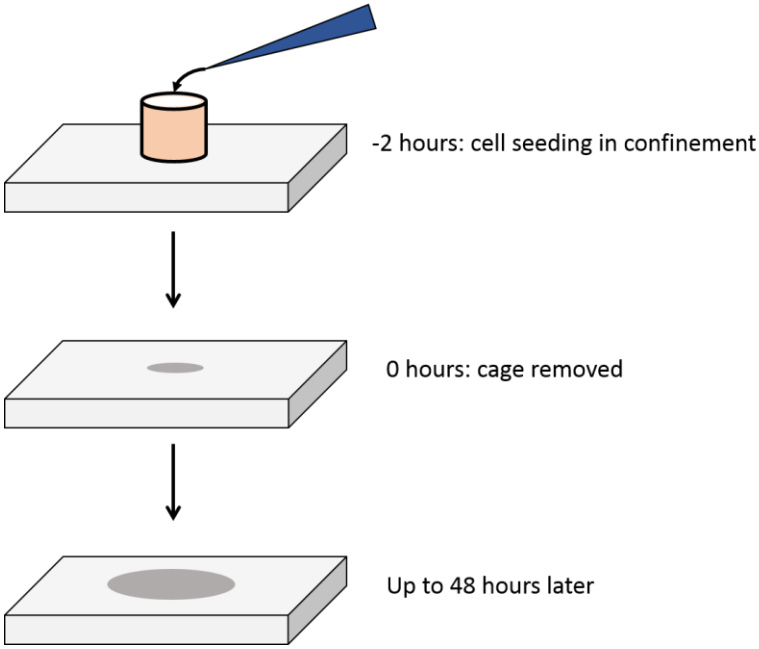

Figure 2.1: The cage assay schematic was performed on 22x22 mm coverslips. Endothelial cells were seeded in 5 mm cages, which were removed after 2 hours (time zero). Cells were then allowed to migrate radially outwards for up to 48 hours.

PAEC were detached from the dish with 0.05% trypsin-EDTA, after which the trypsin was quenched with growth medium. Cell number was quantified using a Z1 Coulter Particle Counter. The cell suspension was pelleted, supernatant was aspirated, and fresh growth medium was added such that the final cell concentration was 300,000 PAEC/mL growth medium. Two polystyrene hollow cylindrical cages (6 mm diameter) were placed on top of the 22x22mm glass coverslips in 6-well plates. The cages were separated far enough from each other to prevent direct or paracrine interaction. 100 µL of the cell suspension was added to each ring, resulting in 30,000 PAEC added to each cage. The samples were incubated for two hours at 37°C and 5% CO_2 to allow confined cell attachment, after which the cages were removed and 3 mL growth medium was added to the well to completely cover the samples. The time of cage removal was considered to be time zero, at which point migration was allowed to start. PAEC were allowed to migrate radially outward from 0-48 hours.

2.2.3. Immunocytochemistry

For fluorescent labeling, samples were fixed with 4% paraformaldehyde (PFA) for 15 minutes at 4°C. Samples were rinsed with phosphate buffered saline (PBS) and permeabilized with 0.1% Triton X-100 for 5 minutes at room temperature. Samples were then rinsed and blocked with 1% bovine serum albumin (BSA) for 15 minutes at room temperature. Primary antibody solutions of mouse anti-fibronectin (1:250), mouse anti-β-catenin (1:250), rabbit anti-VE-cadherin (1:250), rabbit anti-phospho-MLC (Thr18/Ser19), and rabbit anti-phospho-FAK (Tyr397) were diluted in 1% BSA. Samples were incubated with primary antibody overnight at 4°C. After thorough rinsing, samples were incubated with secondary antibodies goat anti-mouse IgG AlexaFluor® 488 (1:250) or goat anti-rabbit IgG AlexaFluor® 633 (1:250), rhodamine phalloidin (1:100, F-actin label), and Hoechst 33342 (1:2000, nuclear label) in 1% BSA. After 1 hour at room temperature, samples were

rinsed with high-volume PBS washes and stored in PBS at 4°C. Samples were mounted onto glass slides with a 50:50 glycerol:PBS solution.

2.2.4. Imaging

Optical resolution is defined as the shortest distance between two points in a sample that can still be distinguished as separate entities.[112] For quantification methods that required minimal optical resolution (migration distance, nuclear orientation, and cell morphology), images were taken using an Olympus IX81 inverted fluorescent microscope to reduce acquisition time. SPOT Advanced software was used to acquire the images. High-resolution confocal images were taken for fibronectin analyses using an Olympus IX81 inverted confocal microscope. Z-stacks were taken at 0.5 µm steps throughout the sample thickness using Olympus Fluoview F1000 software. All images were taken using the 405 nm (blue), 488 nm (green), and 543 nm (orange-red) detection wavelengths.

2.2.5. Image Pre-Processing

Raw images were imported into MATLAB for pre-processing to consolidate Z-stacks (if applicable), remove background noise, and apply consistent contrast adjustments to the entire set of images within an experiment.

For confocal images captured with Olympus software, each file was split into separate layers within the z-stack image. Within each layer, the image was split into three channels: red, green, and blue. For measurements based on features and not intensity, the stacks were flattened by taking the maximal projection along the z-axis. In other words, the highest intensity value was chosen among all layers in the z-stack for each pixel (Figure 2.2A-C).

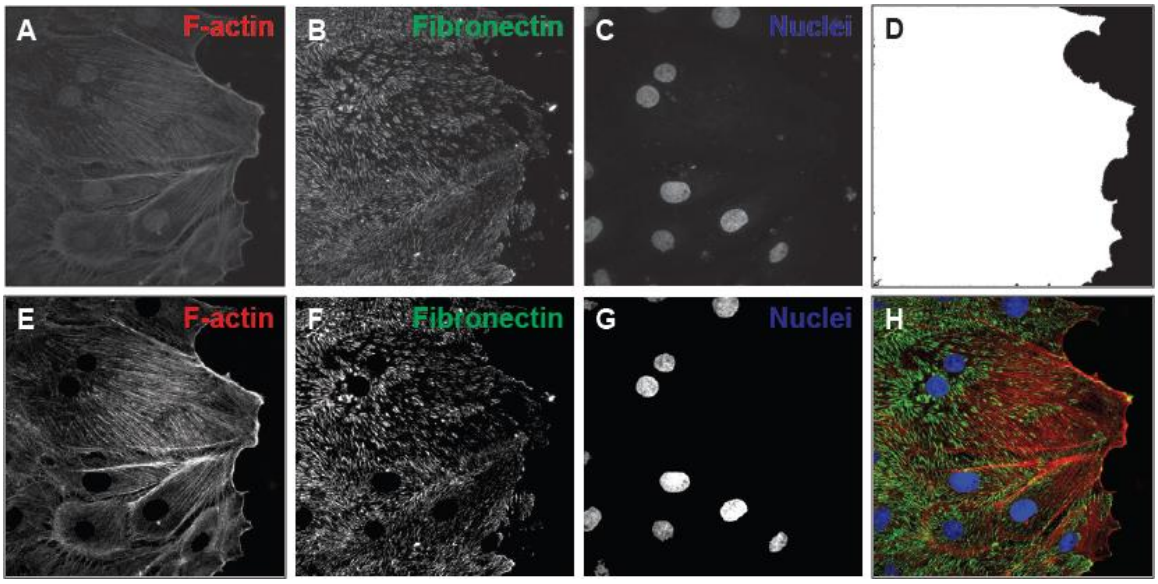

Figure 2.2: Background noise and artifacts were removed as part of image pre-processing. (A-C) The maximal z-axis projection was selected from scanning confocal microscopy layers for each color channel. (E-G) Contrast was adjusted after filtering. Nuclei were removed from non-nuclear channels. F-actin was thresholded and holes were filled in. Debris and artifacts were subtracted out of non-cell areas in the other channels. (H) The three channels were merged into a single RGB image for the final output.

Debris and artifacts were subtracted out of images with known areas of absent cells, such as past the migratory front interface. To accomplish this, the F-actin channel was thresholded using the GRAYTHRESH function, a built-in implementation of Otsu's optimized thresholding algorithm.[113] Briefly, Otsu's algorithm reduces a grayscale image to a binary image by assuming that the image contains two classes of pixels: foreground and background. The algorithm calculates a threshold level between these two pixel classes that minimizes the variance within the class (or maximizes the variance between the classes). Once the threshold was chosen, the built-in IM2BW function was used to apply the threshold to the image, making it a binary image. Holes were filled in the binary image using the built-in IMFILL function and small objects were excluded from the binary image by removing objects below a pixel area threshold set at 1000 using the BWAREAOPEN function (Figure 2.2D). This binary image was then used to subtract debris and artifacts from the non-cell area in the original fluorescent images (Figure 2.2E-G).

Background noise was then removed from the original fluorescent images using a Gaussian filter followed by a median filter (Figure 2.2E-G).[114] The Gaussian filter smoothed the image by taking the weighted average of the nearest pixels. The Gaussian filter was implemented using the built-in FSPECIAL function with a size and standard deviation of 25x25 pixels and 50, respectively. This was fed into the built-in IMFILTER function. The filtering was repeated on the image 50 times to effectively decrease background noise. The median filter, which decreases salt and pepper noise, was implemented using the built-in MEDFILT2 function with a size of 3x3 pixels. The three channels were merged into one RGB image using the built-in CAT function (Figure 2.2H). Unless otherwise noted, these RGB images were used as input for all the following post-processing algorithms (Figure 2.3).

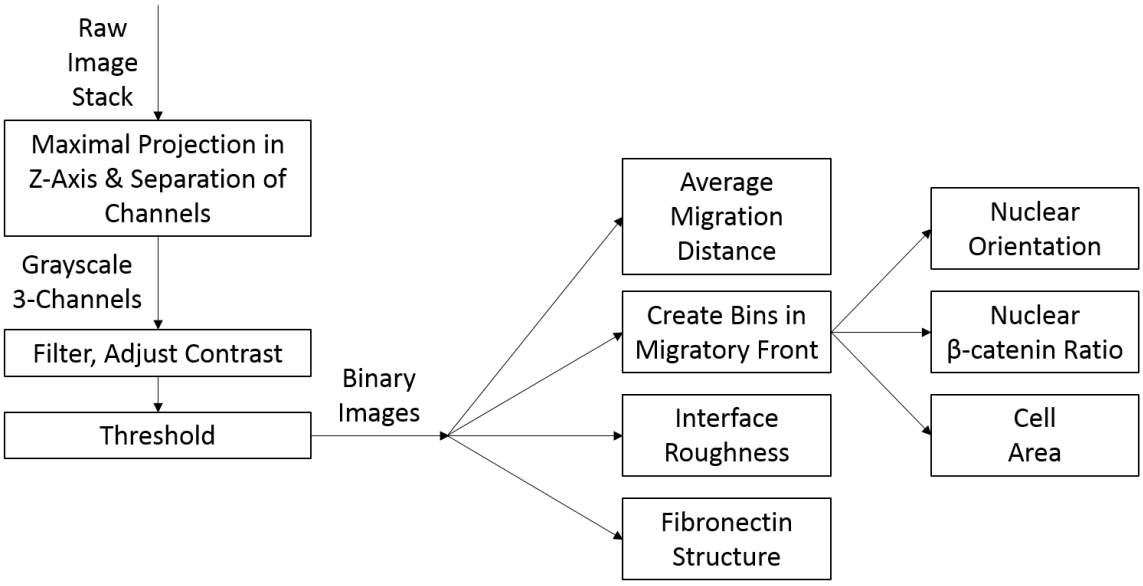

Figure 2.3: Image processing algorithm. The algorithm workflow begins with raw confocal microscopy z-stacks. Each image is pre-processed in a similar way, after which binary images area analyzed for specific morphological features. Each algorithm is tailor-made, but adaptable, for specific measurements.

2.2.6. Statistics

All experiments were done in duplicate or triplicate. Unless otherwise noted, data are represented as mean ± standard error of the mean in order to better reflect the precision of the mean. The mean ± standard error of the mean were calculated from averages of measures from 5+ images per sample from 2+ samples per condition. One-way ANOVA and post-hoc testing (least significance difference) were used to compare metrics across substrate stiffnesses. # denotes p-values less than 0.05, * denotes p-values less than 0.01, ** denotes p-values less than 0.001, and "n.s." denotes a "non-significant" difference.

2.3. Results

2.3.1. Average Migration Distance

Cells in the cage assay migrated radially outward, allowing us to measure the average migration distance (Figure 2.3). This analysis relies heavily on entire-cell labeling. For our studies, we labelled F-actin, but other markers may be suitable. Images were captured using a 4x magnification objective on a fluorescent microscope. To define the cellular region, five to eight images of each sample were manually stitched together by aligning common features using Adobe Photoshop. By calibrating the pixel:length ratio of the microscope 4x objective (3.68 μm/pixel), a yellow circle the size of the original cylinder was positioned in the image center (Figure 2.4A,D). An image consisting solely of the yellow circle was additionally saved.

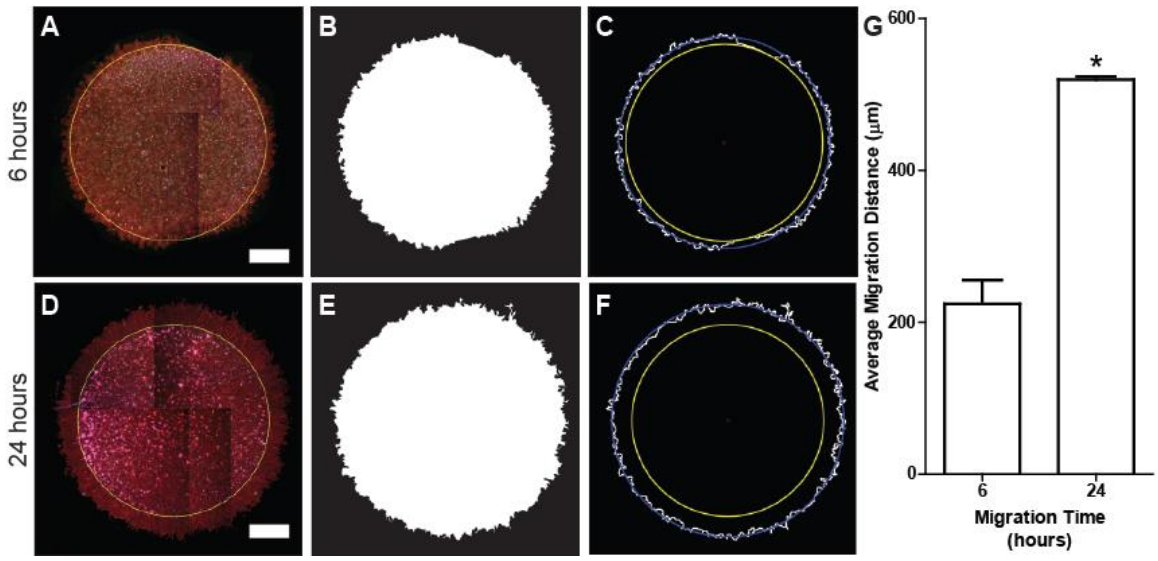

Figure 2.4: Collective migration distance was quantified from the cell outline in the cage assay. (A,D) Samples were fixed and labeled for F-actin (red). 5-8 images were manually aligned in a mosaic to reconstitute the full cell area. The images were adjusted and filtered to enhance contrast prior to thresholding. The yellow circle represents the cage location. (B,E) The composite images were thresholded using Otsu's method to create a binary cell area image. (C,F) The final analysis output showing the original cage position in yellow, the migrating front outline in white, and the average migration distance in blue. (G) The reported value was the difference in radius between the blue and yellow circles. Scale bar = 1000 μm. * $p < 0.01$.

The composite cell area images were imported into a custom MATLAB script that performed thresholding[113] and debris removal as previously described to create a composite binary image (Figure 2.4B,E). Once the binary image was approved by the user, the binary cell area image and the initial cylinder position image (yellow circle) were imported into a second custom MATLAB script. A one-pixel thick outline of the binary cell area was extracted using the built-in BWPERIM function (Figure 2.4C,F). The initial cage center was found by filling in the yellow circle (built-in IMFILL function) and finding its centroid coordinates (built-in REGIONPROPS function). The Euclidean distance between this centroid and each pixel along the cell area outline was calculated. These distances were averaged to determine the average collective migration radius (blue circle). The average collective migration distance was calculated as the difference between the blue circle radius and the yellow circle radius (Figure 2.4G). Using this method, we showed

that average collective migration distance more than doubled between 6 and 24 hours of migration time. This method assumes that the collective migration is uniformly radial, as we observed in our experiments.

2.3.2. Binning Images for Spatial Comparisons

A critical aspect of collective migration quantification is cell heterogeneity as a function of distance from the migratory interface. Whereas cells at the interface have free edges and are able to spread and probe the microenvironment, cells farther back into the tissue are surrounded on all sides by other cells and have different characteristics.[36, 39, 115] It was therefore necessary to develop a method to divide confluent monolayer images into bins so that measurements could be compared spatially. This method is independent of image orientation, which decreases image pre-processing requirements for radially migrating samples and may also ease its adaptation to other biological assays.

A custom MATLAB script was developed to determine the global migration direction within the image. First, a line was drawn perpendicular to the global migration direction by connecting the two furthest F-actin points at the migrating front edges. The slope and y-intercept of this line were calculated. A second line perpendicular to the first line (parallel to the global migration direction) was then drawn. This line was divided into two segments: the segment passing through the cell area (defined by having primarily non-zero F-actin fluorescent intensity) and the segment passing through empty space past the migrating front (defined by having primarily zero F-actin fluorescent intensity). The migratory vector was chosen as pointing from the cell area towards the empty space along the perpendicular line. This global migration angle was defined as the angle of the migratory vector relative to the x axis. This angle was then used to normalize the future alignment measurements.

The next step was to create bins so that measurements could be spatially compared. To accomplish this, the y-intercept of the line perpendicular to the global migration direction was iteratively increased or decreased in the migratory direction until the sum of the pixels from the F-actin channel along the line was zero, i.e. until the line was tangent to the most advanced cell (yellow line in Figure 2.5C,F). Parallel bin lines were then added a fixed width apart until they reached the end of the cell area (white lines in Figure 2.5C,F). Here, we created lines that were 100 µm apart, but any distance can be selected.

For subsequent analyses, bins were generated as the negative of the parallel line mask (Figure 2.5B,E). The pixels within each bin were used to extract features within that bin for any other channel.

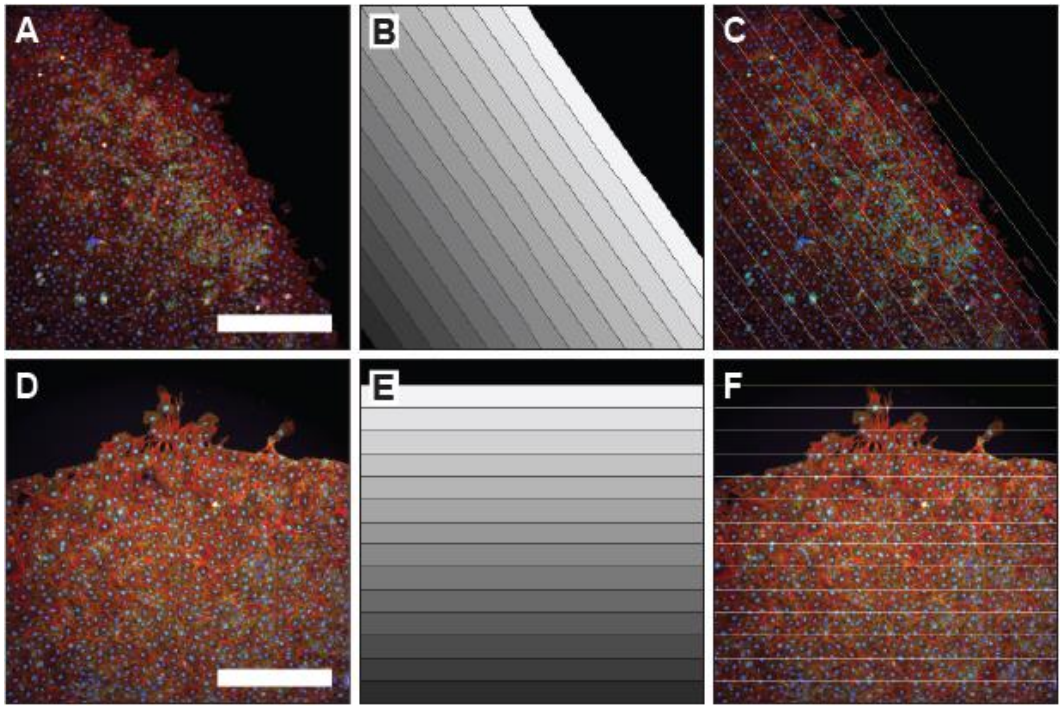

Figure 2.5: Bins were created for any image orientation and migration direction. (A,D) Original images labeled for F-actin (red), β-catenin (green), and nuclei (blue). (B,E) The algorithm automatically found the migratory front and generated equidistant bin lines parallel to the migratory front throughout the image. (C,F) Bin lines overlaid on top of the image to be analyzed. Scale bar = 500 µm.

2.3.3. Nuclear Orientation as a Measure of Cell Alignment

Nuclear orientation was used to measure cell alignment relative to the global migration direction. When a cell elongates, intracellular tension elongates the nucleus along the cell's long axis.[116, 117] 10x images of cell nuclei (Hoescht) and actin (phalloidin) were pre-processed (Figure 2.6A,D) and binned (Figure 2.6B,E). Nuclei that intersected the bin boundary lines were ignored. The cell area outline was included (red) to demarcate the migratory interface. The nuclear centroid and long axis angle were extracted from the binary image of binned nuclei using the built-in REGIONPROPS function. Using the angle and center point, a white line was drawn to visually validate that the long axis of each nucleus was measured (Figure 2.6C,F). The angles were normalized to the global migration direction such that a nucleus perfectly aligned with the migration direction would have a normalized orientation of 0°. Likewise, a nucleus with its long axis perpendicular to the migration direction would have a normalized orientation of 90°. Therefore, the possible values of the final normalized output were [0°,90°]. Within each bin, the average normalized nuclear orientation was plotted as a function of distance from the interface (Figure 2.6G), with values closer to 0° and 45° indicating directed and random orientations, respectively. Here, we observe a significant increase in alignment between 3 and 12 hours of migration time, but only in the intermediate bins 100-500 μm from the interface.

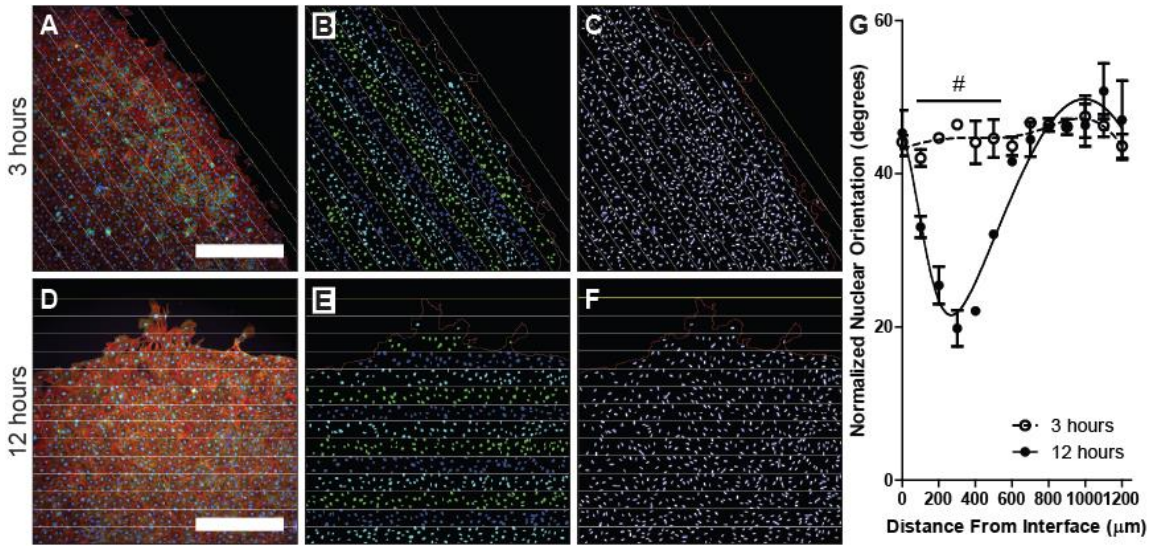

Figure 2.6: Nuclear orientation within bins was automatically measured. (A,D) Pre-processed original images of samples fixed and labeled for F-actin (red), β-catenin (green), and nuclei (blue). (B,E) Nuclei were separated into their respective bins as shown by alternating colors, excluding any that intersected a bin line. (C,F) The long axis for each nucleus was identified and labeled with white lines. The white line angle was measured and normalized with respect to the overall migration direction (i.e. the angle perpendicular to the bin lines). (G) The average normalized orientation was plotted against the distance from the interface. Scale bar = 500 μm. #$p<0.05$ for 3 compared to 12 hours at a given distance.

This method was validated with test images of ovals with known average orientation (Figure 2.7). Using the built-in RAND function, a dispersed set of pixels were randomly set as the oval centroids. Their sizes varied randomly based on the ellipse formed from randomly-assigned aspect ratios between 1.9 and 3. The orientations were set randomly between two limits as shown in Figure 2.7. This method could accurately discern between various levels of oval alignment. The long axes of the ellipses were accurately identified and labeled within bins (Figure 2.7A-F).

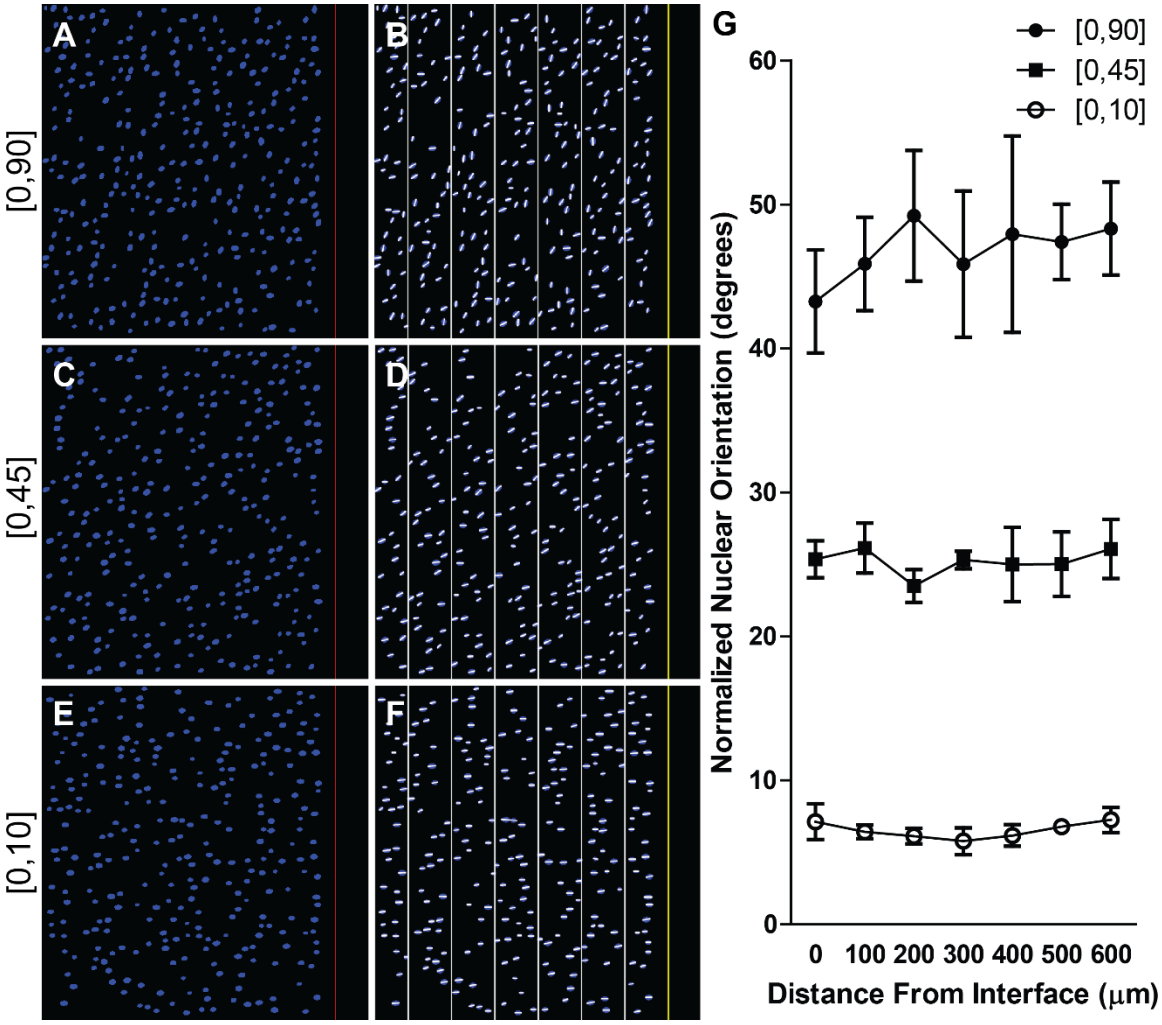

Figure 2.7: The nuclear orientation was tested using randomly generated ovals. (A,C,E) Sample images were made by constructing non-overlapping ovals with varying aspect ratios and random long axis orientations relative to a zero degree migration direction. The ranges for possible orientations were set to have larger [0°,90°], intermediate [0°,45°], and smaller [0°,10°] angle distributions. (B,D,F) The output drawings display white lines along the nuclear long axis. (G) Quantification of five images from each set revealed average nuclear orientations within each group.

This approach successfully measured cell orientation while avoiding the difficult problem of confluent cell segmentation. Since nuclear labeling is ubiquitous in fluorescent imaging, this method can be readily applied. In addition, extracting morphological properties from nuclei is a relatively simple task because the fluorescent signals are robust and rarely are nuclei overlapping in non-proliferative cell monolayers. The method is accommodating to various magnifications as

long as the nuclei are clearly identifiable. In our experience, 10x optical magnification or higher provide the necessary nuclear resolution.

2.3.4. Subcellular Compartmentalization

It is often important to measure relative protein levels in different parts of the cell, since proteins may have different functions based on their subcellular compartmentalization. For example, β-catenin is an intracellular protein and transcription factor that is found in three compartments: the adherens junction, the cytosol, and the nucleus. While in the cadherin complex at the adherens junction, β-catenin is sequestered at the cell membrane. When the adherens junction disassembles, β-catenin moves either to the cytosol, where it is degraded, or to the nucleus, where it promotes gene transcription.[118] More β-catenin at the cell membrane indicates higher cell-cell junction integrity, whereas more β-catenin in the nucleus indicates lower cell-cell junction integrity. Therefore, we used β-catenin localization at the cell membrane vs. in the nucleus to determine the degree of togetherness in collective migration. However, this type of algorithm could be used to understand protein subcellular compartmentalization in many biological assays.

Raw β-catenin and nuclear images (Figure 2.8A,D) were pre-processed to remove background noise and binned as previously described. The nuclear image was used to separate out nuclear (Figure 2.8B,E) from non-nuclear β-catenin (Figure 2.8C,F). Fluorescent intensity and cell number (number of nuclei) were measured within each bin for each image. Nuclear β-catenin as a percentage of the total intensity was then normalized to cell number and graphed vs. distance from the migratory interface (Figure 2.7G). This technique normalizes fluorescence within each image to enable comparisons of samples with heterogeneous labeling and images taken with variable exposure settings (although in our case images within the same experiment were taken

using a constant exposure setting). A greater value indicates less β-catenin is at the membrane and therefore a lower degree of togetherness. Here were show that at an earlier time point, there is a relatively constant 50~60% nuclear β-catenin throughout the migratory front. However, by 12 hours, this drops to ~30% except for a spike up near ~60% at 400 μm, suggesting that togetherness increases as a function of time and fluctuates as a function of distance from the migratory interface, with the lowest togetherness at the migratory zone.

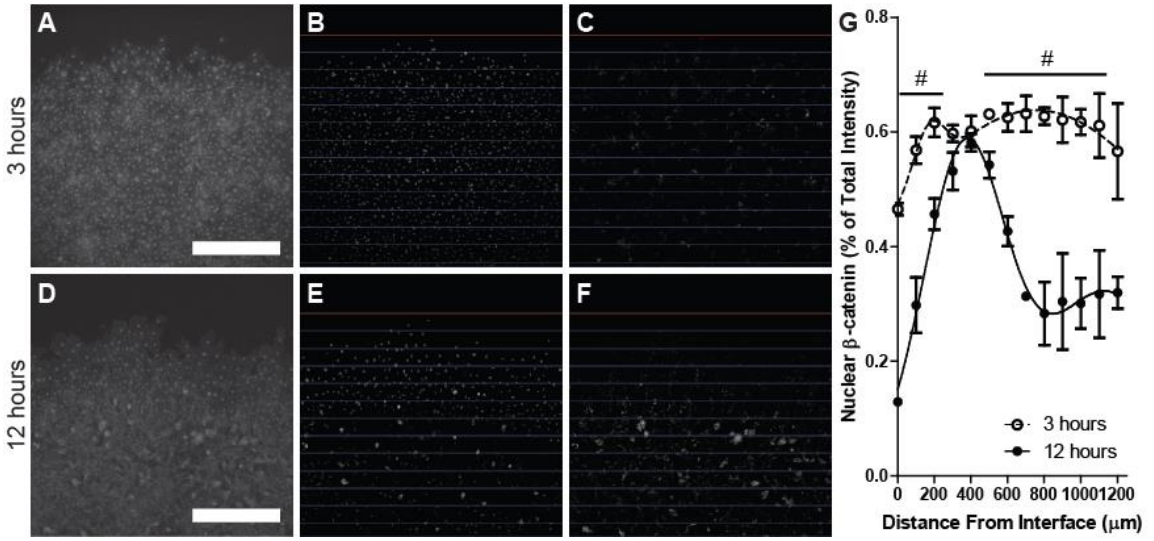

Figure 2.8: β-catenin subcellular compartmentalization was spatially quantified to detect differences in togetherness. (A,D) Initial β-catenin image prior to any pre-processing (high background noise). (B,E) Using the nuclear mask, the nuclear β-catenin was isolated before the background was removed by filtration. (C,F) The negative of the nuclear β-catenin channel was extracted and similarly filtered separately, representing the membrane-bound and cytoplasmic β-catenin. (G) Nuclear β-catenin fluorescent intensity was measured as the percent of total fluorescent intensity normalized to the number of cells within the bin. Scale bar = 500 μm. #p<0.05 for 3 vs. 12 hours at a given distance.

2.3.5. Cell Morphology by Voronoi Tessellation and Membrane Labeling

Cell area and morphology are important measurements in a variety of applications, including collective cell migration. However, it is challenging to segment cells within a confluent

monolayer where cell boundaries are inconsistent or have low contrast. Even when fluorescently labeled, intercellular proteins are non-uniformly expressed, leading to gaps in fluorescent signal. We initially used the Voronoi tessellation as a computationally-effective approximation of cell area using only nuclear labeling. In Voronoi tessellation, a specified set of points (called seeds) is initially defined, in our case the cell nucleus centroid. For each seed, a Voronoi region is developed that encompasses the set of points that are closer to that seed than to any other seed. The lines dividing the Voronoi regions are points that are equidistant to the two nearest seeds. In essence, Voronoi tessellation draws cell boundaries based on the assumption that all components of one cell are closer to their own nucleus than any other neighboring nucleus.[119, 120]

The first step in Voronoi tessellation of migrating cell layers was pre-processing and binning actin and nuclear images as previously described (Figure 2.9A,D). The coordinates of each of nuclear centroid were recorded using the built-in REGIONPROPS function (blue dots in Figure 2.9B,E). These coordinates were input into the built-in VORONOI function, which output the coordinates of the lines that formed the Voronoi region around each nucleus (green lines in Figure 2.9B,E). These annotations were validated by placing them on top of the original β-catenin image, which was the subcellular marker used to visualize the cell membranes. Voronoi lines that extended into the space beyond the cell migrating front were eliminated. Cells at the image edge were omitted from analysis (Figure 2.9C,F) because they represented incompletely imaged cells within the field of view.

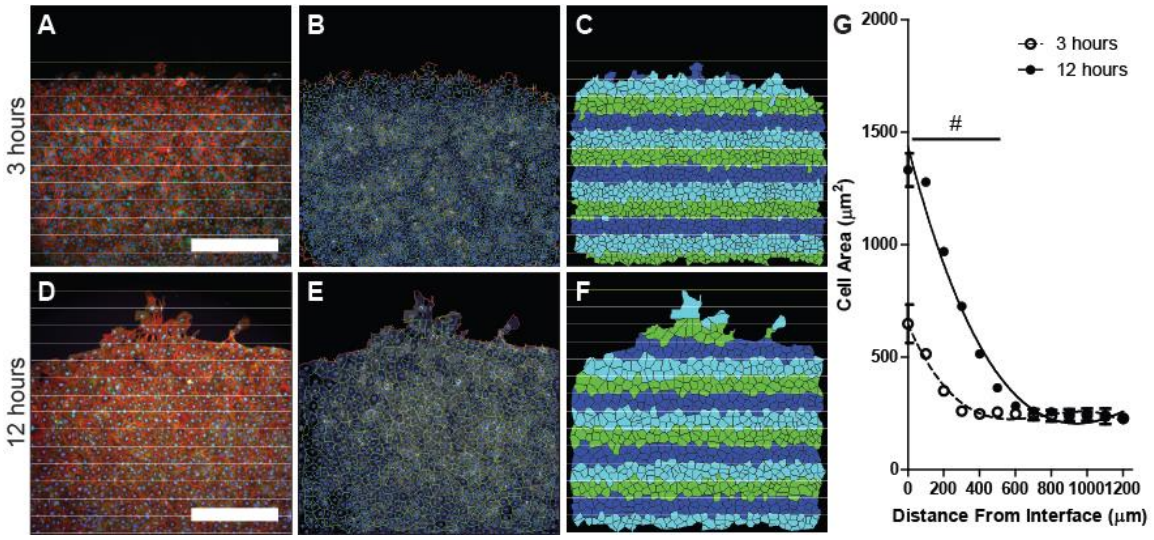

Figure 2.9: Quantification of cell area vs. distance was estimated through Voronoi tessellation map based on the nuclei. (A,D) Pre-processed images labeled for F-actin (red), β-catenin (green), and nuclei (blue). (B,E) Voronoi tessellation around the nuclear centroid (blue dots) produced lines equidistant from neighboring nuclei (green) approximating cell-cell boundaries. Voronoi regions beyond the migrating front were eliminated using F-actin labeling (red). (C,F) The polygonal shapes were used to approximate cell area vs. distance, with cells in each bin indicated by alternating colors. (G) Cell area vs. distance for 3 and 12 hours of migration. Scale bar = 500 μm. #$p<0.05$ for 3 vs. 12 hours at a given distance.

Cell area was then determined as the Voronoi region area. The Voronoi lines (green) and migratory front (red) from Figure 2.9B,E were combined to create fully circumscribed cells. Voronoi regions were filled using the built-in IMFILL function, and the Voronoi lines were subtracted from the filled-in Voronoi map. This produced separated polygonal cell areas (Figure 2.9C,F). This image was then binned as previously described, and cell area was quantified within each bin. For cells that intersected a bin boundary, the cell area was included in the bin in which more than half of its area resided. Average cell area for each bin was graphed as a function of distance from the migratory interface (Figure 2.9G). Using this method, we detected changes in cell area vs. distance over time in collectively migrating cells.[121] The cell area approximately doubled from 3 to 12 hours within 500 μm of the migratory interface. However, beyond 500 μm, area decreased to a minimum and did not differ over time.

Tessellation provided a good approximation of cell area; however, important cell morphological information such as aspect ratio was lost. We therefore also used a fluorescent membrane marker to determine cell area and aspect ratio. Cells labeled for β-catenin and nuclei were imaged at a higher 20x magnification (Figure 2.10A). A different membrane protein could also be used, for example VE-cadherin in adherens junctions.

Fluorescently labeled membrane proteins are often discontinuous. The primary challenge was to close gaps in the labeled membranes. First, nuclear bleed-through in the β-catenin channel was removed by subtracting the nuclear image. Edges of β-catenin labeled structures were found using the built-in EDGE function. To close gaps in the β-catenin labeling, the built-in IMCLOSE function was applied using the line structuring element. The IMCLOSE function therefore performed a dilation along a line of a given angle followed by an equal erosion of the edges. It was applied iteratively for line structuring elements of angles between -90° and 90° and line lengths of 5 pixels. This approach was crucial for closing small gaps within the membrane boundaries that were either incomplete from the original β-catenin labeling or not picked up by the EDGE function. Finally, the image was filtered with a Gaussian filter to get smooth features (Figure 2.10B). The inverse of the identified cell membrane was therefore the cells. The built-in IMFILL function was used to remove holes within the resulting approximate cell shapes. Any cells touching the edge of the image were removed using the built-in IMCLEARBORDER function because they represented incomplete cells.

A watershed algorithm was applied to separate two or more overlapping nuclei into separate regions. To accomplish this, the nuclear edges were found using the Sobel edge filter. The distance matrix, a matrix of pairwise distances between each non-zero pixel in the nuclear edge image, was returned using the built-in BWDIST function. Each pixel in the nuclear image is replaced by a Euclidean distance to the nearest edge. The center of each nucleus would therefore

be the brightest and the pixel values would radially decrease toward the edge. This image was finally subject to the built-in WATERSHED function. This algorithm comes from topographical maps with catchment basins. Therefore, the brightest pixels within each nucleus was considered the bottom of a "catchment basin" and lower intensity pixels corresponded to "higher elevation." Based on an elevation threshold, two overlapping nuclei were separated by a watershed line. The resulting watershed lines were subtracted out of the original nuclear channel, leaving behind separated nuclei.

The connected regions (i.e. potential cells) were identified with the built-in BWCONNCOMP function. The number of nuclei within each connected region was determined (Figure 2.10C). If there were no nuclei inside, the connected region was ignored from further analysis (Figure 2.10C, yellow regions). If there was one nucleus inside, the connected region was classified as a single cell (Figure 2.10C, green regions). If there were 3 or more nuclei inside, the connected region was omitted from further analysis (Figure 2.10C, red regions). For connected regions with exactly 2 nuclei inside, an algorithm was applied to split the region such that valid single nucleus cells were formed. The two nuclear centroids were found using the built-in REGIONPROPS function. The line formed by connecting the two nuclear centroids was determined. The connected region was then split into two cells by drawing a line perpendicular to the nuclear centroid-connecting line at the midpoint between the two nuclear centroids (Figure 2.10C, cyan regions).

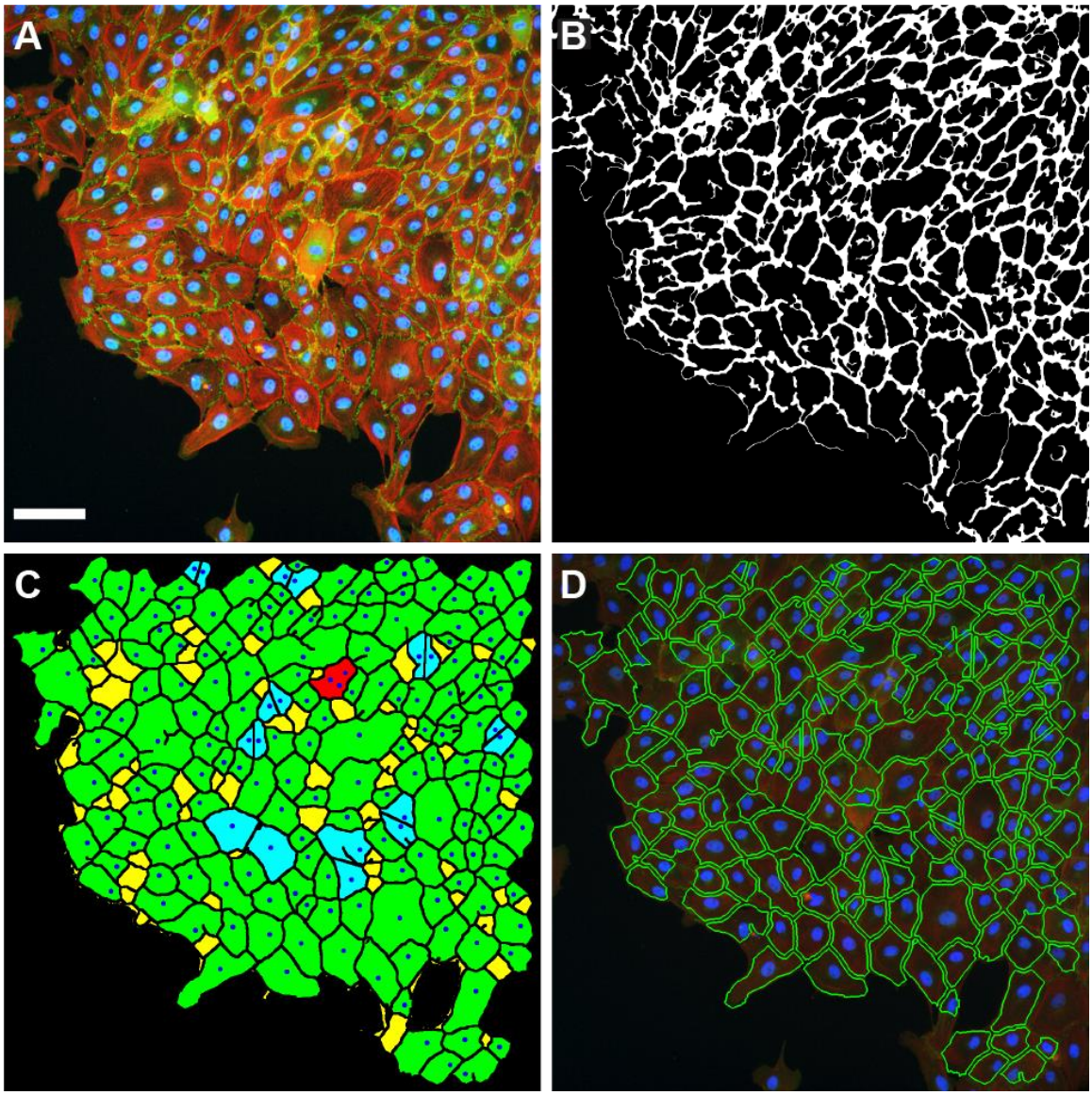

Figure 2.10: Cell area and aspect ratio were measured from images of labeled membrane β-catenin. (A) Images of samples labeled for β-catenin (green), F-actin (red), and nuclei (blue). (B) After processing the β-catenin channel, a preliminary cell membrane network was produced. (C) A classification map was produced, labeling each identified cell. Yellow and red connected components were excluded for having too few and too many nuclei (blue dots), respectively. Cyan connected components were initially identified as having incomplete boundaries between exactly two nuclei, but the gaps were filled with a midpoint approximation. Green connected components were valid. Both green and cyan objects from (C) were used for further analysis as shown in (D). Green outlines the accepted shapes overlaying the original image. Scale bar = 100 μm.

After connected region classification (Figure 2.10C,D), the aspect ratio and area of the identified cells were determined using the built-in REGIONPROPS function. The aspect ratio was

calculated by dividing the MajorAxisLength array by the MinorAxisLength array produced from the REGIONPROPS function. This restricted the calculated aspect ratio to a minimum of 1 (i.e. theoretical circle or diamond shape) and an unbounded maximum.

2.3.6. Tissue Interface Roughness as a Measure of Sprouts and Extensions

Interface roughness is an important measure of tissue features, indicating how many sprouts or extensions are present. To measure the migrating interface roughness, we implemented an adapted method used for single-cell membrane ruffles, previously described by Lacayo *et al*.[122] In brief, they measured the cell front roughness using the formula for a parametric curve:

(Eq. 1) $C(p) = \frac{x'y'' - y'x''}{[(x')^2 + (y')^2]^{3/2}}$

C(p) is the curvature at each point p along the curve and it is based on the first and second derivatives of the x and y coordinates at point p. This was discretized for computation with the following formulas:

(Eq. 2) $x'(n) = \frac{x(n+1) - x(n-1)}{2(\Delta x)}$ $y'(n) = \frac{y(n+1) - y(n-1)}{2(\Delta y)}$

(Eq. 3) $x''(n) = \frac{x'(n+1) - x'(n-1)}{2(\Delta x)}$ $y''(n) = \frac{y'(n+1) - y'(n-1)}{2(\Delta y)}$

Equation 2 requires an ordered array of each pixel's x and y coordinates along the curve. Equation 3 takes the array outputs from Equation 2 as its input. These equations are valid for all n = [2, N-1], where N is the total pixel number along the curve. To evaluate the derivatives at n = 1 and n = N, the array wrapped around such that at n = 1, (n – 1) = N and (n + 1) = 2 in Equation 2. Likewise, at n = N, (n – 1) = N-1 and (n + 1) = 1 in Equation 2. Once these arrays were evaluated, they were used in Equation 1 to produce a curvature array representing the curvature at each pixel along the curve. Lacayo *et al.* used the sum of the absolute value of the curvature array to

represent roughness. Whereas Lacayo *et al.* used constant array lengths among samples, we divided the preliminary roughness number by the total number of pixels in the curve to account for the differences in surface area among our samples. Equation 4 provides the interface roughness as a measure of the interface curvature per pixel and is the primary algorithm output.

(Eq. 4) $$interface\ roughness = \frac{\sum|C(p)|}{N}$$

Although roughness metric generation was fairly simple, generating an array of ordered coordinates for the interface pixels was non-trivial. Interface pixel coordinates were determined by a separate algorithm that exploited the F-actin labeling in the pre-processed image to capture the full cell-covered area (Figure 2.11A,D, Figure 2.12A). We developed an algorithm that first classified each pixel as (1) interface, (2) inner, or (3) outer. Interface, inner, and outer pixels were assigned values of 1 (white), 0.5 (light gray), and 0 (black), respectively (Figure 2.11B,E, Figure 2.12B). Input images were consistently oriented such that the endpoints were on the top and bottom rows. The starting pixel was chosen to be the interface pixel in the first row. The algorithm populated the ordered set of interface coordinates until it reached the bottom image row. Once a pixel was added to the ordered coordinate list, its value became 0.2 (dark gray). To choose the next pixel, the algorithm examined the nearest eight neighboring pixels (Figure 2.22C,D). If there was only one neighbor with a value of 1, then there was only one option for the next interface pixel and the decision was simple. However, if there were multiple neighbors with a value 1, the algorithm chose the next best pixel based on all the potential of each path option to avoid a dead-end. For example, when at the pixel with the black asterisk in Figure 2.12D, there were two options for the next pixel (green and red asterisks). The algorithm iteratively considered “what if” it went to each of the possible next pixels. The red asterisk was eliminated because it no longer contained any neighbors of the value 0.5 (gray), rightly indicating that that path strays from the inner section and would likely lead to a dead end. The green asterisk was accepted because (1) it

contains a neighbor of value 1 and therefore can guarantee a third pixel ahead of the current one, (2) it maintains proximity to at least one pixel of value 0.5, and (3) the only other option failed. Therefore, those four pixels starting at the red asterisk and moving away from the tissue interface were ignored from analysis. The final output of the tracing was validated by a red outline on the image (Figure 2.11C,F). The ordered coordinates of the red line served as the input for the curvature function in Equation 1. We observed that interface roughness increased from 6 to 24 hours of collective migration (Figure 2.11G).

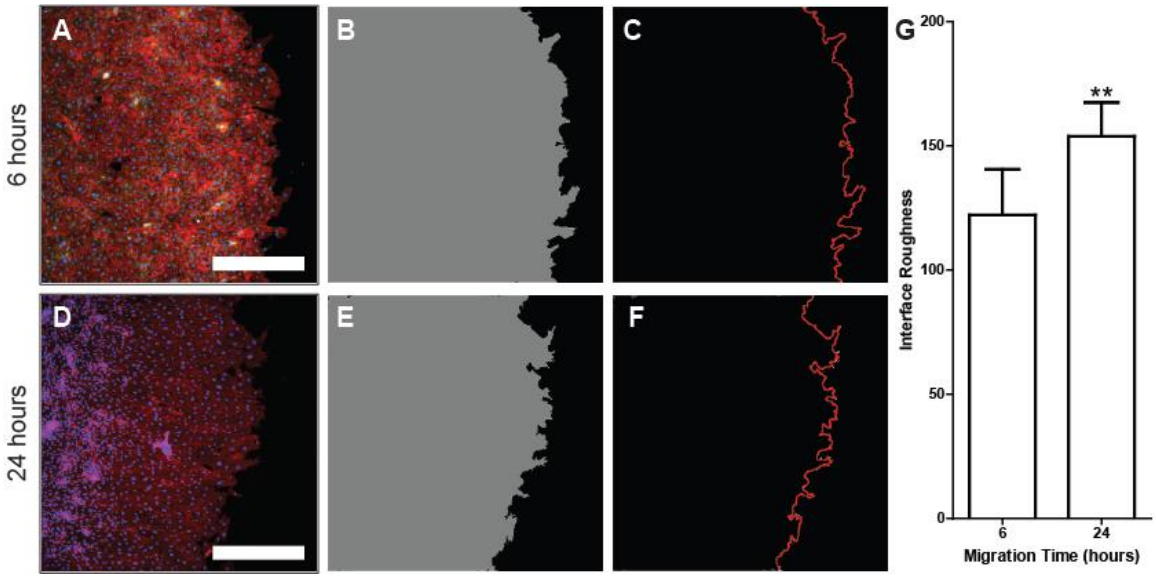

Figure 2.11: An algorithm to quantify the sample interface roughness of actual samples adapted was adapted from a method for single-cell membrane ruffles. (A, D) Input images with labeled F-actin (red), β-catenin (green), and nuclei (blue). (B,E) The naïve image classification was based on the thresholded input images. (C,F) The algorithm traced highly irregular interface curves from actual samples. (G) Interface roughness for cell collective migration after 6 and 24 hours. Scale bar = 500 μm. **p<0.001.

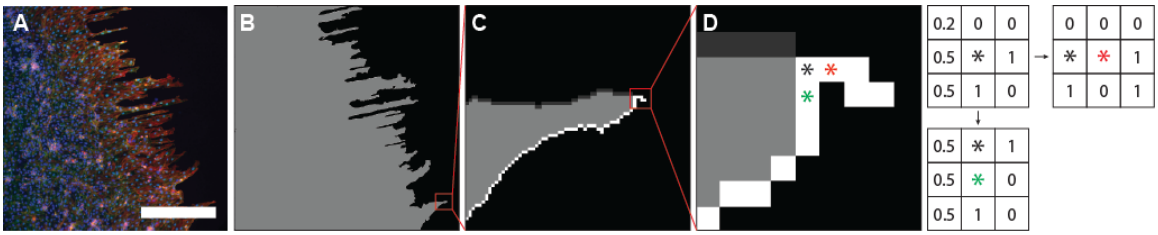

Figure 2.12: Automated interface roughness quantification was achieved by first tracing the cell migratory front contour. (A) Pre-processed input images with labeled F-actin (red), β-catenin (green), and nuclei (blue). (B) The naïve pixel classification was based on the thresholded image such that the background was 0 (black), the cell-occupying area was 0.5 (light gray), and the boundary was 1 (white). (C) Starting at one edge, the interface was traced. The coordinates of the trace were stored and their pixel values were marked as 0.2 (dark gray) to avoid repetition. (D) Whenever there was a choice of direction, the algorithm evaluated the likelihood of reaching its goal. The algorithm considered the 8-pixel neighborhood map when making the choice, shown in the 3x3 grids. For example, if the current pixel were at the black asterisk, the next pixel could be the red or green asterisks. Since the red asterisk would take the path away from the interior (i.e. there are no 0.5 neighbors), it would not be chosen and the tracing would continue to the green asterisk. Scale bar = 500 µm.

The interface roughness as validated using user-generated test images (Figure 2.23). The test images in Figure 2.13 were fabricated using a controlled roughness function generator. The function randomly generated an equation that was the sum of five sine or cosine terms with corresponding random amplitudes and frequency changes. Sine or cosine terms were chosen with 50% chance. The random set of frequency modulators was multiplied by a constant frequency factor to affect overall roughness.

(Eq. 5) $$f(x) = \sum_{i=1}^{5} \begin{cases} A(i) * \sin(F * B(i) * x) \\ A(i) * \cos(F * B(i) * x) \end{cases}$$

For the function input, A and B were 5-element arrays containing random values. The values in A were constrained such that the amplitude did not cause the function to have pixel coordinates outside the image area. The frequency factor F was set to 0.001, 0.1, 0.4, and 0.8 to generate sample images (Figure 2.13 A,D,G,J). We observed a logarithmic relationship between frequency factor and measured interface roughness with significant differences among all values

(Figure 2.13M). This significance even included a small, but discernable increase from the G to J image, demonstrating the sensitivity of this algorithm.

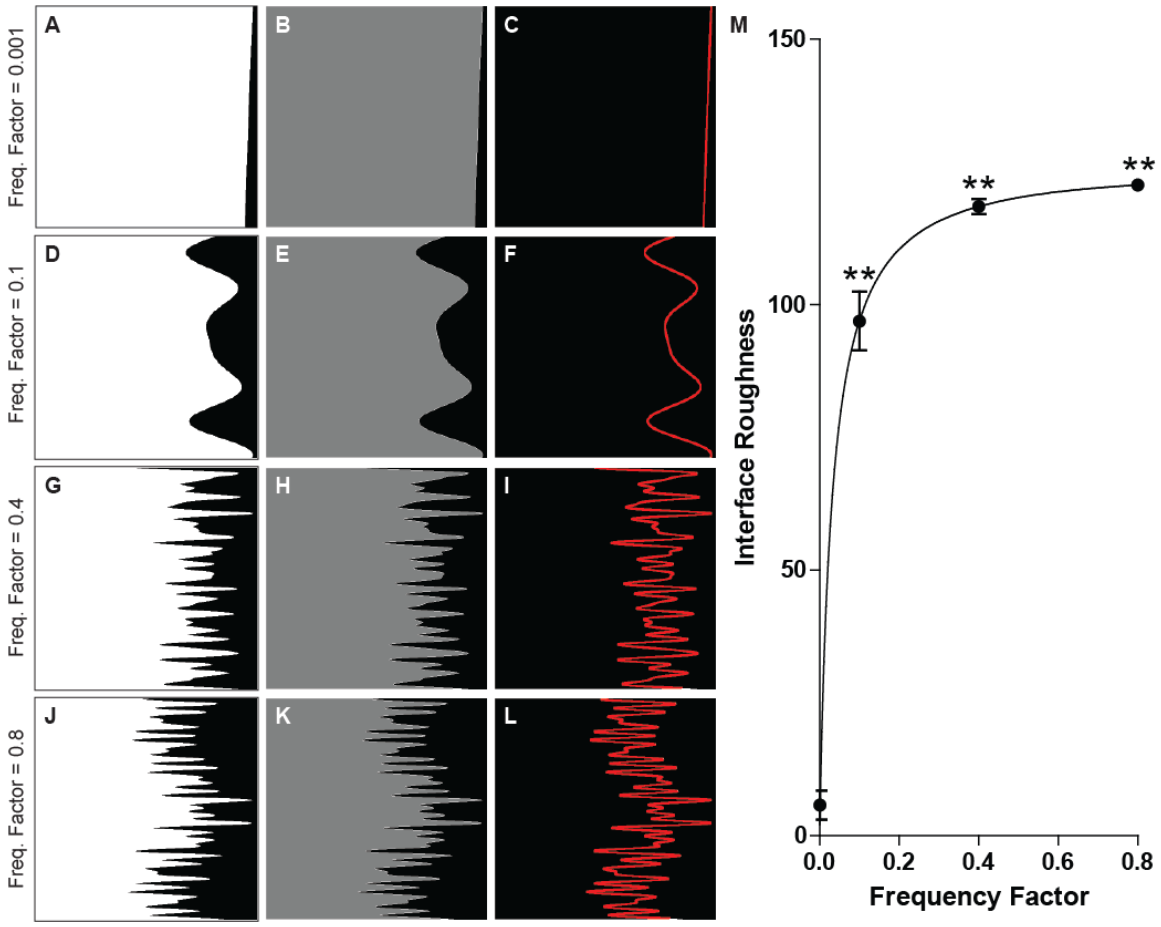

Figure 2.13: The tissue interface roughness algorithm was tested using images created by a controlled roughness function generator. (A,D,G,J) Images were fabricated using sums of sine or cosine terms, each with randomized amplitudes and frequencies. Frequency factor tuning increased or decreased the overall frequency to simulate roughness. (B,E,H,K) The naïve image classification was based on the thresholded input images. (C,F,I,L) Accurate tracing was validated by the red outline. (M) Five images of each frequency factor were used in the quantification and revealed a logarithmic curve. Scale bar = 500 µm. **p<0.001 compared to all other samples.

2.3.7. Extracellular Fiber Length and Orientation

Small fiber morphology is important in many biological applications including extracellular matrix protein topology which has been shown to be important in directed cellular migration. To examine extracellular matrix structure, samples were labeled for fibronectin, a prominent extracellular matrix protein (Figure 2.14A). Input images were filtered using Gaussian and median filters before being thresholded as previously described. Using the built-in BWMORPH function, the thresholded image was skeletonized so that each labeled fiber was reduced to a single-pixel thickness structure. Using the same BWMORPH function, the branched points were identified and removed to isolate contiguous fibers. The built-in REGIONPROPS function was used to measure skeletonized fiber orientation and area. Since fibers were one pixel thick, skeletonized fiber area was equal to fiber length. With these metrics, many subsequent statistical analyses could be performed given the distribution of both fiber lengths and fiber angles (Figure 2.14D).

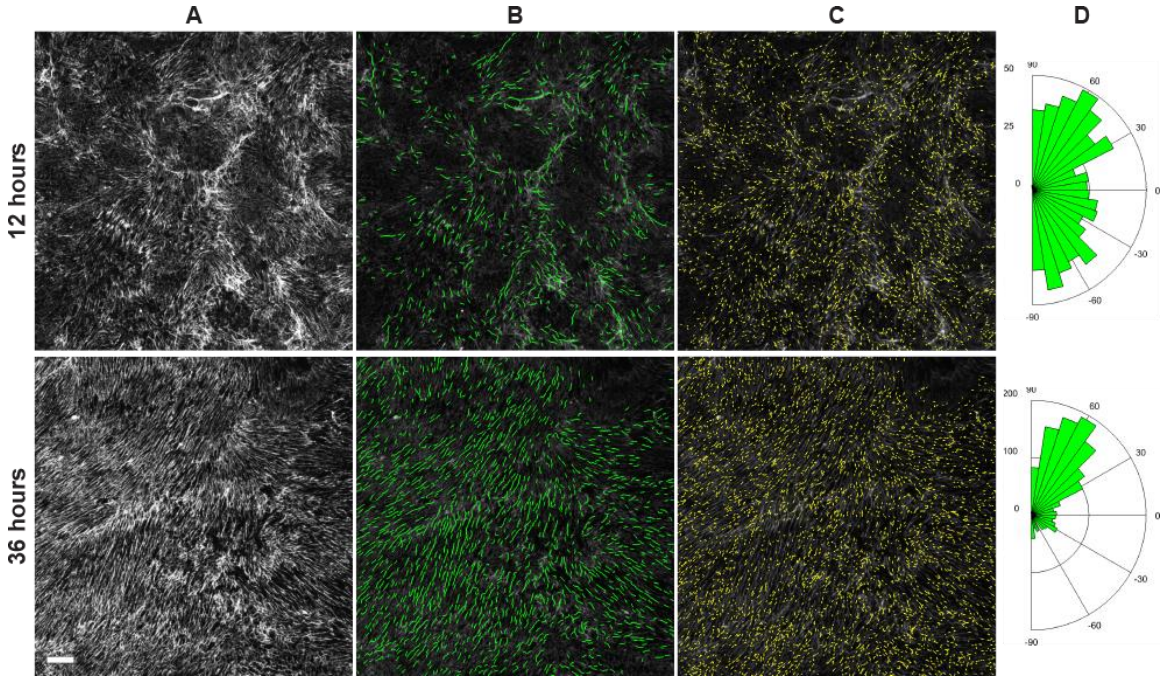

Figure 2.14: Fibronectin fiber length and angle were determined as a measure of extracellular matrix structure. (A) Input fibronectin images were filtered using Gaussian and median filters to remove background. Fibers were skeletonized and all branch points were removed. The identified fibers were classified by their length. Fibers with lengths above (B, green) and below (C, yellow) a given cutoff were overlaid on the original fibronectin image. (D) The distribution of angles from fibers in (B) shown in a rose plot. Scale bar = 20 µm.

2.4. Discussion

In this chapter, we introduced novel, semi-automated computational approaches for high-throughput quantification of cell and tissue features to standardize collective cell migration analysis. The approaches were designed to address the challenge of cellular segmentation in confluent monolayers with low intercellular contrast by exploiting ubiquitous fluorescent labels. All algorithms were implemented in MATLAB, an accessible interface for many researchers.

We hope that these methods will serve as a springboard for rigorous, high-throughput, transparent image analysis throughout the biological and biomedical research communities. It was recently argued that results and conclusions without transparent and robust analysis methodology are dubious.[107] Along the same lines, quantifying absolute pixel intensity is

considered pseudo-quantitative. Conclusions may be more convincing if fluorescent signals are considered to be on or off and then used to quantify cellular features. The methods in this paper will help maintain research integrity as microscopy techniques continue to advance. In addition, there is a balance between generalized power and automation. Rather than creating a large generalizable application to analyze many types of images, a modular approach may be more appropriate. For example, the methods in this paper could come as a confluent cell monolayer package or collective cell migration package.

Although we apply these algorithms to collective cell migration, the measurements can be generalized to other contexts where it is important to measure cellular orientation, subcellular compartmentalization, tissue interface roughness, and extracellular matrix protein fiber distribution and structure. For example, cellular orientation, nuclear:non-nuclear ratio of a subcellular component, and extracellular matrix protein fiber analyses could be performed on images of other cell types or single migrating cells. The extracellular matrix protein fiber analysis could be performed on structures with fibrillar shapes, such as neurites or filopodia.

Although these methods are helpful for quantifying collective migration, they are limited to two-dimensional images. Information was lost when confocal z-stacks were collapsed into one plane. Although nuclear and F-actin labeling is common, our dependence on both labels for many of these algorithms may prevent application on existing images or in experiments where those fluorescent channels need to be labeled with another marker. Nuclear orientation and Voronoi tessellation are approximations for cellular orientation cellular area, which limits their accuracy and potential application. The fiber analysis has an inherent bias toward short fibers since it breaks up clustered networks of fibers. While this is not a problem in the context of cellular processes, it may impact fiber analysis by reporting artificially low fiber lengths.

3. The Effect of Substrate Stiffness on Endothelial Cell Collective Migration

3.1. Introduction

Endothelial cell (EC) migration is critical to restoring a confluent endothelium following vascular denudation, creating new blood vessels during angiogenesis, and vascularizing tissue engineering structures. EC migrate upon activation following injury or in response to inflammatory cytokines and growth factors, such as VEGF. In single cell migration, the cell's trailing end bound to the substrate creates the resistance to forward propulsion. However, in collectively migrating EC, cell-cell adhesions add to the resistance to forward propulsion.

EC migrate across the vessel surface as well as in all tissues of the body, in addition to through tissue engineering scaffolds. The stiffness of the surrounding stromal tissue is a crucial input, affecting migration, proliferation, survival, and sensitivity to other exogenous signals.[61, 67, 68, 71, 72, 74, 123] Substrate stiffness changes must be considered to fully understand endothelial cell response in normal aging and diseases in which stromal stiffness increases. Furthermore, our understanding of how substrate stiffness impacts endothelial cell function will inform tissue engineering-based strategies. That is, researchers and clinicians need to be mindful of the mechanical properties of the tissue-engineered implants to promote vascularization.

Cellular migration on substrates of varied stiffness has largely been studied in individual cells. Single cells migrate faster on soft substrates.[64, 80] Single EC are thought to migrate in a similar fashion to fibroblasts and epithelial cells in a 3-phase process: (1) propulsion in the forward direction, (2) cell contraction, and (3) retraction of the tail.[124, 125] Propulsion occurs through Rac signaling.[126] Cell contraction is a Rho/ROCK mediated process, causing myosin to pull against the actin cytoskeleton.[86, 127] Tail retraction is a consequence of Rho/ROCK-mediated contraction leading to focal adhesion dismantling.[128] Integrin signaling in focal adhesions promote Rac and

Rho/ROCK pathways.[129] Substrate stiffness therefore impacts each phase of migration through focal adhesion formation, stability, and degradation.

More recently, cell collective migration on substrates of different stiffness has been studied, although largely in epithelial cells. Epithelial cell collective migration is faster on stiffer substrates, and requires myosin-based contractility to overcome cadherin-based resistance.[48] Stiffness-dependency for migration has also been shown to occur with single fibroblasts[64] and collectively-migrating cancer cell lines.[81] It is clear that changes in substrate stiffness are an important factor for understanding collective migration; however, the effect of substrate stiffness on EC collective migration after injury has not been examined.

While EC migrate collectively on substrates of varied stiffness in health and disease, little is known about how this process occurs. It is imperative that we understand how substrate stiffness affects EC collective migration in pathologic states so that we can best design therapies to promote re-endothelialization. In this chapter, I describe an investigation of EC collective migration using a cage assay on collagen coated polyacrylamide gels of varying stiffness. I hypothesize that EC migrate faster and farther on stiffer substrates due to different balances between cell-ECM and cell-cell adhesion. In support of this hypothesis, I interrupted cellular contractility with a specific ROCK inhibitor and knocked down fibronectin and α_5 integrin subunit using siRNA techniques. We found that ROCK-mediated contractility inhibits collective migration on soft, but not stiff substrates. We also found that α_5 integrin, but not fibronectin, is essential for directed collective migration and the farther migration distance on stiffer substrates. These data enhance our understanding of how collective migration is controlled by specific integrins and contractility based on the mechanotransduction of substrate stiffness.

3.2. Methods

3.2.1. Polyacrylamide Hydrogels

Polyacrylamide (PA) hydrogels were made based on previously described methods.[64, 65] Bottom 22x22 mm coverslips were made hydrophilic by treating them with 0.1 M sodium hydroxide (NaOH) for 3 minutes and then drying them by vacuum aspiration. Coverslips were then treated with (3-aminopropyl)trimethoxysilane (3-APTMS) for 3 minutes and then vigorously washed with high-volume distilled water (3x 10 minutes). After coverslips were dried, they were treated with 0.5% glutaraldehyde solution for 30 minutes. These activated bottom coverslips were used as the base for the PA hydrogels. Top 22x22 mm coverslips were made hydrophobic by treating them with Surfasil® Siliconizing Fluid for 30 seconds followed by drying in a 65°C oven for 15-30 minutes.

PA hydrogels of various mechanical stiffnesses were made by mixing different ratios of 40% acrylamide and 2% bis-acrylamide solutions. For our experiments, acrylamide concentration was held constant with increasing bis-acrylamide, resulting in linearly increasing substrate stiffness. Final solution concentrations and their correlated elastic moduli are shown in Table 3.1. Mechanical stiffness of all PA gels was quantified by atomic force microscopy (Figure 3.1).

TEMED (1:333) and 10% ammonium persulfate (1:100) were added to the PA solution to initiate polymerization. After vortexing, 200 µL PA solution was added to an activated bottom coverslip. An activated top coverslip was placed on top of the PA gel solution creating a PA hydrogel sandwich between the activated top and bottom coverslips. PA hydrogels were fully polymerized for 10 minutes before the top coverslip was removed.

Table 3.1: Final concentrations of acrylamide and bis-acrylamide with the elastic modulus measured by atomic force microscopy

Acrylamide (%)	Bis-Acrylamide (%)	Elastic Modulus (kPa)	Name
10	0.03	3.99 ± 1.24	Soft
10	0.10	13.75 ± 1.09	Intermediate
10	0.60	50.03 ± 7.49	Stiff

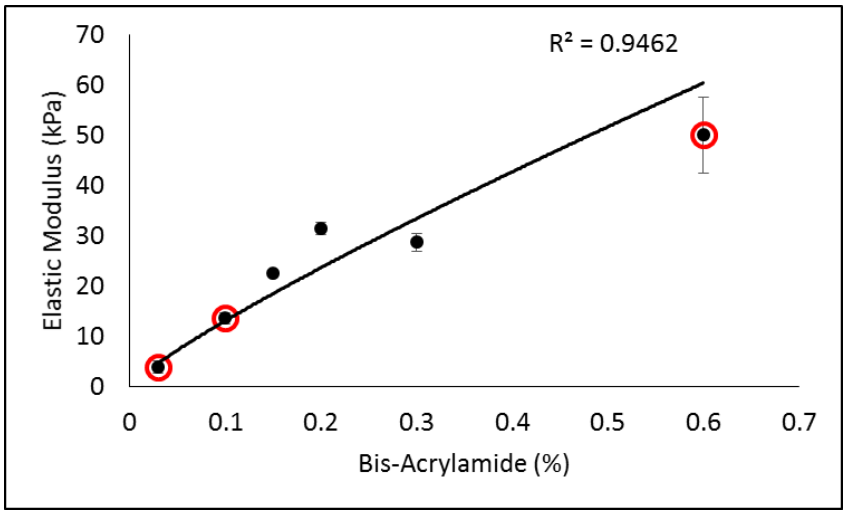

Figure 3.1: Atomic force microscopy was used to measure PA gels elastic modulus. Three stiffnesses (red circles) were selected for all future experiments. Acrylamide concentration was held constant.

Chemically-inert PA hydrogels were rinsed with 50 mM HEPES buffer (pH 8.5). The Sulfo-SANPAH linker molecule was used to attach collagen to the PA hydrogel surface to enable cell attachment. 0.5 mg Sulfo-SANPAH was dissolved in 1 mL 50 mM HEPES buffer (pH 8.5) and 10% dimethyl sulfoxide (DMSO). This solution was pipetted onto the dried PA hydrogel surface, exposed to UV light (250 nm) for 10 minutes, and rinsed with 50 mM HEPES buffer (pH 8.5). PA hydrogels were incubated with 200 µg type I collagen for 12-24 hours at 4°C. Functionalized

collagen-coated PA hydrogels were rinsed with sterile phosphate-buffered saline (PBS) in 6-well plates and stored at 4°C for up to 1 week. Just prior to use, PA hydrogels were UV-sterilized (250 nm) for 30 minutes.

3.2.2. Cell Culture

Porcine aortic endothelial cells (PAEC) were used as previously described in Chapter 2.

3.2.3. Cage Migration Assay

A cage migration assay based on previous studies[110, 111] was modified for our experiments (Figure 3.2). The bottom surfaces of polystyrene hollow cylindrical cages (6 mm diameter) were pre-treated for 30 minutes with 2% Pluronic® F-127 solution, a hydrophobic surfactant used to prevent damage to the underlying extracellular matrix layer during incubation. Cages were then air-dried for 1-3 hours and lastly dried in an oven at 65°C for 1 hour. Immediately before use, cages were UV-sterilized (250 nm) for 30 minutes.

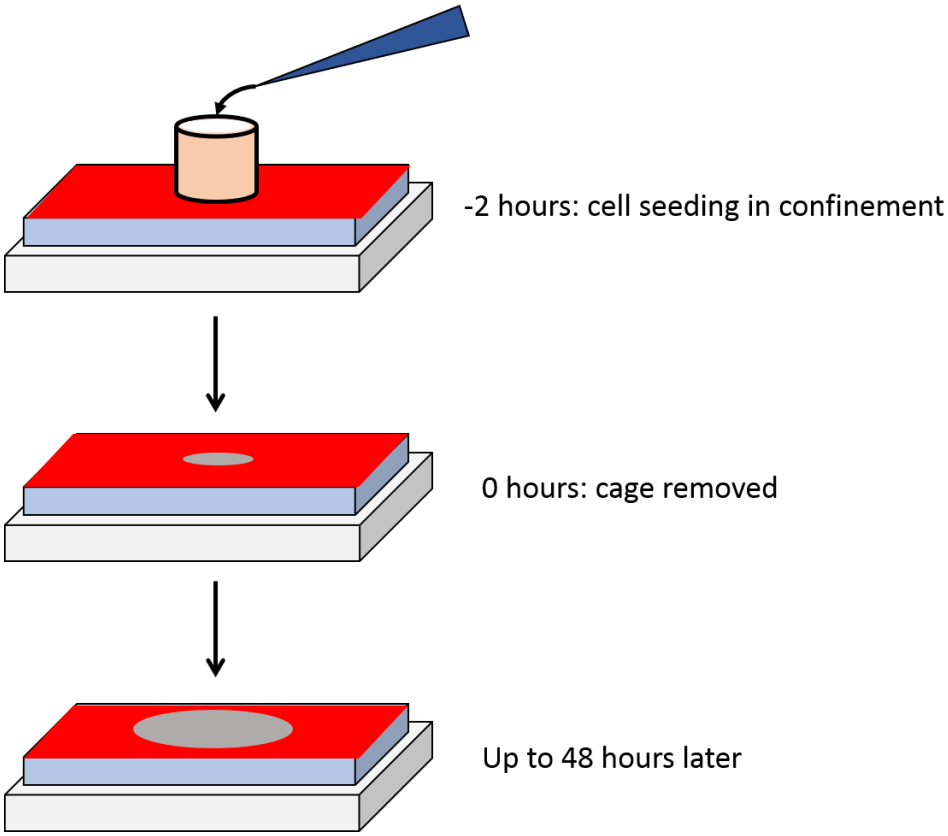

Figure 3.2: The cage migration assay. It begins with seeding 30,000 cells per cage on top of type I collagen-coated (red) PA hydrogels (blue) on 22x22 mm coverslips (gray). Endothelial cells were seeded in 5 mm cages, which were removed after 2 hours (time zero). Cells were then allowed to migrate radially outwards for up to 48 hours.

The cage assay was performed as described in Chapter 2 (Figure 2.1), except on PA gels. PAEC were detached with 0.05% trypsin-EDTA, counted using a Z1 Coulter Particle Counter (Beckman Coulter), and re-suspended at 300,000 PAEC/mL in growth medium. Two polystyrene hollow cylindrical cages (6 mm diameter) were placed on top of the 22x22mm PA hydrogels in 6-well plates. 100 µL of cell suspension was added to each ring, resulting in 30,000 PAEC in each cage. The samples were incubated for two hours at 37°C and 5% CO_2 to enable confined cell attachment, after which the cages were removed and 3 mL growth medium was added to the well

to completely cover the samples. The time of cage removal, at which point migration started, was considered time zero. PAEC migrated radially outward from 0-48 hours.

3.2.4. Pharmacological Inhibitors

For some experiments Y-27632 (10 μM), a specific Rho kinase (ROCK) competitive inhibitor, was used to reduce Rho/ROCK-derived cell contractility.

3.2.5. Knockdowns with siRNA Transfection

siRNA transfection was used to knock down key proteins of interest. Custom fibronectin and α_5 integrin subunit siRNAs were purchased from Ambion, targeting the sequences shown in Table 3.2. ON-TARGET plus® Control Non-Targeting Pool siRNA (Thermo Scientific) was included as a negative control in addition to the null case in which no siRNA was added. Lipofectamine RNAiMAX® (Invitrogen) was used as the transfecting agent following the manufacturer's protocol. PAEC were seeded at ~60% density in 6-well plates using growth medium without any antibiotics. PAEC were allowed to attach for 24 hours prior to transfection. On the day of transfection, 0.1 μM siRNA was added to 125 μL Opti-MEM. Separately, 7.5 μL lipofectamine was added to 125 μL Opti-MEM. The two solutions were combined and mixed at room temperature for 5 minutes. 250 μL of the resulting siRNA-lipofectamine solution was added to each well. In the null control, lipofectamine alone was added (i.e. no siRNA). Transfection continued for 3 days in a humidified incubator at 37°C and 5% CO_2. After transfection, PAEC were trypsinized and prepared for use in the cage assay or Western blot.

Table 3.2: siRNA sequences.

Target Protein	Target Gene	Target Sequence
Fibronectin	FN1_p	5'-GACUGGUGGUUACAUGUUAtt-3'
α_5 integrin subunit	ITGA5	5'-GCAGAGAGAUGAAGAUGUAtt-3'

Knockdown was confirmed by Western blot for protein content. For Western blot, PAEC were trypsinized, pelleted, and lysed in ice-cold lysis buffer (20 mM Tris, 1% deoxycholate, 150 mM NaCl, 1% Triton X-100, 2 mM EDTA, 2 mM PMSF, 0.1% SDS, 1 µg/mL leupeptin, 2 mM NaVO4, 50 mM NaF, 10% glycerol, complete protease inhibitor, pH 7.4). After 10 minutes at 4°C, the samples were centrifuged for 10 min at 10,000g and 4°C to remove insoluble material. Cell lysates were normalized for protein content using a BCA assay (ThermoFisher), separated by SDS-PAGE on a 4-12% Bis-Tris gel, and transferred to a nitrocellulose membrane (Invitrogen). After blocking in 5% Blotto (Biorad), membranes were incubated with primary mouse fibronectin (1:250, Invitrogen) or α_5 integrin (1:250, Invitrogen) antibodies overnight at 4°C followed by a secondary horseradish peroxidase-conjugated anti-mouse antibody for 2 hours at room temperature. Protein bands were detected using an enhanced chemiluminescence kit (Western Lightning, PerkinElmer), and visualized with a Fluorchem digital imager (Alpha Innotech). Band intensity was quantified using AlphaEase FC software.

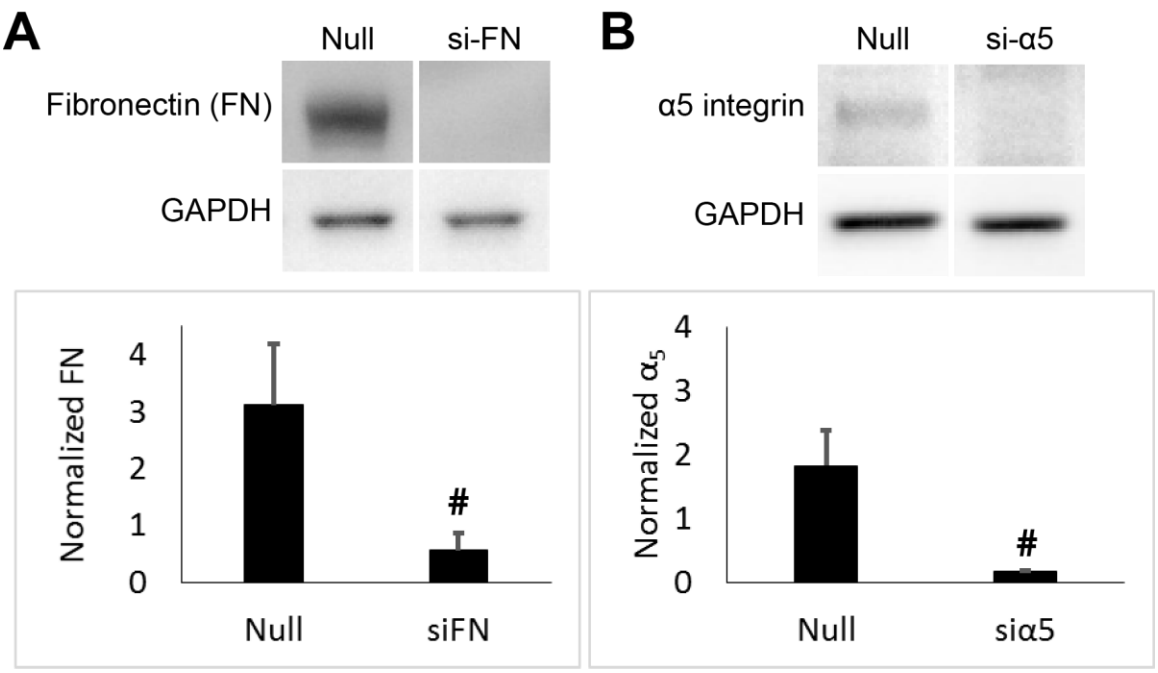

Figure 3.3: Fibronectin and α_5 integrin knock downs were validated by western blot. (A) Western blot of fibronectin and GAPDH with band intensity quantification. (B) Western blot of α_5 integrin and GAPDH with band intensity quantification. #$p < 0.05$.

3.2.6. Live Cell Imaging

Live cells were imaged by phase contrast microscopy on an Olympus IX81 inverted fluorescent microscope. An environmental chamber surrounding the microscope stage allowed for stable temperature (37°C) and 5% CO_2. SPOT Advanced software from Diagnostic Instruments was used to capture images through the SPOT Flex 64MP color digital camera every 5 minutes for up to 24 hours. Serial images were output into an .AVI video format using ImageJ software.

3.2.7. Immunocytochemistry

For fluorescent labeling, samples were fixed with 4% paraformaldehyde (PFA) for 15 minutes at 4°C. Samples were rinsed with PBS and permeabilized with 0.1% Triton X-100 for 5 minutes at room temperature. Samples were then rinsed and blocked with 1% bovine serum

albumin (BSA) for 15 minutes at room temperature. Primary antibody solutions were diluted in 1% BSA and include mouse anti-fibronectin (1:250), mouse anti-β-catenin (1:250), rabbit anti-VE-cadherin (1:250), rabbit anti-phospho-MLC (Thr18/Ser19), and rabbit anti-phospho-FAK (Tyr397). Samples were incubated overnight at 4°C. After thorough rinsing, samples were incubated with secondary antibody solution including goat anti-mouse IgG AlexaFluor® 488 (1:250), goat anti-rabbit IgG AlexaFluor® 633 (1:250), rhodamine phalloidin (1:100, F-actin label), and Hoechst 33342 (1:2000, nuclear label) in 1% BSA. After 1 hour at room temperature, samples were rinsed with PBS and stored in PBS at 4°C until use.

3.2.8. Proliferation Assay

Bromodeoxyuridine (BrdU) was used to measure endothelial cell proliferation. 1:100 BrdU reagent was added to growth medium for the final hour of the experiment. Samples were fixed and permeabilized as previously described. Nuclei were permeabilized by successive acid washes. Samples were incubated in 1 M hydrochloric acid (HCl) for 10 minutes at room temperature and then in 2 M HCl for 20 minutes at 37°C. The acid solution was neutralized with 0.1 M borate buffer solution (0.77 g boric acid and 1.12 g sodium tetraborate in 250 mL distilled water) for 12 minutes at room temperature. Samples were blocked with 1% BSA solution for 15 minutes at room temperature. Samples were then incubated in a primary antibody solution of mouse anti-BrdU (1:250) in 1% BSA overnight at 4°C. Samples were rinsed and then incubated with secondary antibody solution including goat anti-mouse IgG AlexaFluor® 488 (1:250) and Hoechst 33342 (1:2000, nuclear label) in 1% BSA. After 1 hour at room temperature, samples were rinsed with high-volume PBS washes and stored in PBS at 4°C until use.

3.2.9. Imaging

PA hydrogels were imaged by confocal microscopy using a wet mount setup. PA hydrogels were inverted onto larger coverslips with excess PBS and placed on the microscope stage. For quantification methods that required lower feature resolution, samples were imaged using an Olympus IX81 inverted fluorescent microscope to reduce acquisition time. These included analyses for migration distance, nuclear orientation, proliferation, and cell morphology.

High-resolution confocal images were taken on an Olympus FluoView™ FV1000 confocal microscope for fibronectin, phospho-MLC, phospho-FAK, and VE-cadherin. Z-stacks were taken at 0.5 µm steps throughout the sample thickness using Olympus FluoView™ F1000 software.

3.2.10. Image Quantification

All quantification methods were as previously described in Chapter 2.

3.2.11. Statistics

All experiments were done in duplicate or triplicate. Unless otherwise noted, data are represented as mean ± standard error of the mean in order to better reflect the precision of the mean. The mean ± standard error of the mean were calculated from averages of measures from 5+ images per sample from 2+ samples per condition. One-way ANOVA and post-hoc testing (least significance difference) were used to compare metrics across substrate stiffnesses. # denotes p-values less than 0.05, * denotes p-values less than 0.01, ** denotes p-values less than 0.001, and “n.s.” denotes a “non-significant” difference.

3.3. Results

3.3.1. Migration Distance as a Function of Substrate Stiffness

PAEC migration distance from 3 to 48 hours was measured for samples on 4, 14, and 50 kPa PA gels (Figure 3.4). Representative fluorescent microscopy composite images of cell outward migration are shown in Figure 3.4A. Before 12 hours, there was no difference in migration distance for PAEC on different stiffness substrates. However, cells on 14 kPa and 50 kPa substrates migrated significantly farther as compared to 4 kPa substrates by 24 hours ($F = 23.14$, $p = 0.006$), 36 hours ($F = 65.58$, $p < 0.001$), and 48 hours ($F = 19.73$, $p = 0.008$). Average migration velocities between 12 and 24 hours were 9.94 ± 8.58, 18.87 ± 2.26, and 18.96 ± 0.99 μm/hour for 4, 14, and 50 kPa gels, respectively. However, migration slowed after 36 hours and plateaued for cells on each stiffness gel by 48 hours. Therefore, the 12-hour period between 12 and 24 hours appeared to be the most important time for substrate stiffness-related effects. For future experiments, these time points were the focus.

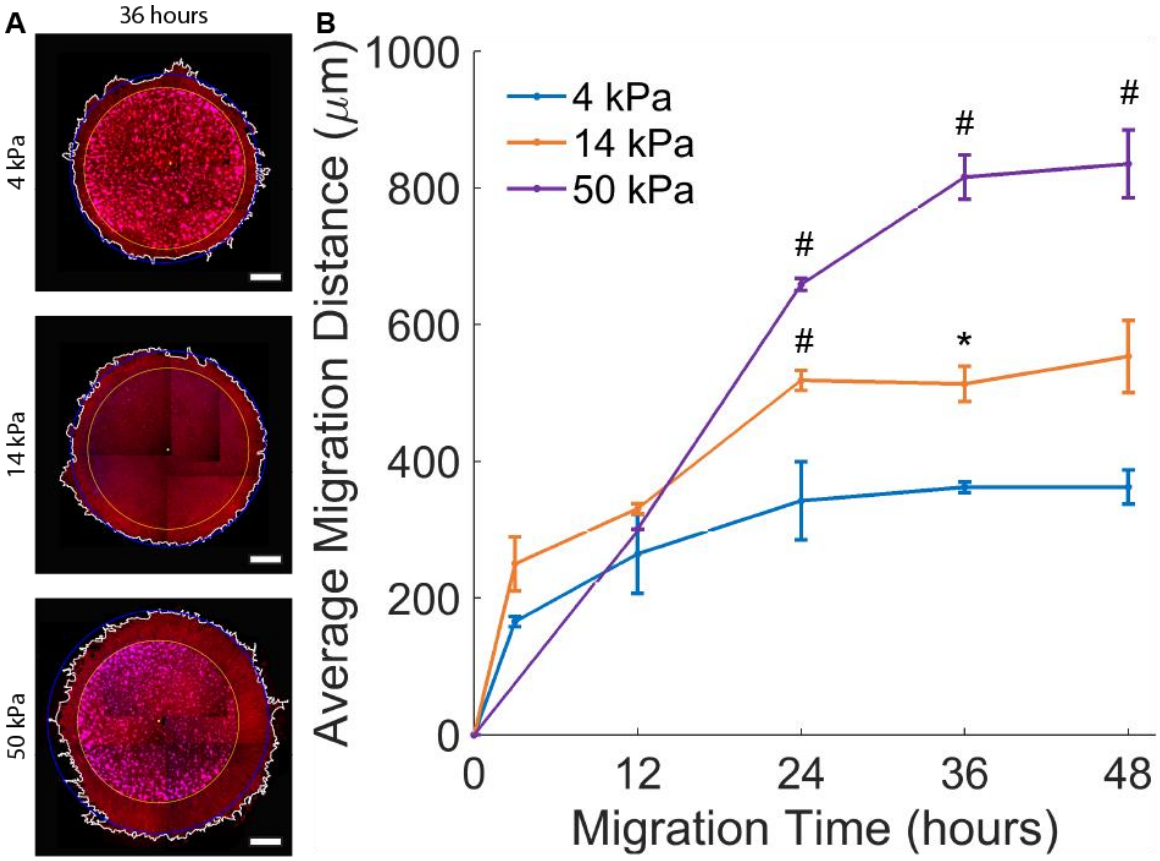

Figure 3.4: PAEC collectively migrated faster and farther on stiffer substrates. (A) Samples were labeled for F-actin (phalloidin, red) and nuclei (Hoescht, blue). Composite images were stitched together to reconstruct the sample. The radial difference between the average migration distance (blue circle) and original cage position (yellow circle) was the final output graphed in (B). #p<0.05; *p<0.01; markers for 50 kPa samples were compared to 14 kPa; markers for 14 kPa were compared to 4 kPa. Scale bars = 1000 µm.

3.3.2. Cellular Orientation as a Function of Substrate Stiffness

Collective migration involves groups of cells directed toward a similar goal.[35] To assess PAEC orientation, the nuclear long axis angle relative to the global migration direction was measured for cells within fixed-width bands throughout the migratory front (Figure 3.5-3.7). Angle deviations ranged from -90° to 90° for each nucleus, with 0° being the most aligned.

At 0, 3, and 6 hours, PAEC did not show significantly different nuclear alignment among the three substrates. PAEC started to align on all substrates by 6 hours (data not shown). However by 12 hours, nuclei were more aligned on 14 kPa gels as compared to 4 and 50 kPa gels (Figure

3.5A,B). For cells on 14 and 50 kPa substrates, nuclei exhibited increased alignment with the migration direction in the bins 400-700 μm back from the interface (red and orange rose plots, Figure 3.5B). A similar trend is seen at 24 hours (Figure 3.6), with more variable nuclear alignment on 4 kPa gels as compared to 14 and 50 kPa gels. By 36 hours, the nuclear alignment differences among substrates were lost (Figure 3.7).

To further compare nuclear alignment, the average nuclear angle, percentage of nuclei aligned within 20° of the migration direction, as well as the angle distribution kurtosis and standard deviation were calculated and plotted as a function of distance from the migratory front (Figure 3.8). Nuclear alignment significantly differed with substrate stiffness at 12 hours ($F = 2.52$, $p < 0.0001$) and 24 hours ($F = 1.95$, $p = 0.004$). At 12 hours, nuclei were 74-126% and 43-58% more aligned at the peak zones 400-600 μm from the migratory interface on 14 kPa substrates compared to 4 kPa and 50 kPa substrates, respectively. By 24 hours, nuclei were 56-85% more aligned 500-700 μm from the migratory interface on 14 kPa substrates compared to 4 kPa substrates, showing no difference on 50 kPa substrates. In addition, nuclei were 55% more aligned 600 μm from the migratory interface on 50 kPa substrates compared to 4 kPa substrates. At 12 and 24 hours, average nuclear angle and the percentage of aligned nuclei were highest in cells on 14 kPa gels. The nuclear angle distribution for cells on 14 kPa gels also showed higher kurtosis, indicating more nuclei clustered around 0° deviation from the migration direction. The standard deviations decreased in the same bands with highest alignment and kurtosis. By 36 hours, the degree of nuclear alignment did not differ among the substrates ($F = 1.04$, $p = 0.41$).

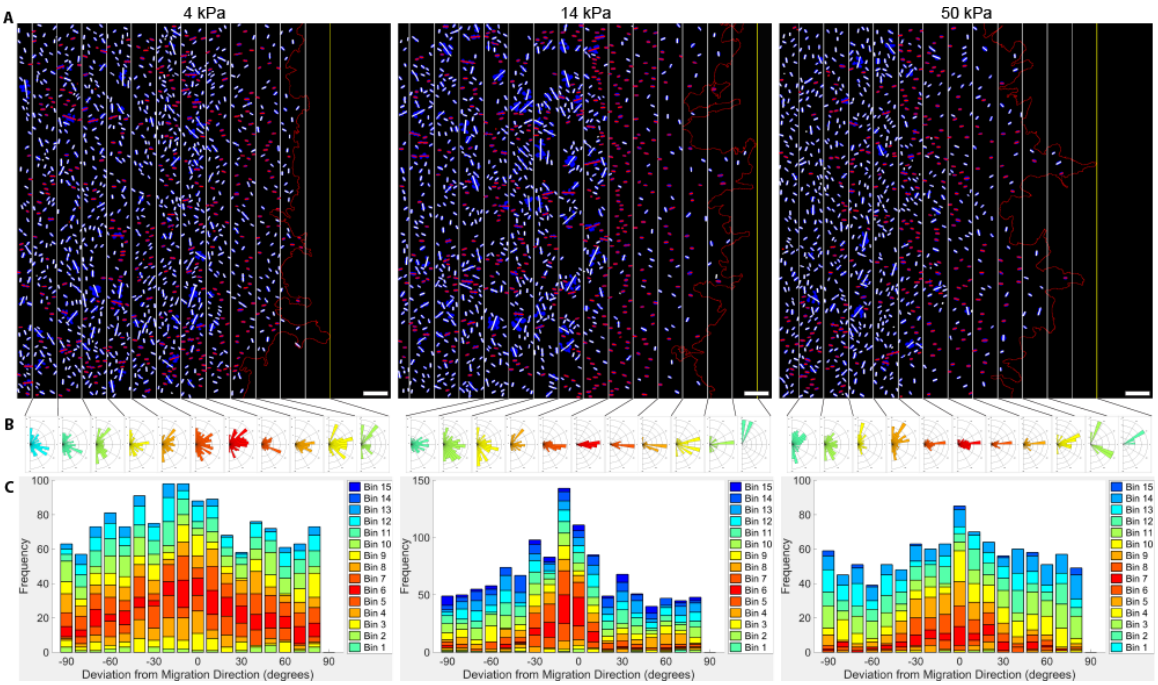

Figure 3.5: PAEC were more aligned with the migration direction on stiffer substrates at 12 hours. (A) Nuclei (blue) with short lines (red = within 20° of the global migration direction, white = greater than 20° from the global migration direction) indicating their long axis angle. The global migration direction is perpendicular to the bin lines. (B) Nuclear angle frequency rose plots for each bin. 0° (to the right) represent nuclei with no deviation from the global migration direction. Values ranged from [-90°,90°]. The rose plot for the bin with the highest percentage of aligned nuclei is red. (C) Stacked histograms with a similar color scheme as described in (B). Scale bars and distance between bin lines = 100 µm**.**

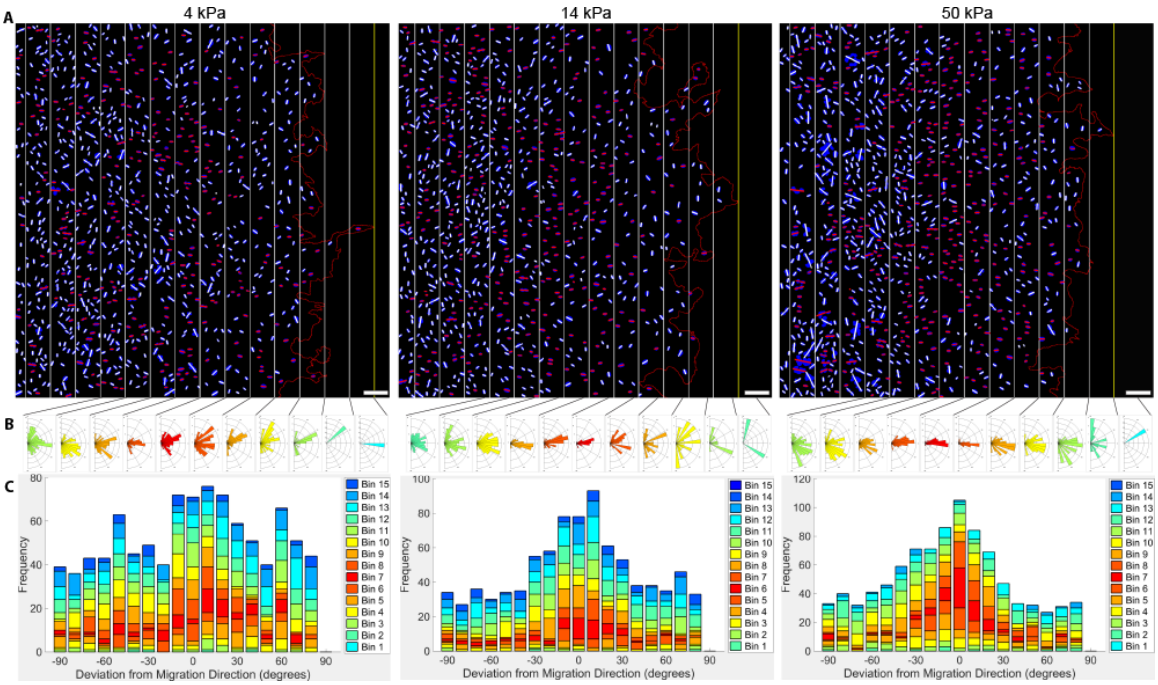

Figure 3.6: PAEC continued to be more aligned with the migration direction on stiffer substrates at 24 hours. (A) Nuclei (blue) with short lines (red = within 20° of the global migration direction, white = greater than 20° from the global migration direction) indicating their long axis angle. The global migration direction is perpendicular to the bin lines. (B) Nuclear angle frequency rose plots for each bin. 0° (to the right) represent nuclei with no deviation from the global migration direction. Values ranged from [-90°,90°]. The rose plot for the bin with the highest percentage of aligned nuclei is red. (C) Stacked histograms with a similar color scheme as described in (B). Scale bars and distance between bin lines = 100 µm.

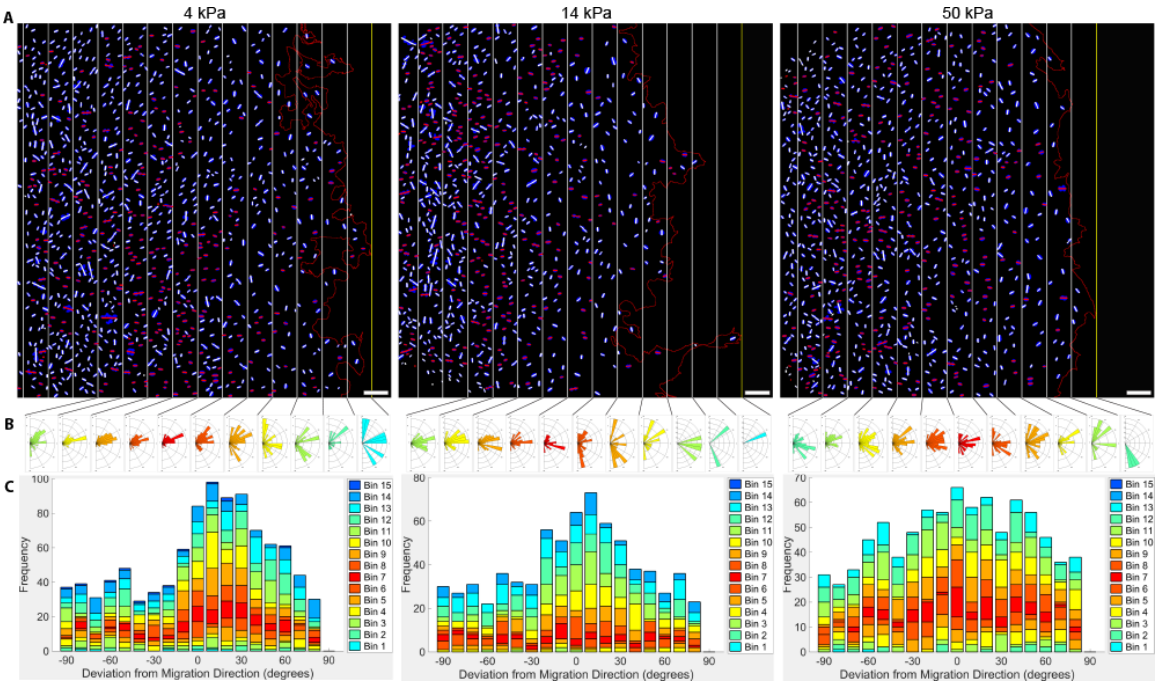

Figure 3.7: Nuclear alignment was similar for cells on all substrate stiffnesses at 36 hours. (A) Nuclei (blue) with short lines (red = within 20° of the global migration direction, white = greater than 20° from the global migration direction) indicating their long axis angle. The global migration direction is perpendicular to the bin lines. (B) Nuclear angle frequency rose plots for each bin. 0° (to the right) represent nuclei with no deviation from the global migration direction. Values ranged from [-90°,90°]. The rose plot for the bin with the highest percentage of aligned nuclei is red. (C) Stacked histograms with a similar color scheme as described in (B). Scale bars and distance between bin lines = 100 µm.

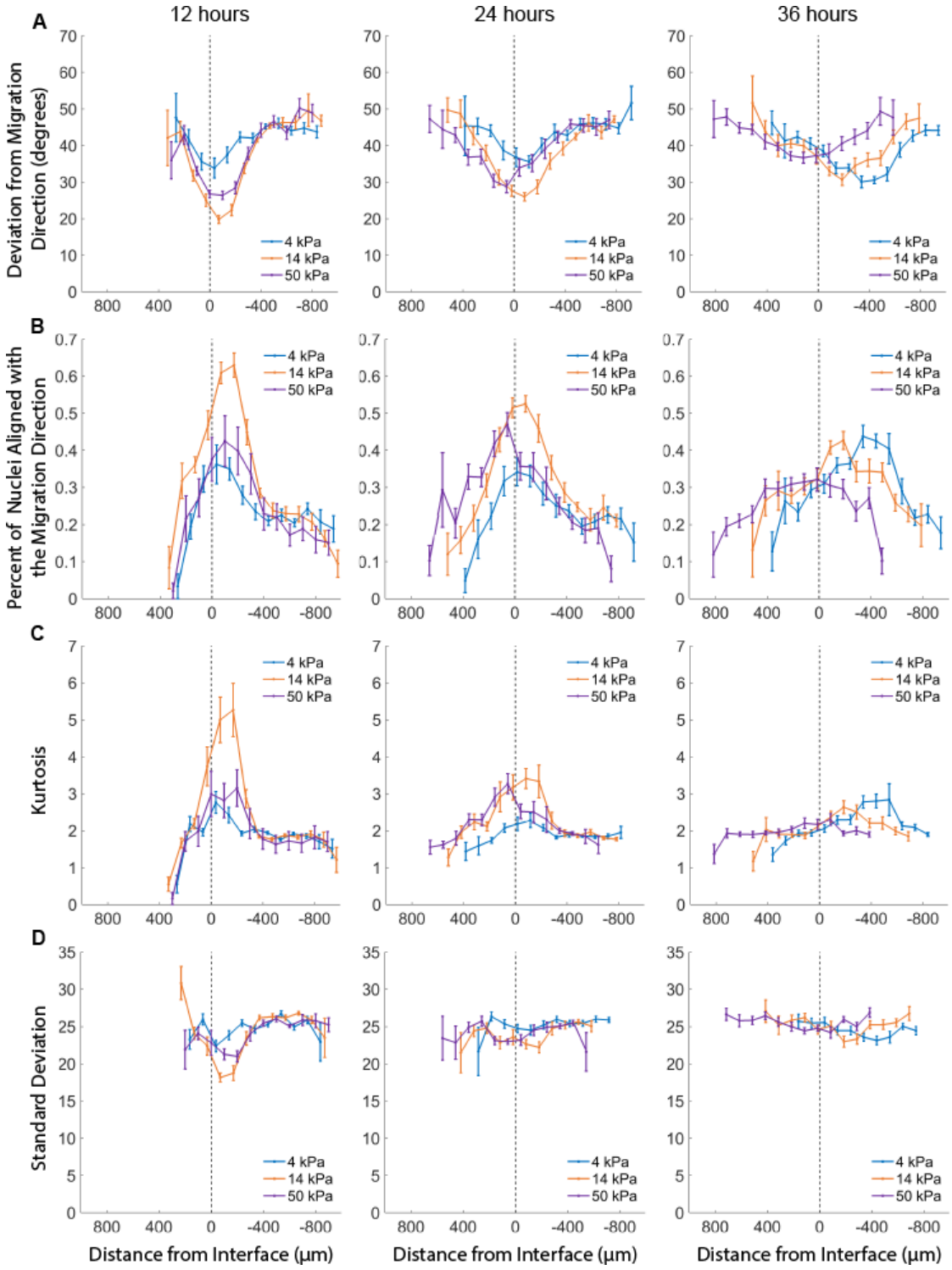

Figure 3.8: PAEC were most aligned on 14 kPa substrates within 200 μm of the original cage position at 12 and 24 hours. Four metrics were used to compare differences in nuclear alignment relative to the migration direction: (A) average angle deviation from the migration direction, (B) percent of nuclei aligned with the migration direction, (C) kurtosis of nuclear angle distribution, and (D) standard deviation of nuclear angle distribution. Along the x-axis, 0 is the original cage position and cells migrate in the positive direction.

To understand how the zone of maximal alignment changed over time, it was measured for each substrate and shown as a relative distance from the moving interface (left, Figure 3.9) or as a distance relative to the original cage position at 0 μm (right, Figure 3.9). The zone of maximal alignment relative to the moving interface did not change with stiffness ($F = 2.26$, $p = 0.06$). However, there were differences in the zones of maximal alignment distance relative to the original cage position ($F = 6.23$, $p = 0.0002$). Zones of maximal alignment were 237.3 and 232.4 μm farther ahead on 50 kPa substrates compared to 14 kPa substrates at 24 and 36 hours, respectively ($p < 0.05$). The zone of maximal alignment was 331.1 μm farther ahead on 14 kPa substrates compared to 4 kPa substrates at 36 hours ($p < 0.01$). The zones of maximal alignment only moved forward on 50 kPa substrates, but remained behind the original cage position on 4 kPa. The zone of maximal alignment did not move away from the original cage position on 14 kPa substrates ($F = 0.47$, $p = 0.63$).

These data suggest that nuclear alignment with the migration direction, a measure of cell directedness during collective migration, is a function of substrate stiffness, distance from the migratory front, and time. On 14 kPa substrates, PAEC were more aligned with the migration direction compared to 4 kPa and 50 kPa substrates. This alignment was the farthest forward on 50 kPa substrates and moved farther back on 4 kPa and 14 kPa substrates, relative to the original cage position. Using these data, we defined three distinct zones in the migratory front based on the degree of nuclear alignment: (1) interface zone at the edge of the migrating cell cluster (nuclei not aligned in the migration direction), (2) migratory zone a few cells back from the migrating edge (nuclei more aligned with the migration direction), and (3) confluent zone behind the migratory zone (PAEC no longer aligned with the migration direction). Cells within these zones were examined in future experiments.

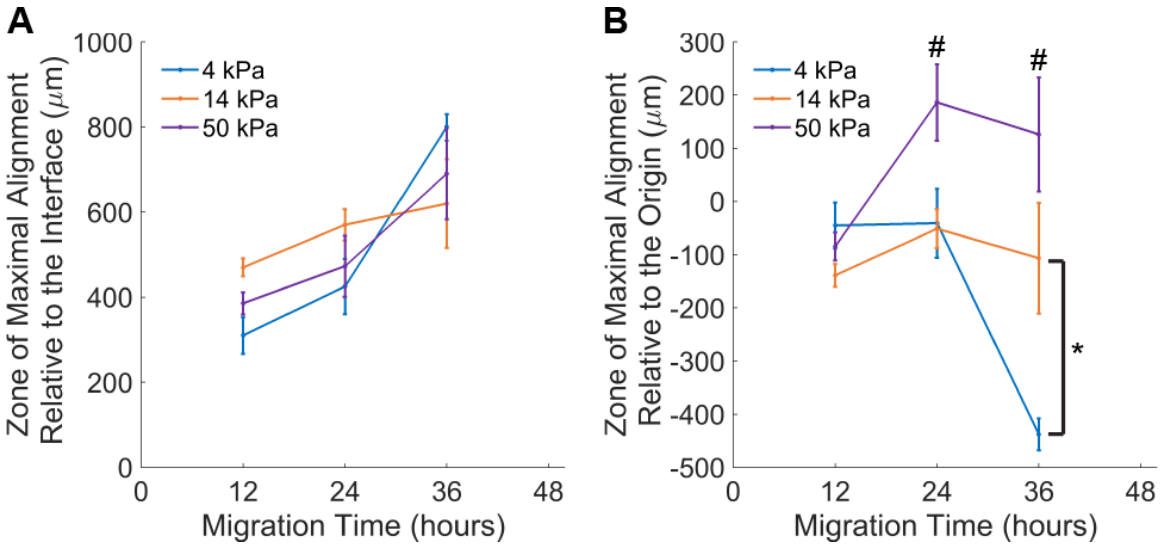

Figure 3.9: The zone of maximal alignment relative to the migratory interface did not differ with substrate stiffness. The zone of maximal alignment relative to the cage position only moved forward on the stiffest substrate. The zone within the migratory front with the peak nuclear alignment was plotted as a function of time. The zones were measured relative to the migratory interface (A) or the original cage position at 0 μm (B). #$p < 0.05$; *$p < 0.01$; compared to 14 kPa unless otherwise noted.

3.3.3. Cellular Morphology as a Function of Substrate Stiffness

To determine whether cell morphology contributed to increased migration distance in cells on stiffer substrates, cell size and area were measured using a custom MATLAB algorithm that quantified the morphological features of PAEC in the migratory front after 12 (Figure 3.10) and 24 hours (Figure 3.11). At 12 hours, PAEC were 46% larger on 14 and 50 kPa gels compared to 4 kPa substrates (Figure 3.10D, $F = 21.78$, $p < 0.001$). At 24 hours, PAEC were 16% larger on 14 kPa and 50 kPa substrates compared to 4 kPa substrates (Figure 3.11D, $F = 7.01$, $p = 0.004$). The aspect ratio show similar trends with 15% and 4% increases in cell elongation on the two stiffer substrates compared to 4 kPa substrates at 12 and 24 hours, respectively (Figure 3.8C, $F = 26.02$, $p < 0.001$; Figure 3.10C, $F = 6.26$, $p = 0.006$). These data suggest that increased PAEC elongation and area contribute to the increased migration distance and velocity with substrate stiffness.

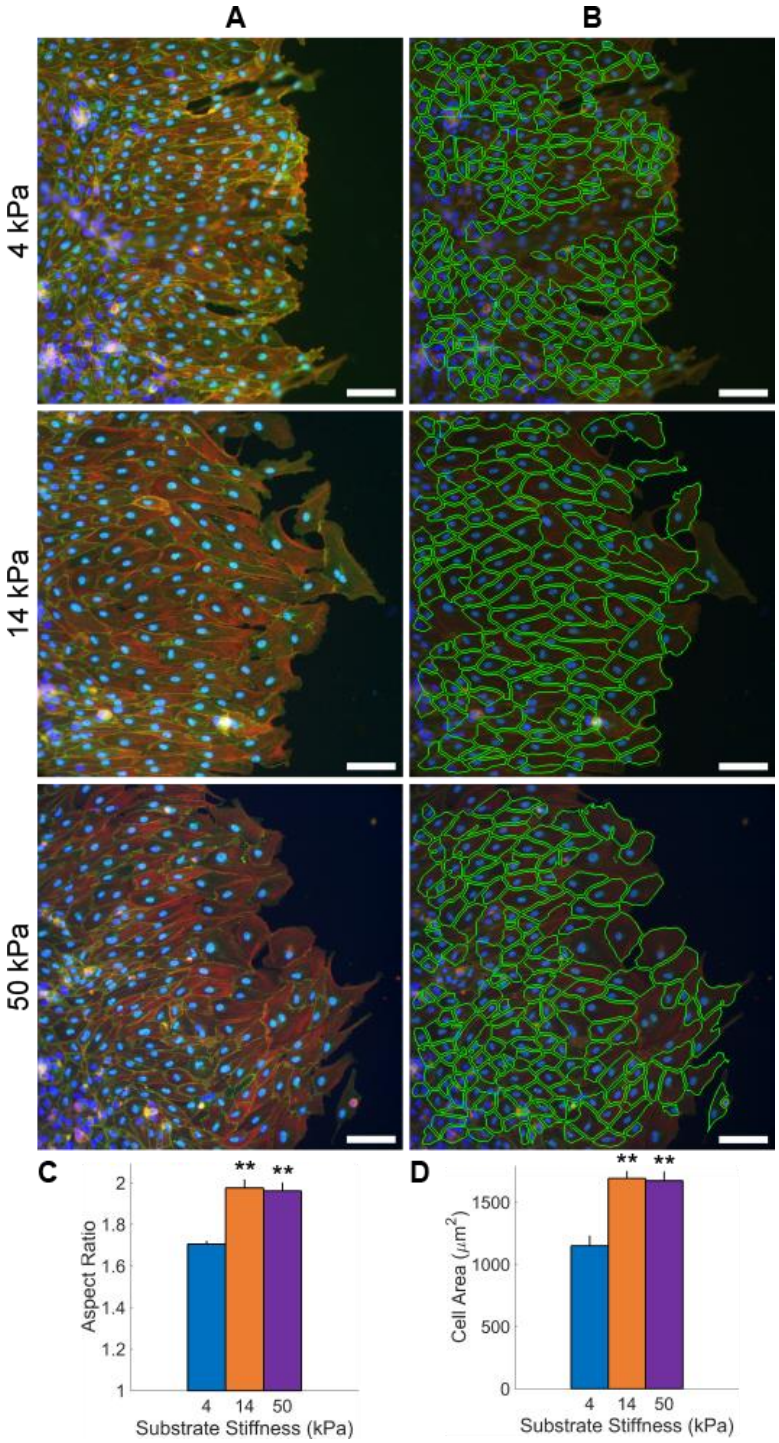

Figure 3.10: PAEC were larger and more elongated on stiffer substrates at 12 hours of migration. (A) Confocal microscopy images of migrating samples labeled for β-catenin (green), F-actin (red), and nuclei (blue). (B) Green boundaries delineate cell shape from a custom MATLAB algorithm. Aspect ratio (C) and area (D) of the outlined cells. Scale bars = 50 μm. **p < 0.001; compared to cells on 4 kPa gels.

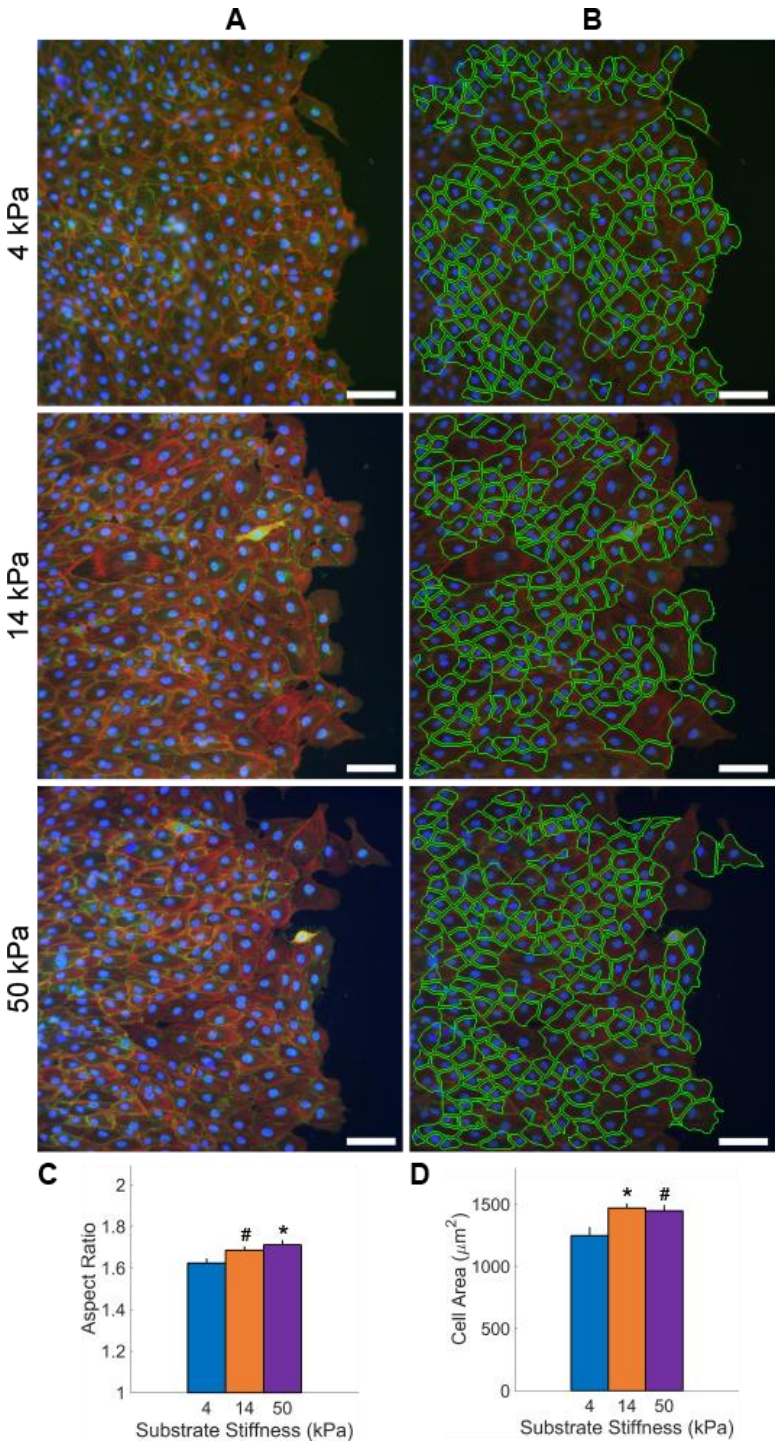

Figure 3.11: PAEC were larger and more elongated on stiffer substrates at 24 hours of migration. (A) Confocal microscopy images of migrating samples labeled for β-catenin (green), F-actin (red), and nuclei (blue). (B) Green boundaries delineate cell shape from a custom MATLAB algorithm. Aspect ratio (C) and area (D) of the outlined cells. Scale bars = 50 μm. #$p < 0.05$; *$p < 0.01$; compared to cells on 14 kPa gels.

3.3.4. Fibronectin Fiber Orientation as a Function of Substrate Stiffness

Fibronectin fiber length and angle distributions were measured in PAEC on collagen-coated PA hydrogels of varied stiffness to determine if fiber alignment and length varied with substrate stiffness. First, we note that PAEC secrete and remodel fibronectin on collagen-coated PA hydrogels (Figure 3.12-3.20). Similar fibronectin networks were seen in serum-free conditions, confirming that fibronectin is secreted (data not shown). At 12 hours, there were no differences in fibronectin fiber angle among substrates of any stiffness. However, by 24 hours, fibers were more aligned with the migration direction in the migratory zone on the 14 and 50 kPa gels as compared to the 4 kPa gels (Figure 3.21). Fibers on 14 and 50 kPa gels had average angles that were 66% and 61% lower than fiber angles on 4 kPa substrates, respectively. Furthermore, fibers on 14 and 50 kPa gels had a 314% and 285% increase in percent of fibers aligned within 20° of the migration direction, respectively. Similar trends were seen for kurtosis and standard deviation of the distributions. No differences were seen in the interface and confluent zones. The fibronectin fiber trends continued for the 14 kPa gels through 36 hours, showing a 62% decrease in fiber angle, a 352% increase in percent of aligned fibers, and a 53% decrease in fiber angle standard deviation compared to 4 kPa gels. Fibers on 50 kPa gels were consistently aligned, but not always in the migration direction. Fibronectin fiber length did not significantly differ with substrate stiffness (data not shown).

We noticed qualitative differences between fibronectin fiber appearance on different substrates. Fibers appeared in more of a network on 4 kPa substrates with clustering of fibers between cells. On 14 kPa and 50 kPa substrates, fibers were more individual and aligned in parallel uniformly throughout the sample.

These results show that fibronectin fiber alignment increases with substrate stiffness specifically in the migratory zone, which is the same region where PAEC are most aligned.

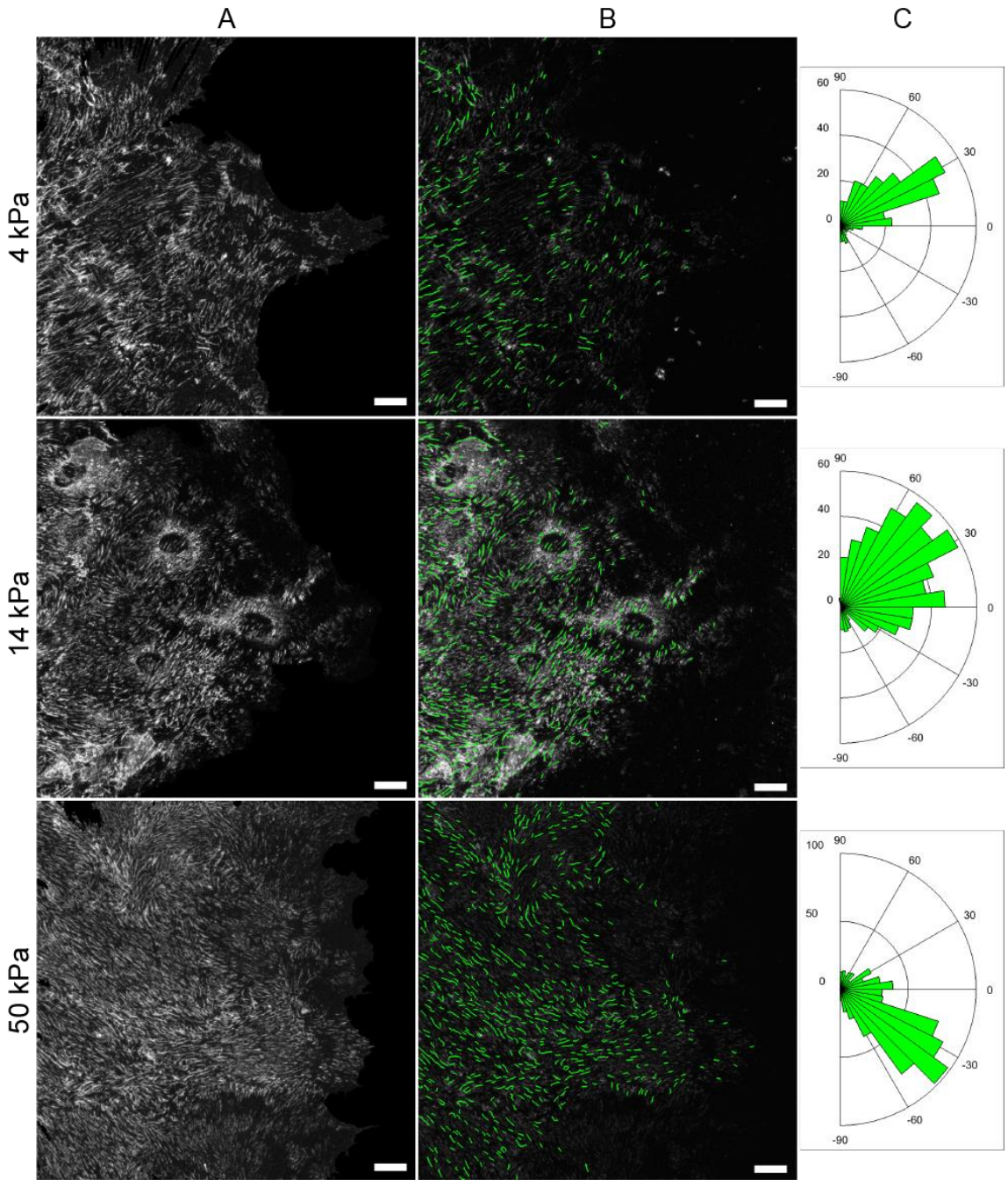

Figure 3.12: Fibronectin fibers were networked on 4 kPa substrates and uniformly dispersed in individual parallel fibers on 14 kPa and 50 kPa substrates in the interface zone at 12 hours. (A) Confocal microscopy images of fibronectin fibers. (B) MATLAB output showing identified fibers (green) overlaying the original image. (C) Fiber angle distribution. Scale bars = 20 µm.

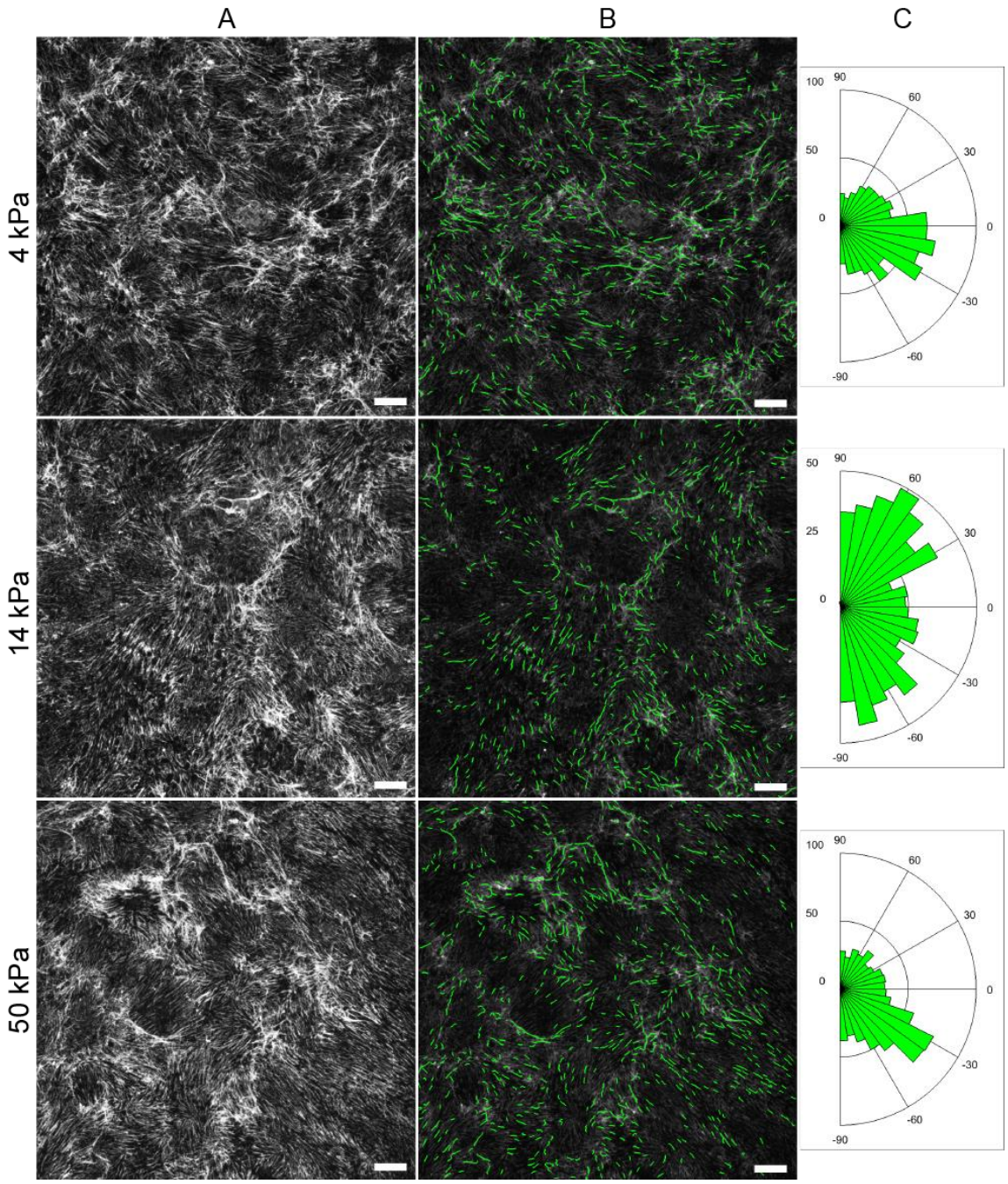

Figure 3.13: Fibronectin fibers were networked on all substrates in the migratory zone at 12 hours. (A) Confocal microscopy images of fibronectin fibers. (B) MATLAB output showing identified fibers (green) overlaying the original image. (C) Fiber angle distribution. Scale bars = 20 µm.

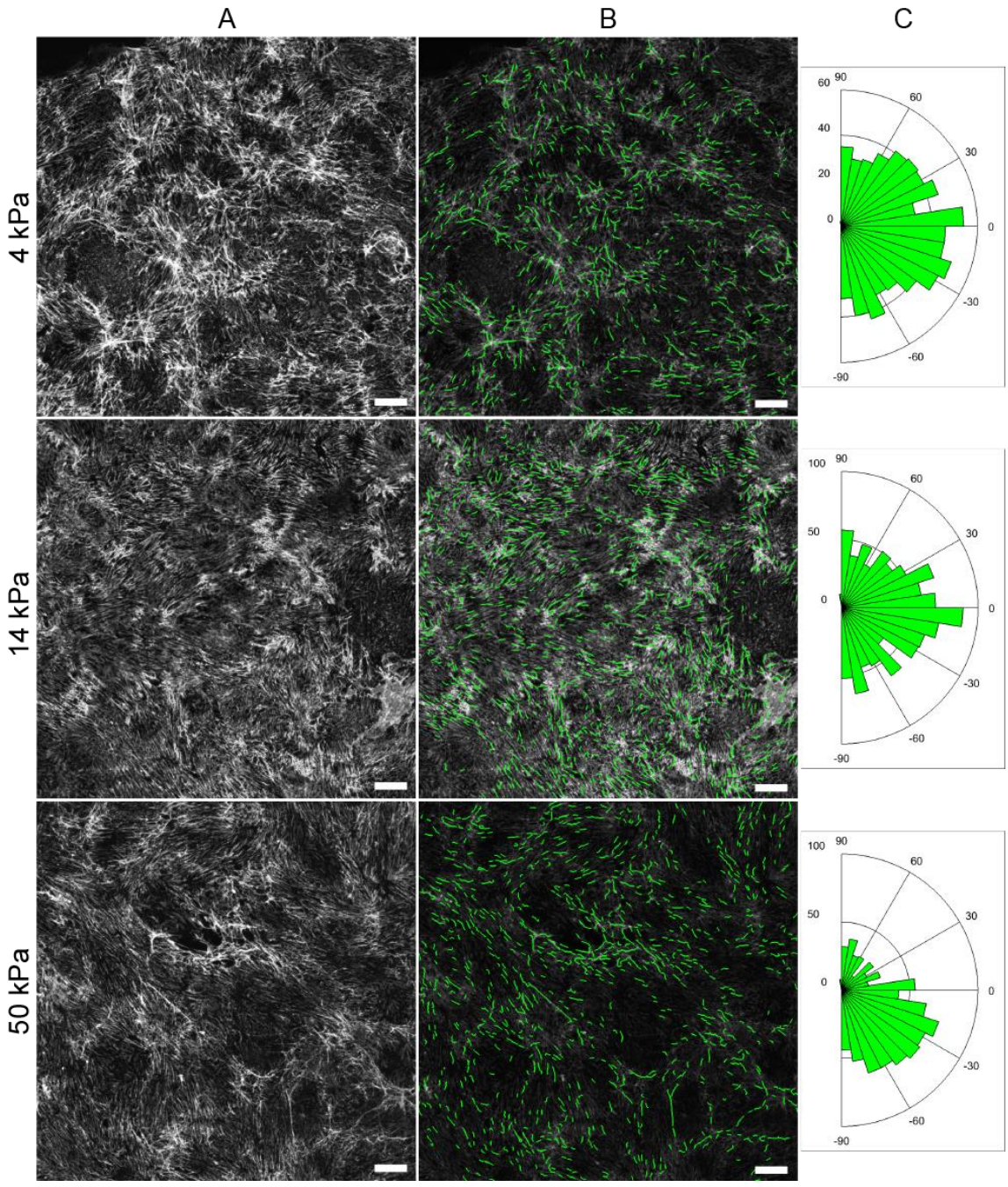

Figure 3.14: Fibronectin fibers were networked on all substrates in the confluent zone at 12 hours. (A) Confocal microscopy images of fibronectin fibers. (B) MATLAB output showing identified fibers (green) overlaying the original image. (C) Fiber angle distribution. Scale bars = 20 µm.

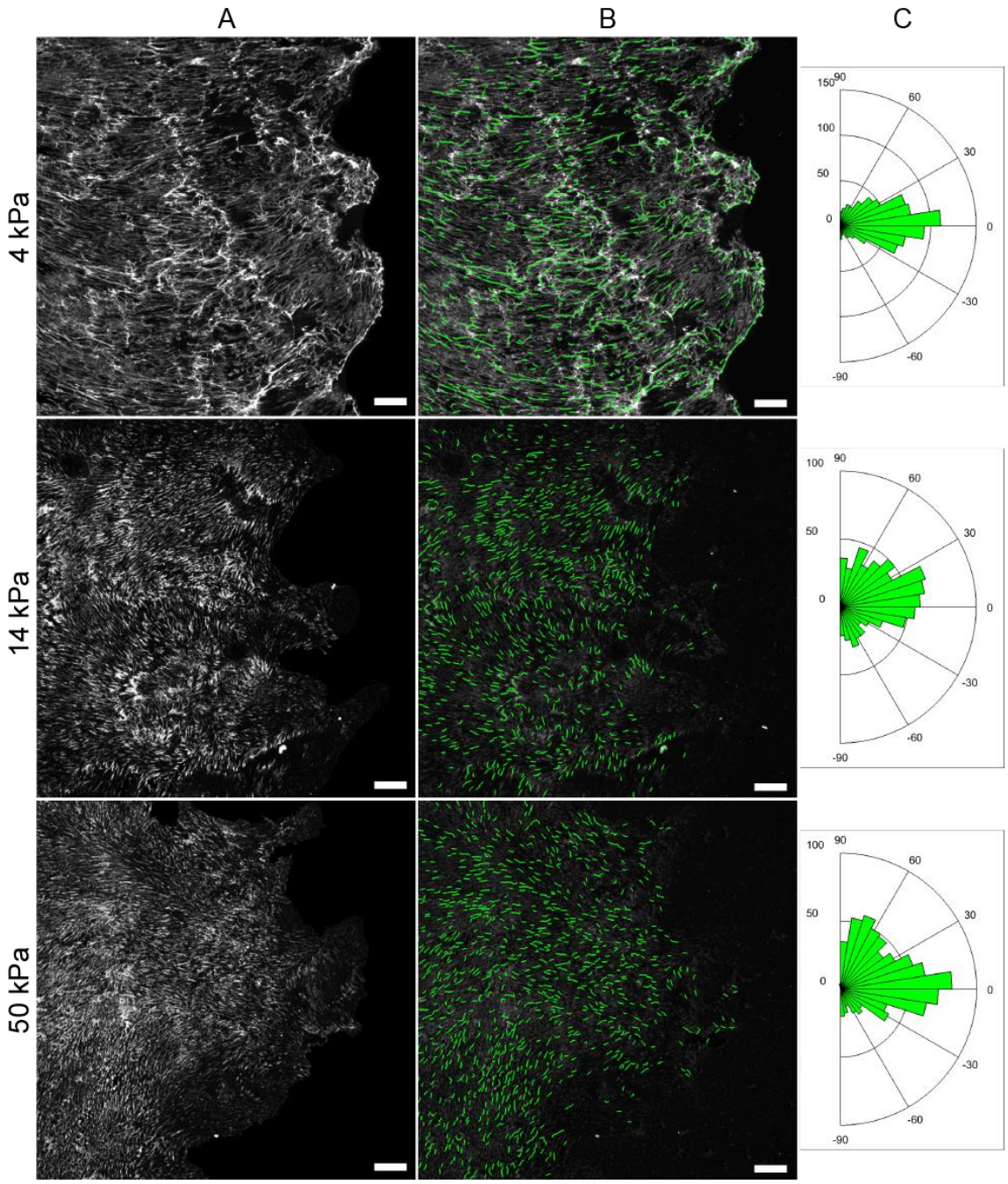

Figure 3.15: Fibronectin fibers were uniformly dispersed in individual parallel fibers on 14 kPa and 50 kPa substrates in the interface zone at 24 hours, unlike 4 kPa substrates with fibers clustered in bright spots. **(**A) Confocal microscopy images of fibronectin fibers. (B) MATLAB output showing identified fibers (green) overlaying the original image. (C) Fiber angle distribution. Scale bars = 20 µm.

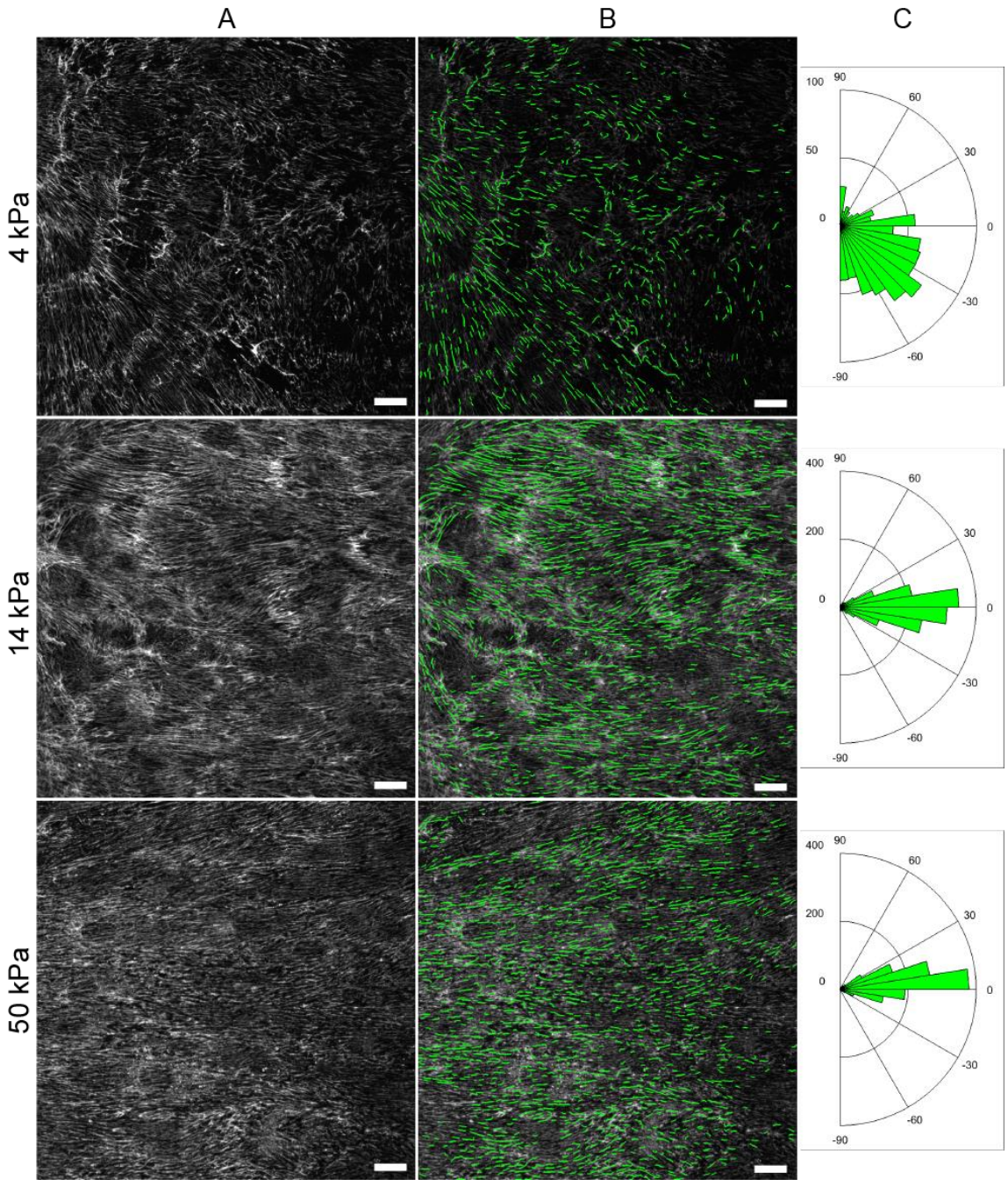

Figure 3.16: Fibronectin fibers were networked on 4 kPa substrates and uniformly dispersed in individual parallel fibers on 14 kPa and 50 kPa substrates in the migratory zone at 24 hours. (A) Confocal microscopy images of fibronectin fibers. (B) MATLAB output showing identified fibers (green) overlaying the original image. (C) Fiber angle distribution. Scale bars = 20 µm.

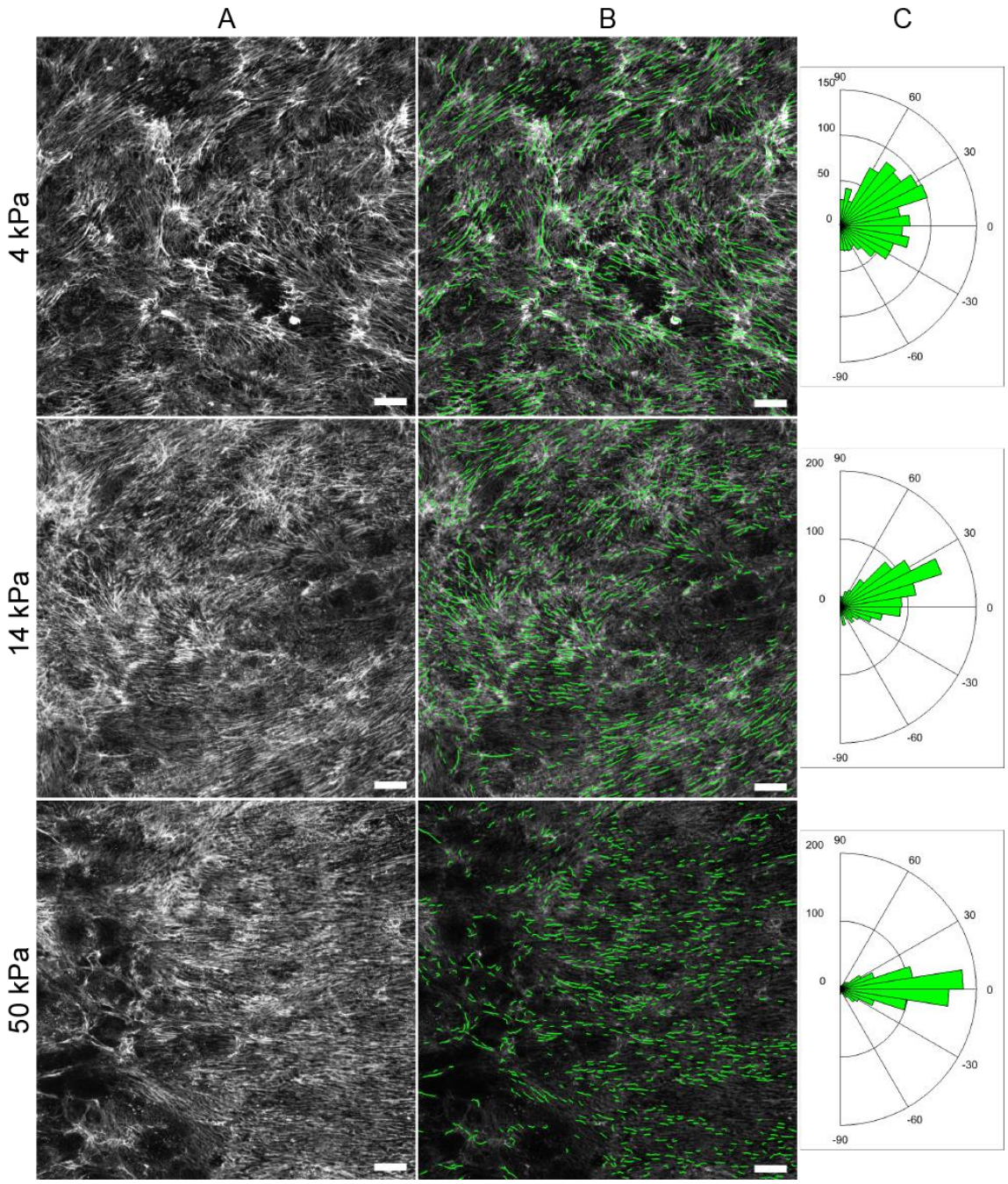

Figure 3.17: Fibronectin fibers were uniformly dispersed in individual parallel fibers on 14 kPa and 50 kPa substrates in the interface zone at 24 hours, unlike 4 kPa substrates with fibers clustered in bright spots. (A) Confocal microscopy images of fibronectin fibers. (B) MATLAB output showing identified fibers (green) overlaying the original image. (C) Fiber angle distribution. Scale bars = 20 µm.

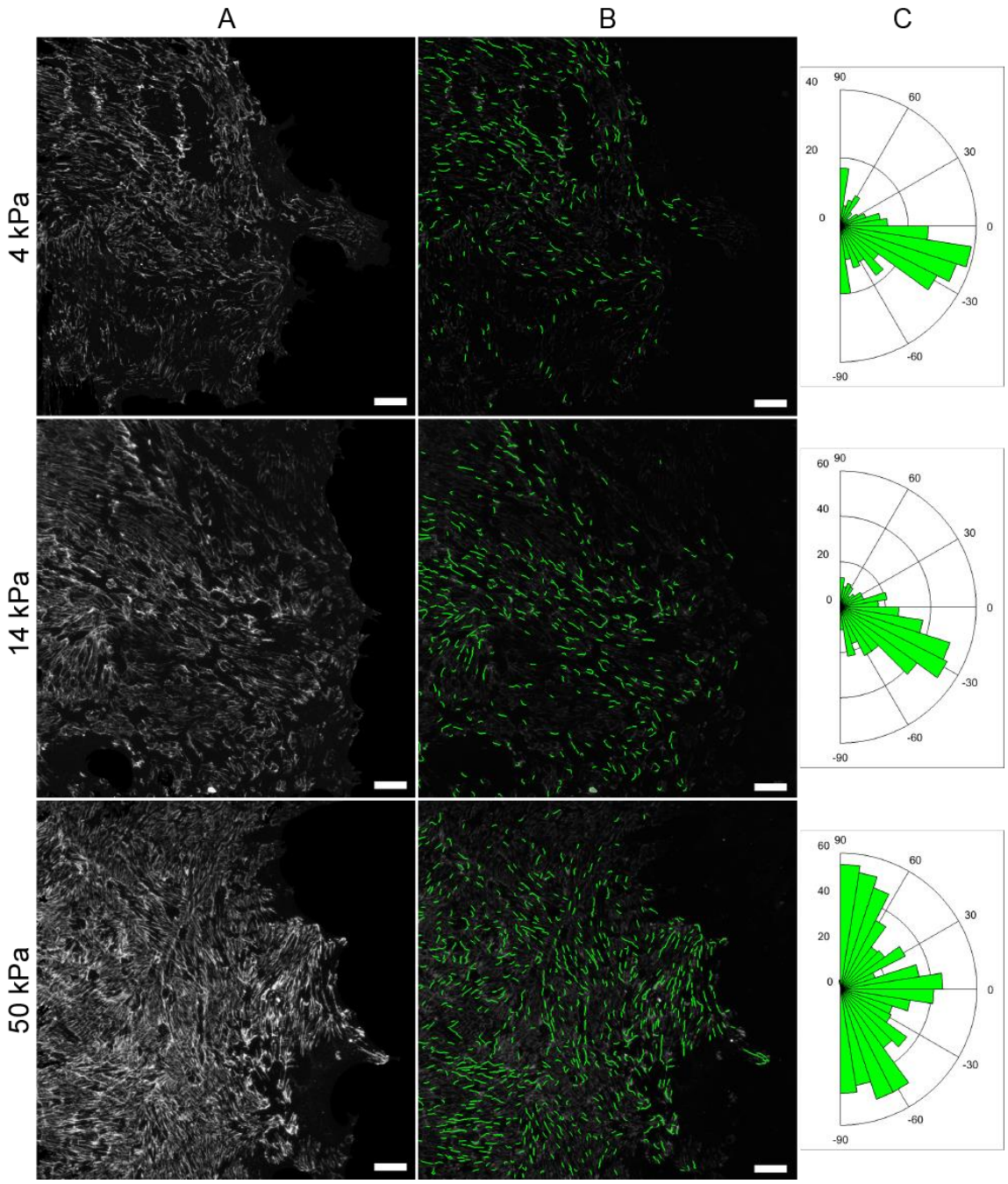

Figure 3.18: There were fewer fibronectin fibers on 4 kPa substrates and fibronectin was uniformly dispersed in individual parallel fibers on 14 kPa and 50 kPa substrates in the interface zone at 36 hours. (A) Confocal microscopy images of fibronectin fibers. (B) MATLAB output showing identified fibers (green) overlaying the original image. (C) Fiber angle distribution. Scale bars = 20 µm.

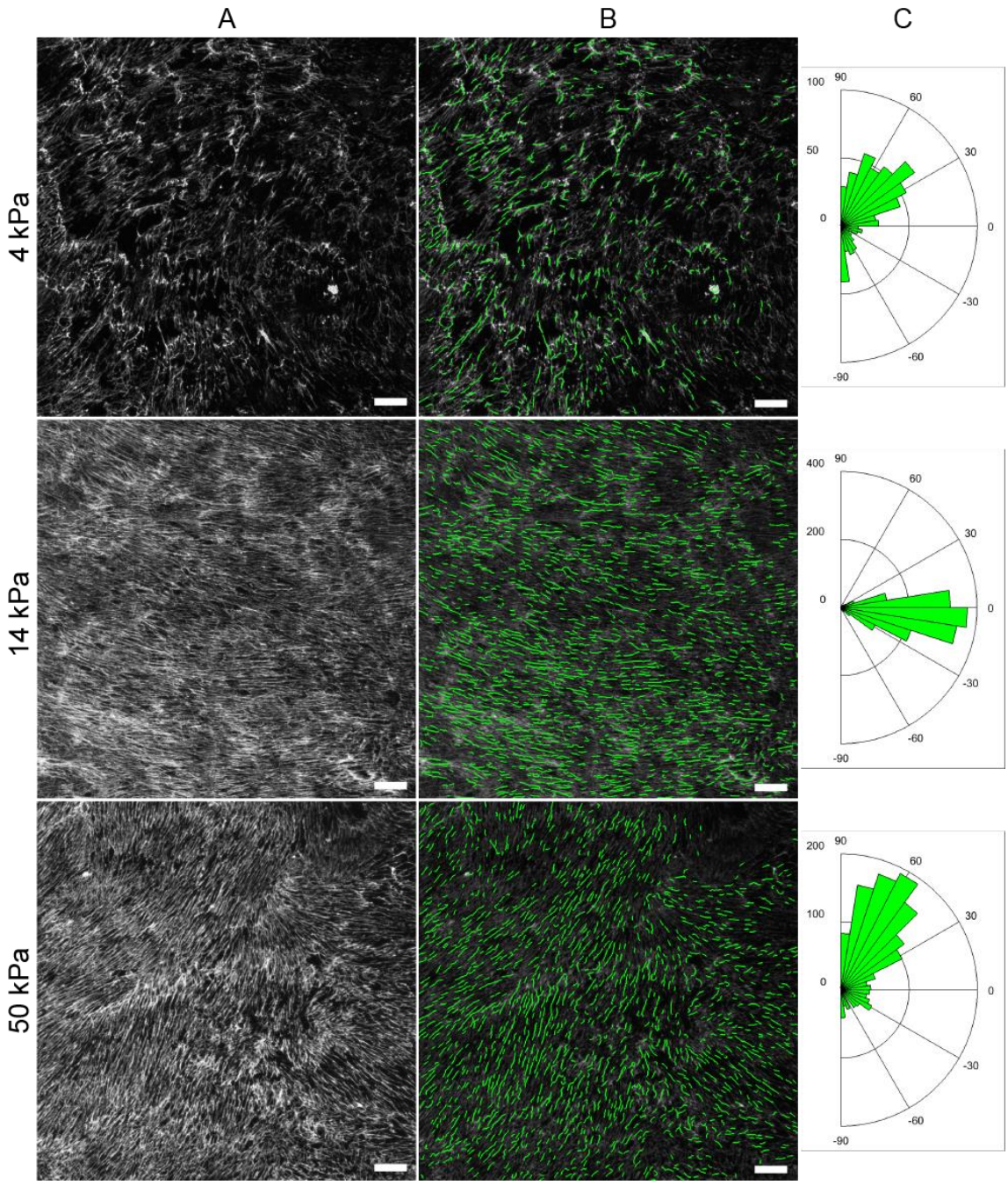

Figure 3.19: There were fewer fibronectin fibers on 4 kPa substrates and fibronectin was uniformly dispersed in individual parallel fibers on 14 kPa and 50 kPa substrates in the migratory zone at 36 hours. (A) Confocal microscopy images of fibronectin fibers. (B) MATLAB output showing identified fibers (green) overlaying the original image. (C) Fiber angle distribution. Scale bars = 20 µm.

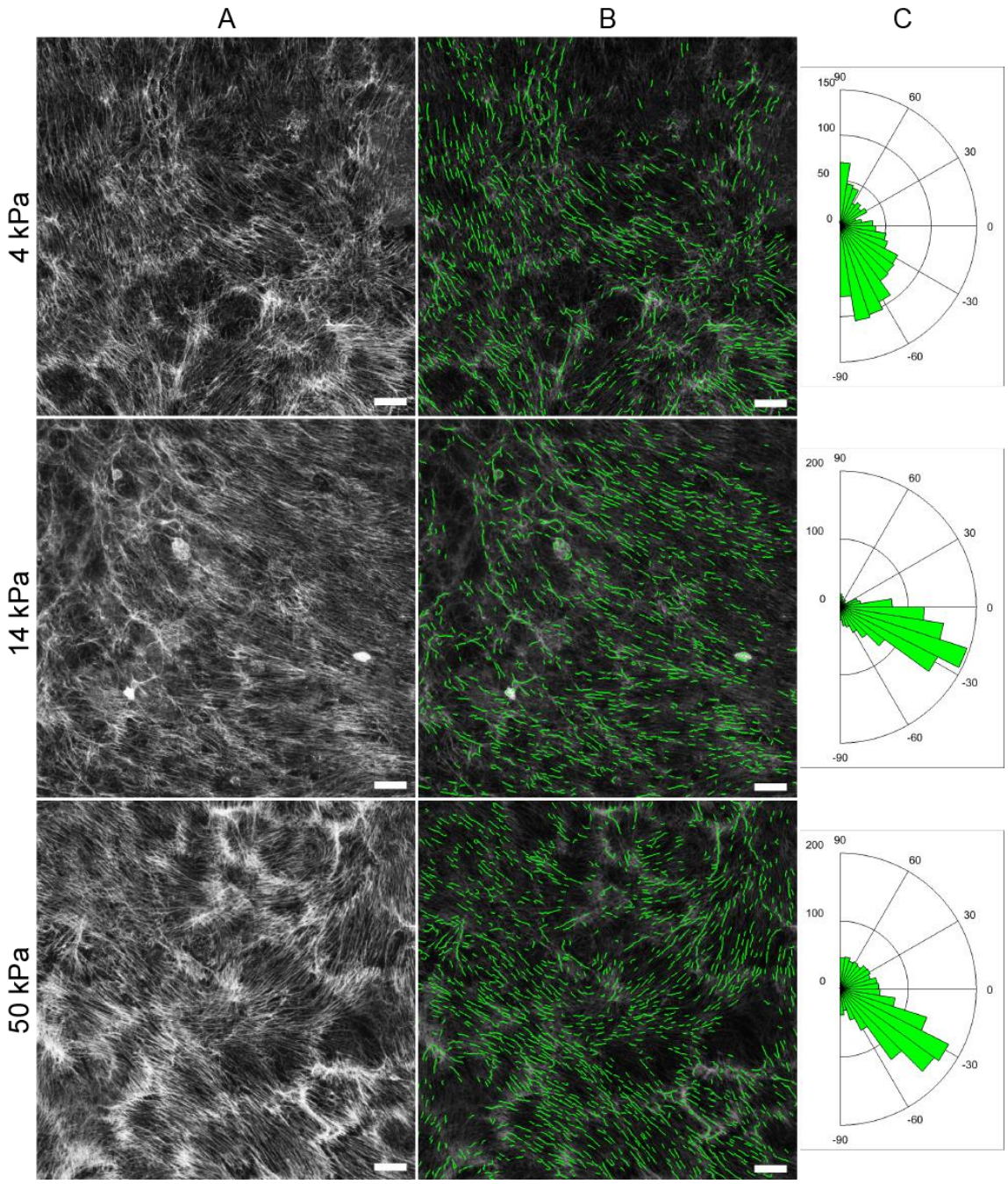

Figure 3.20: Fibronectin fibers were networked on all substrates in the interface zone at 36 hours. (A) Confocal microscopy images of fibronectin fibers. (B) MATLAB output showing identified fibers (green) overlaying the original image. (C) Fiber angle distribution. Scale bars = 20 µm.

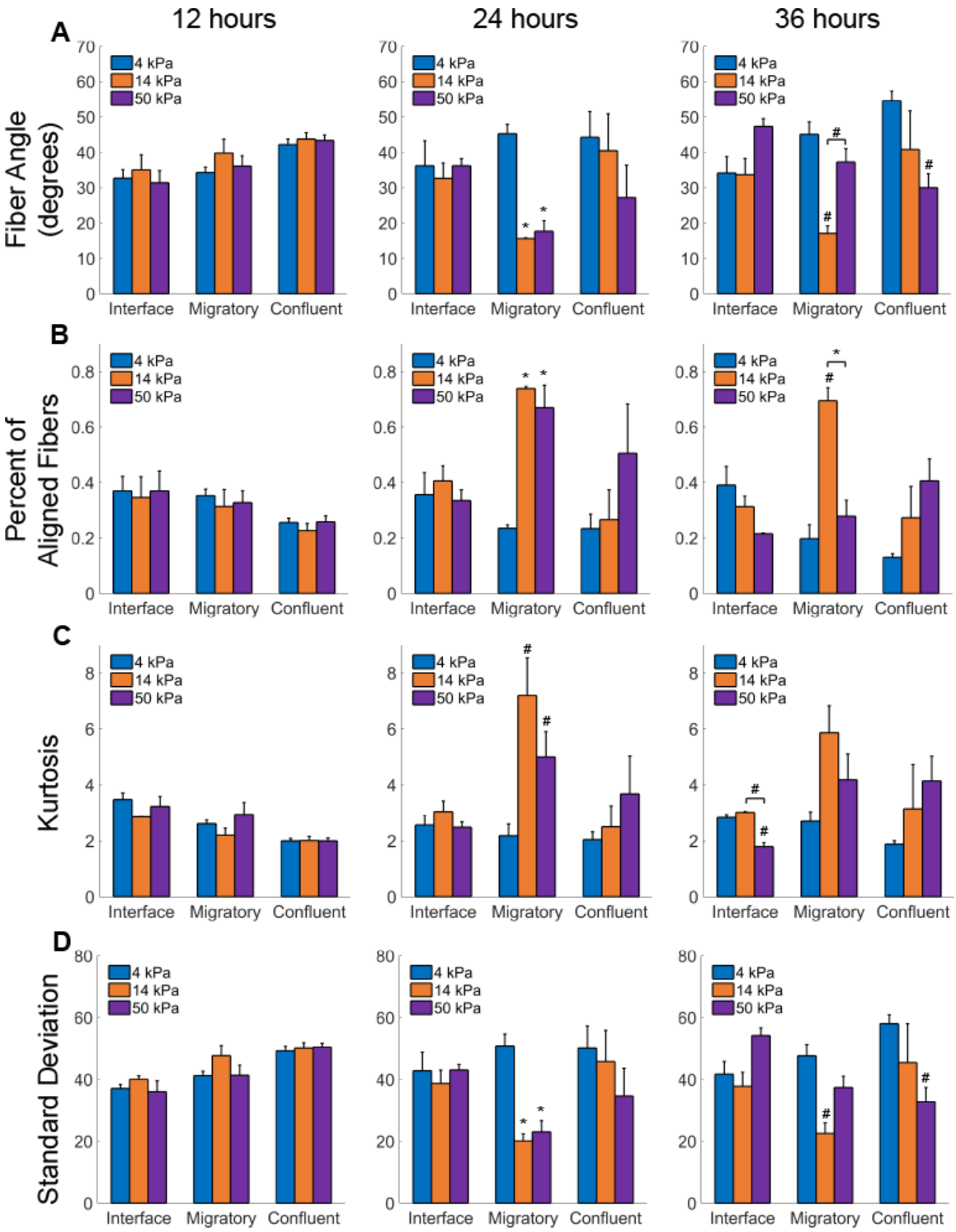

Figure 3.21: Fibronectin fibers were most aligned in the migratory zones at 24 hours on 14 kPa and 50 kPa substrates. (A) Average fiber angle, (B) percent of fibers aligned within 20° of the migration direction, (C) kurtosis of the fiber angle distribution, and (D) standard deviation of the fiber angle distribution for each zones on 4, 14, and 50 kPa gels. #$p < 0.05$; *$p < 0.01$; compared to 4 kPa within the same zone unless otherwise noted.

3.3.5. Togetherness as a Function of Substrate Stiffness

Togetherness is a defining characteristic of collective migration. To measure togetherness, we labelled for VE-cadherin and assessed focal cadherin complexes. PAEC on 4 kPa gels had diffuse VE-cadherin while PAEC on 14 and 50 kPa substrates had VE-cadherin organized in larger focal complexes at the cell membrane (Figure 3.22). The focal cadherin complexes on stiffer substrates are flanked by large gaps. PAEC area and elongation both increase with stiffness (Figure 3.10-3.11). Thus while membrane-to-membrane contact is greater on soft substrates, cadherin complexes are larger and more focal on stiffer substrates.

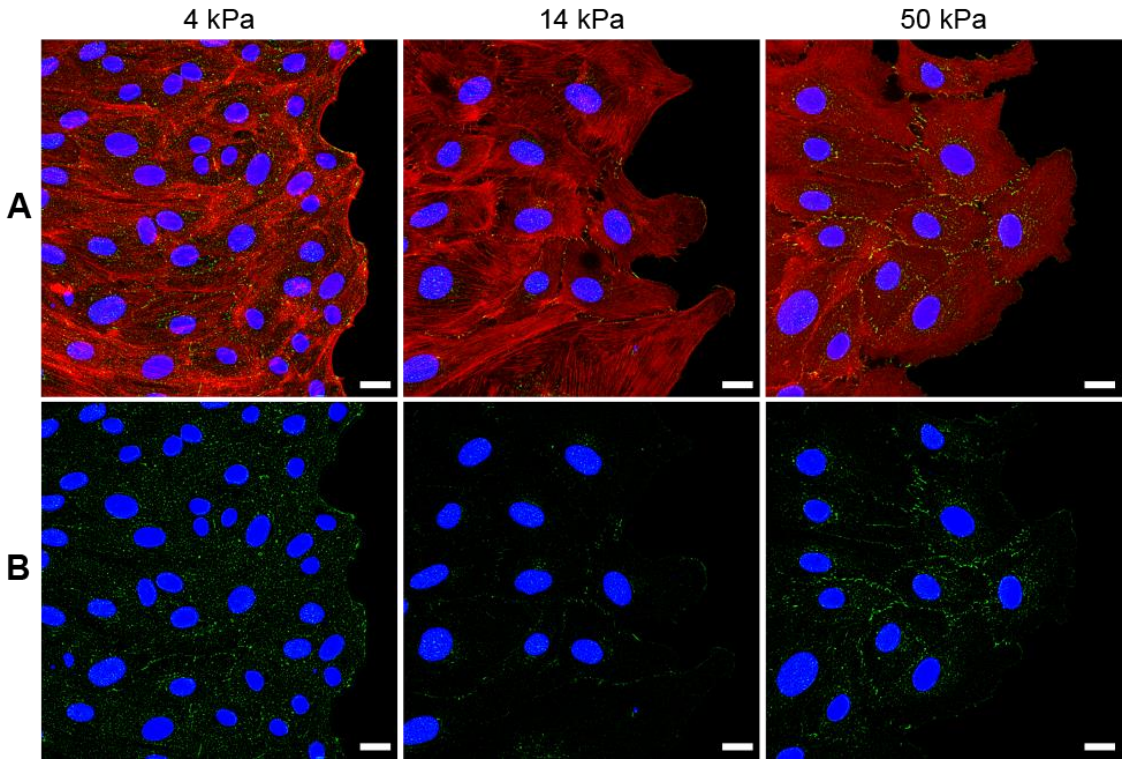

Figure 3.22: PAEC have diffuse VE-cadherin with no gaps on 4 kPa substrates and focal VE-cadherin between gaps on 14 kPa and 50 kPa substrates. (A) Representative confocal microscopy images. After 24 hours in the cage migration assay, samples were fixed and labeled for VE-cadherin (green), F-actin (red), and nuclei (blue). (B) Confocal microscopy images of VE-cadherin alone. Scale bars = 20 µm.

We further investigated togetherness by examining β-catenin localization. β-catenin is largely sequestered at the cell membrane in cadherin complexes. When the adherens junctions are disassembled, β-catenin dissociates from VE-cadherin and translocates into the nucleus. Therefore, the relative levels of nuclear and non-nuclear β-catenin were used as markers for togetherness (Figure 3.23). The ratio of nuclear:non-nuclear β-catenin remained constant on 4 kPa gels from 12 to 36 hours (Figure 3.24). However, the nuclear:non-nuclear β-catenin ratio was 48-70% higher on 14 and 50 kPa substrates at 12 hours within 100-500 μm of the interface ($F = 32.87$, $p < 0.0001$). After 24 hours, however, there was no difference in nuclear:non-nuclear β-catenin ratio among substrates ($F = 3.065$, $p > 0.05$). These data suggest that togetherness is a dynamic, transient process in collective migration that is dependent on substrate stiffness. In particular, we found that togetherness decreases at 12 hours on 14 kPa and 50 kPa substrates compared to 4 kPa substrates.

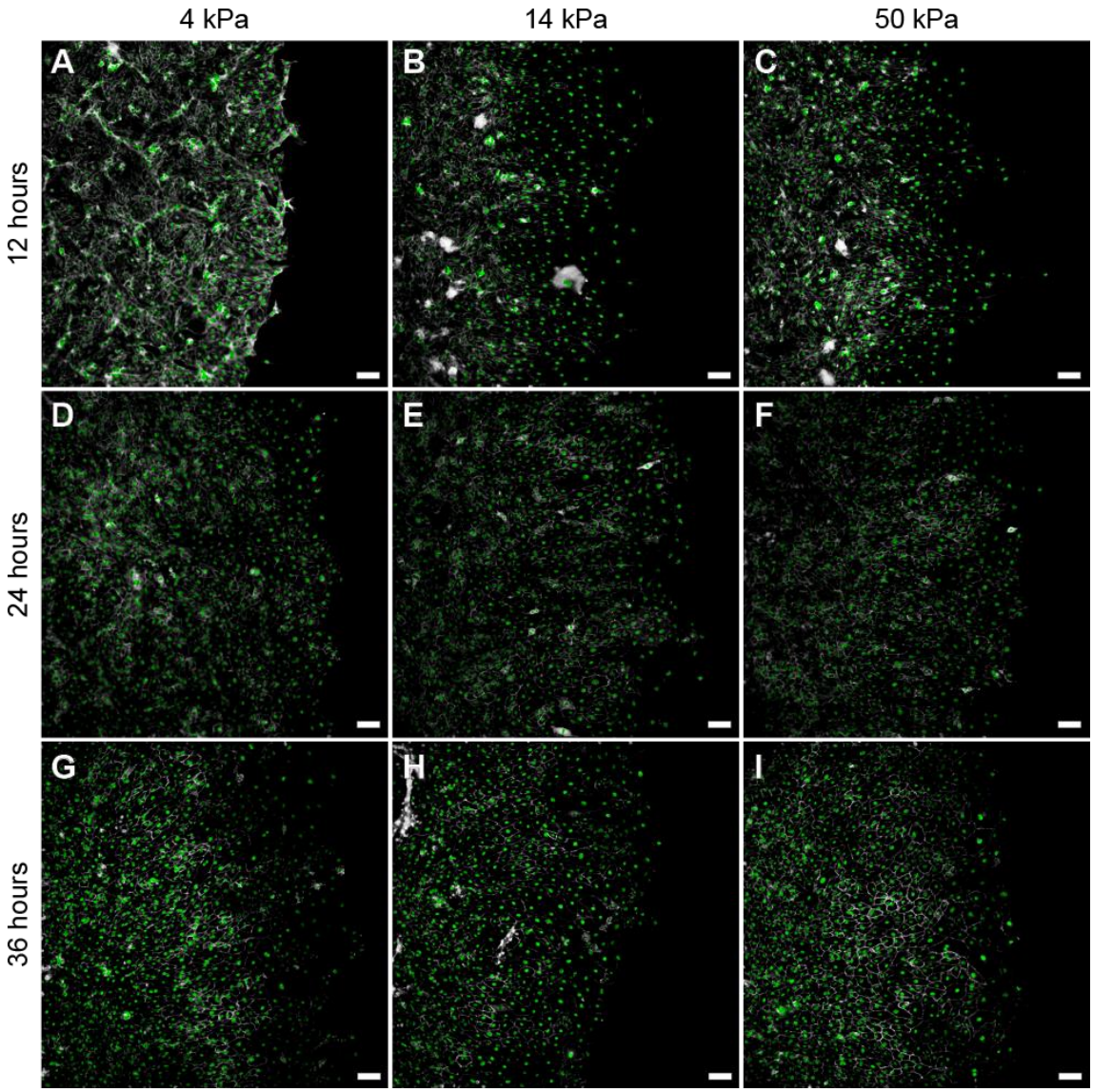

Figure 3.23: The nuclear:non-nuclear β-catenin ratio increased with substrate stiffness, peaking at 12 hours. (A-I) PAEC were fixed and labeled for β-catenin. A custom MATLAB algorithm filtered and separated the β-catenin channel into nuclear (green) and non-nuclear (white) regions. Scale bars = 100 µm.

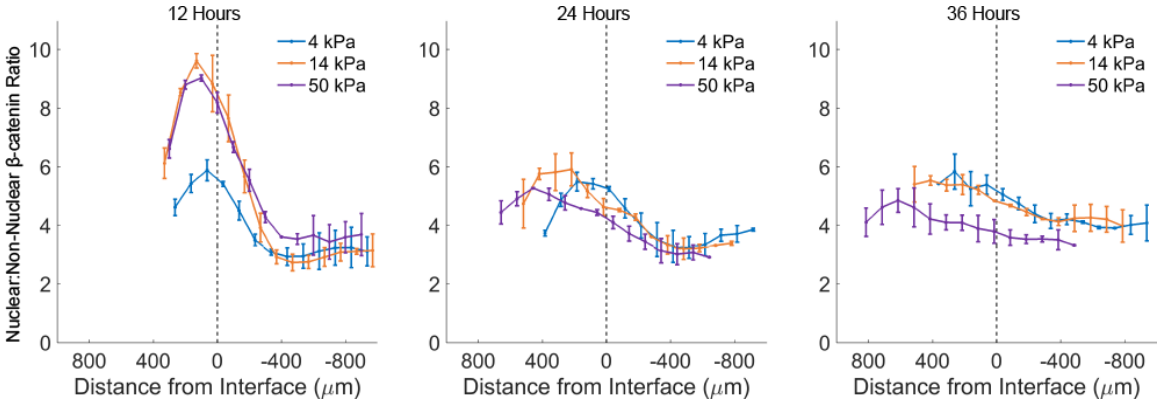

Figure 3.24: The nuclear:non-nuclear β-catenin ratio increased with substrate stiffness, peaking at 12 hours at 100-500 µm from the interface and decreasing through 36 hours in the cage migration assay.

3.3.6. Proliferation as a Function of Substrate Stiffness

In order to investigate whether cell proliferation may contribute to differences in migration distance, a BrdU proliferation assay was performed. PAEC proliferated more on 14 and 50 kPa as compared to 4 kPa gels (Figure 3.25). For bands within 200 µm of the interface, there was a 36% and 34% increase in proliferating cells for 14 and 50 kPa substrates, respectively, compared to 4 kPa substrates (Figure 3.25D). These differences dropped gradually farther from the interface to 21% and 27% increase at 200-400 µm and then to 13% and 11% increase at 400-600 µm for 14 and 50 kPa gels, respectively. These results suggest that proliferation is dependent on substrate stiffness within the collectively migrating front. It also may be an indication that cell-cell adhesion diminishes on stiffer substrates compared to soft ones.

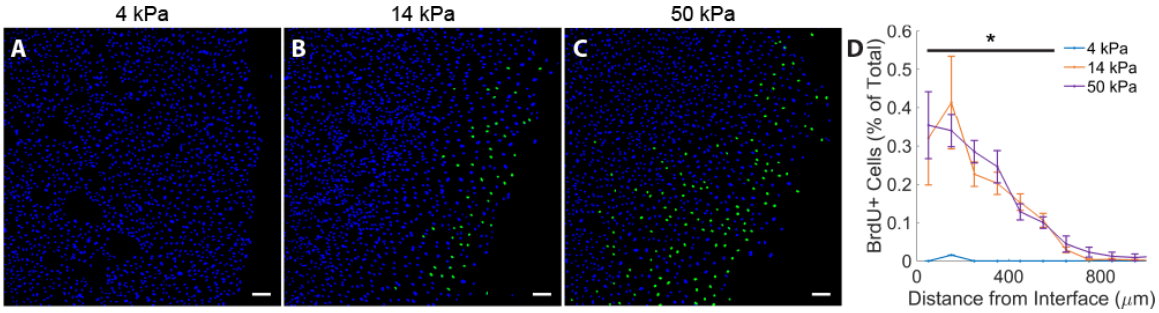

Figure 3.25: PAEC proliferation increased in the migratory front on stiffer substrates after 24 hours. (A-C) BrdU (green) was added to cells in the final 1 hour of the 24-hour migration time. Cells were also labeled for nuclei (blue). (D) Percent of BrdU+ nuclei vs. distance from interface. Scale bars = 100 μm. *$p < 0.01$, comparisons between 14 and 50 kPa vs. 4 kPa.

3.3.7. ROCK Inhibition to Attenuate Cell Contractility

We demonstrated that endothelial cell migration distance increases with substrate stiffness. Rho/ROCK-mediated contractility has been shown to be important for rear tail retraction for cell motility.[130] To determine if this pathway is important in stiffness-dependent collective migration, ROCK was inhibited with Y27632 for 30 minutes at 0, 12, or 18 hours. This treatment caused a marked increase in long, thin filopodia (Figure 3.26A,B). While control samples showed MLC phosphorylation after 24 hours (Figure 3.26C,F), Y27632 prevented MLC activation through 24 hours for all time points: 0-0.5 hours (Figure 3.26D,G), 12-12.5 hours (Figure 3.26E,H), and 18-18.5 hours (data not shown).

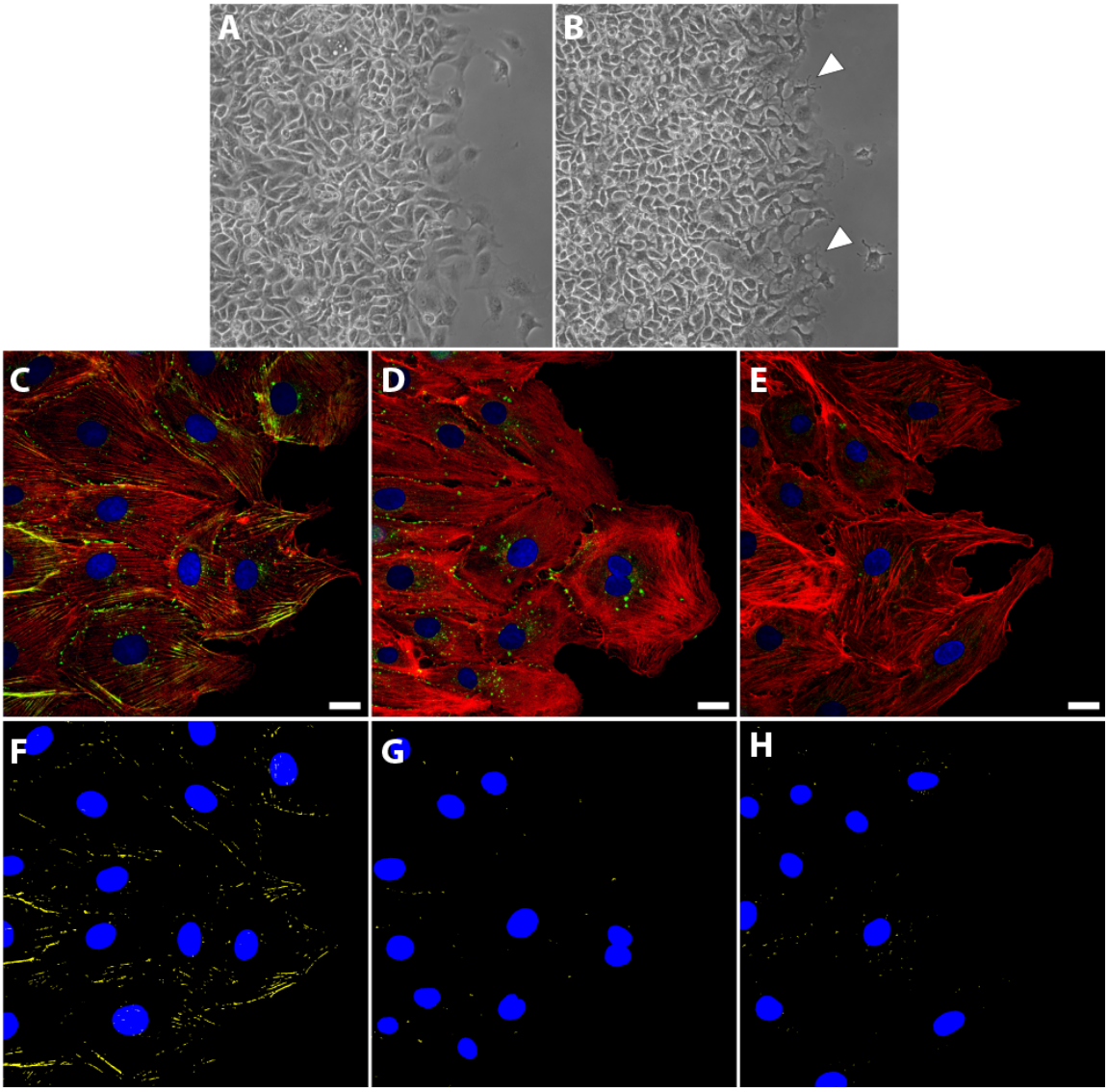

Figure 3.26: 30 minutes Y27632 reduced MLC activation throughout 24 hours. Phase contrast images of PAEC (A) controls or (B) 30 minutes 10 µM Y27632. White arrow heads show long and thin filopodia. (C) Confocal microscopy images of samples labeled for phosphorylated MLC (green), F-actin (red), and nuclei (blue). (F) MATLAB-processed images showing co-localized phosphorylated MLC with F-actin (yellow). (D,G) 10 µM Y27632 given from 0-0.5 hours. (E,H) 10 µM Y27632 given from 12-12.5 hours. Scale bar = 20 µm.

3.3.8. Effect of ROCK Inhibition on Collective Migration Distance

To determine if ROCK is important in stiffness-dependent collective migration, PAEC were treated with 10 µM Y27632 for 30 minutes at 0, 12, or 18 hours and average migration distance was measured (Figure 3.27). Interestingly, ROCK inhibition did not affect migration distance for

cells on 50 kPa gels. Instead, ROCK inhibition increased migration distance in cells on both 4 and 14 kPa gels by 52% and 38%, respectively. Y27632 timing did not significantly affect migration distance on any substrate. These results suggest that ROCK-mediated contractility limits migration speed in a substrate stiffness-dependent fashion, namely on 4 kPa and 14 kPa substrates, but not 50 kPa substrates.

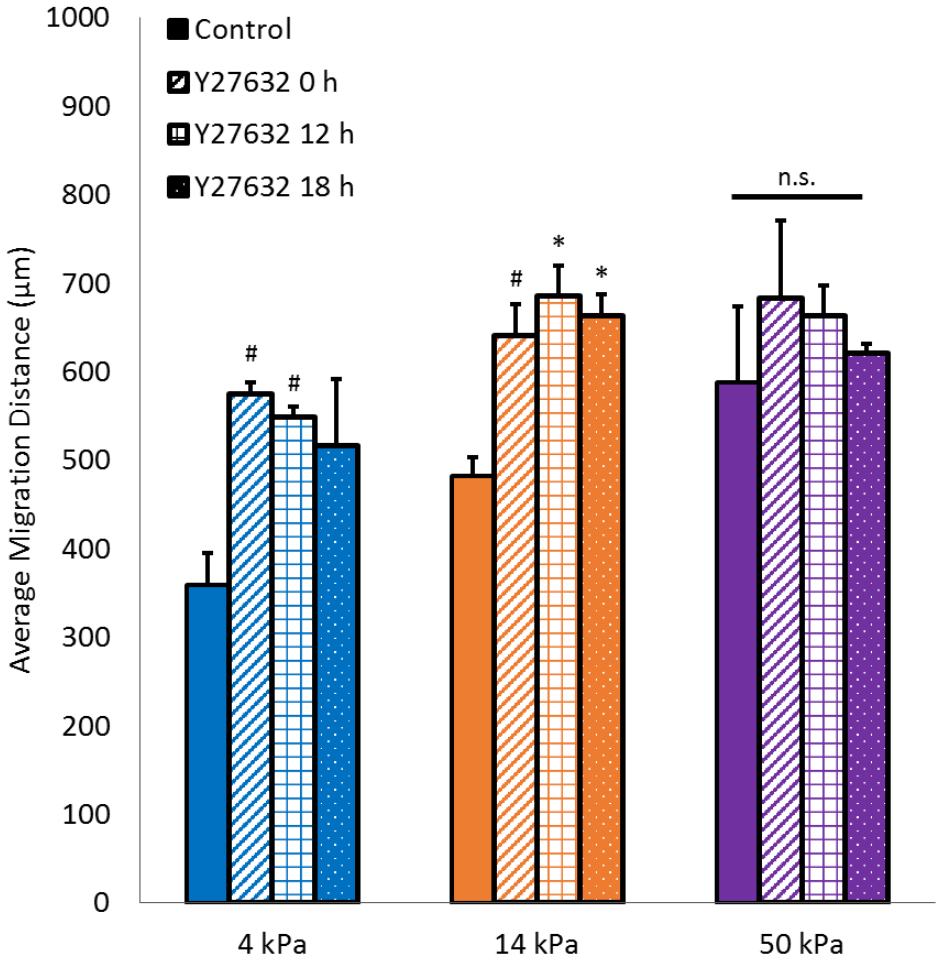

Figure 3.27: ROCK inhibition increased migration distance for cells on 4 and 14 kPa gels, but not for cells on 50 kPa gels. 10 µM Y27632 was added to cell medium for 30 minutes at 0, 12, and 18 hours. PAEC were allowed to migrate until 24 hours when they were fixed and labeled for F-actin and nuclei. #$p < 0.05$; *$p < 0.01$; n.s. = not significant as compared to control samples on the same stiffness substrate.

3.3.9. Effect of ROCK Inhibition on Cellular Orientation

To determine if ROCK inhibition affected directedness, nuclear orientation was measured as a function of distance from the migratory front (Figure 3.28-3.31). Compared to controls (Figure 3.6), ROCK inhibition abrogated the alignment difference observed with substrate stiffness, regardless of when it was added (Figure 3.31). PAEC on 4 and 50 kPa gels showed the same degree of peak alignment as cells on 14 kPa gels. In addition, PAEC peak alignment consistently occurred 600 μm back from the interface. When different substrate stiffness samples were adjusted for change in total migration direction, alignment curves were statistically similar for samples exposed to Y27632 regardless of substrate stiffness ($F = 2.72$, $F = 1.93$, and $F = 3.38$, respectively, $p > 0.05$). These results suggest that ROCK inhibits PAEC alignment with the migration direction on softer substrates.

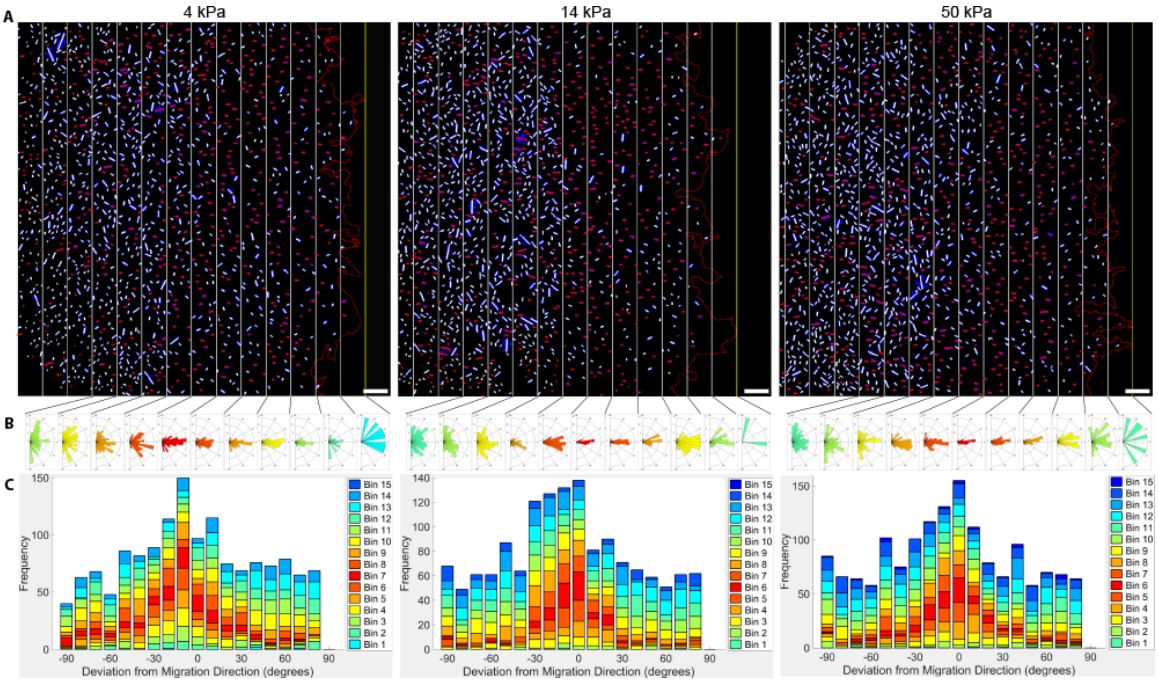

Figure 3.28: Differences in cell alignment between substrate stiffness were abolished by 24 hours when 10 µM Y27632 was given for 30 minutes at 0 hours. (A) Nuclei (blue) with short lines (red = within 20° of the global migration direction, white = greater than 20° from the global migration direction) indicating their long axis angle. The global migration direction is perpendicular to the bin lines. (B) Nuclear angle frequency rose plots for each bin. 0° (to the right) represent nuclei with no deviation from the global migration direction. Values ranged from [-90°,90°]. The rose plot for the bin with the highest percentage of aligned nuclei is red. (C) Stacked histograms with a similar color scheme as described in (B). Scale bars and distance between bin lines = 100 µm.

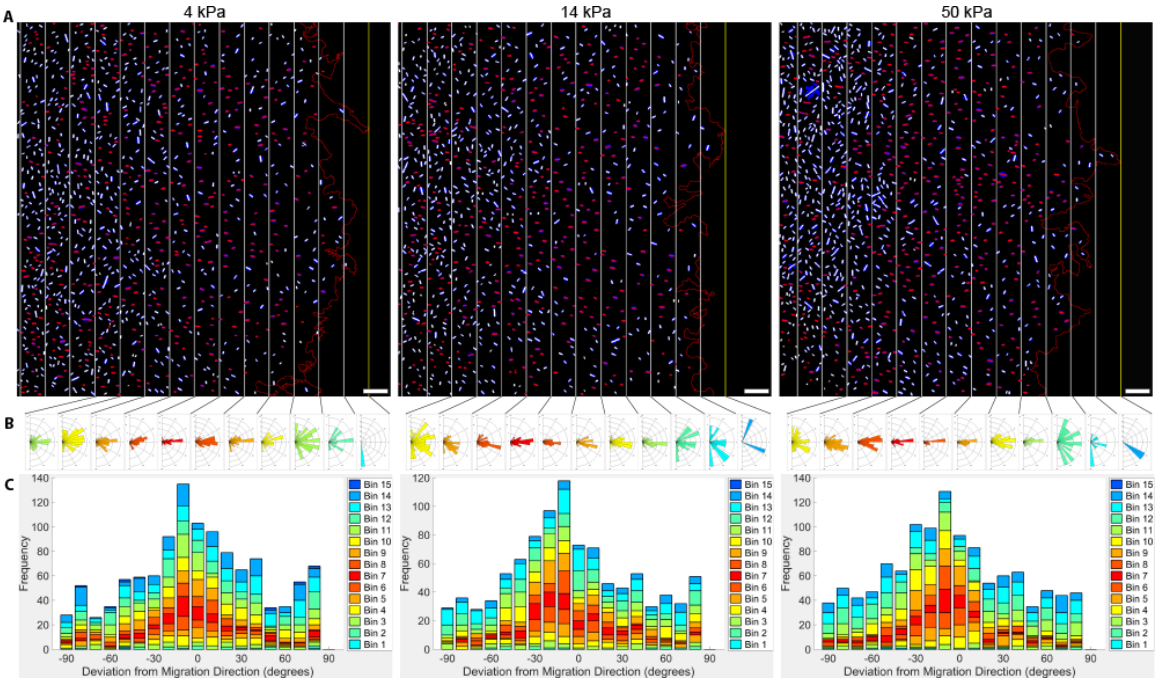

Figure 3.29: Differences in cell alignment between substrate stiffness were abolished by 24 hours when 10 µM Y27632 was given for 30 minutes at 12 hours. (A) Nuclei (blue) with short lines (red = within 20° of the global migration direction, white = greater than 20° from the global migration direction) indicating their long axis angle. The global migration direction is perpendicular to the bin lines. (B) Nuclear angle frequency rose plots for each bin. 0° (to the right) represent nuclei with no deviation from the global migration direction. Values ranged from [-90°,90°]. The rose plot for the bin with the highest percentage of aligned nuclei is red. (C) Stacked histograms with a similar color scheme as described in (B). Scale bars and distance between bin lines = 100 µm.

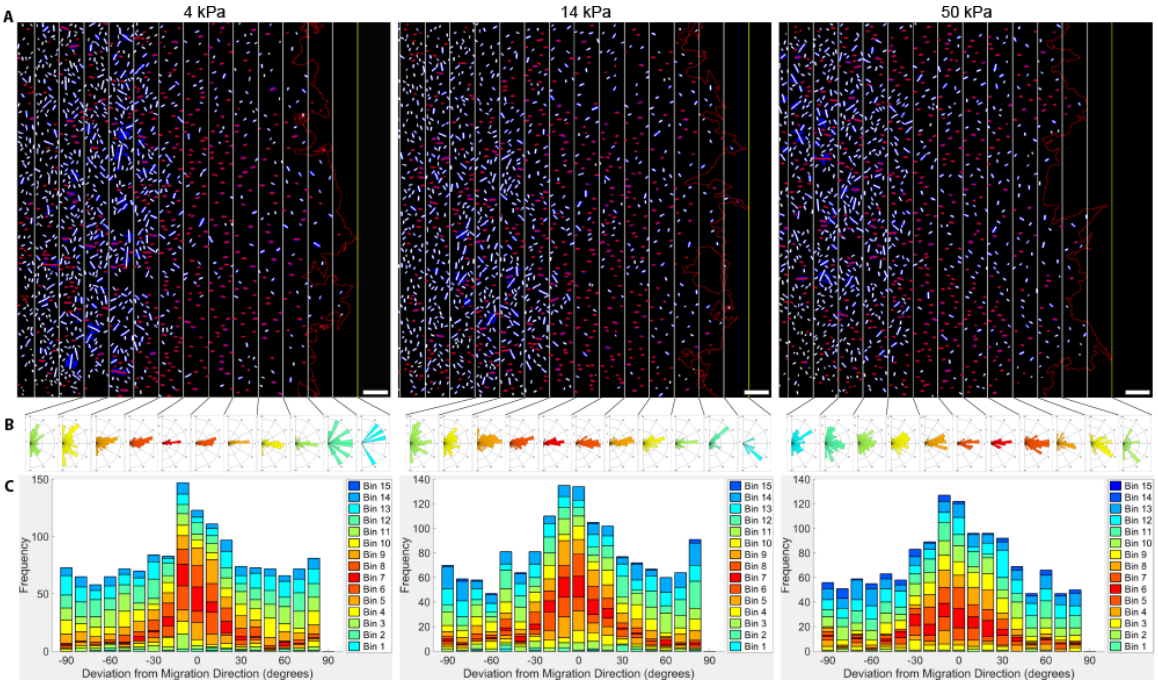

Figure 3.30: Differences in cell alignment between substrate stiffness were abolished by 24 hours when 10 µM Y27632 was given for 30 minutes at 18 hours. (A) Nuclei (blue) with short lines (red = within 20° of the global migration direction, white = greater than 20° from the global migration direction) indicating their long axis angle. The global migration direction is perpendicular to the bin lines. (B) Nuclear angle frequency rose plots for each bin. 0° (to the right) represent nuclei with no deviation from the global migration direction. Values ranged from [-90°,90°]. The rose plot for the bin with the highest percentage of aligned nuclei is red. (C) Stacked histograms with a similar color scheme as described in (B). Scale bars and distance between bin lines = 100 µm.

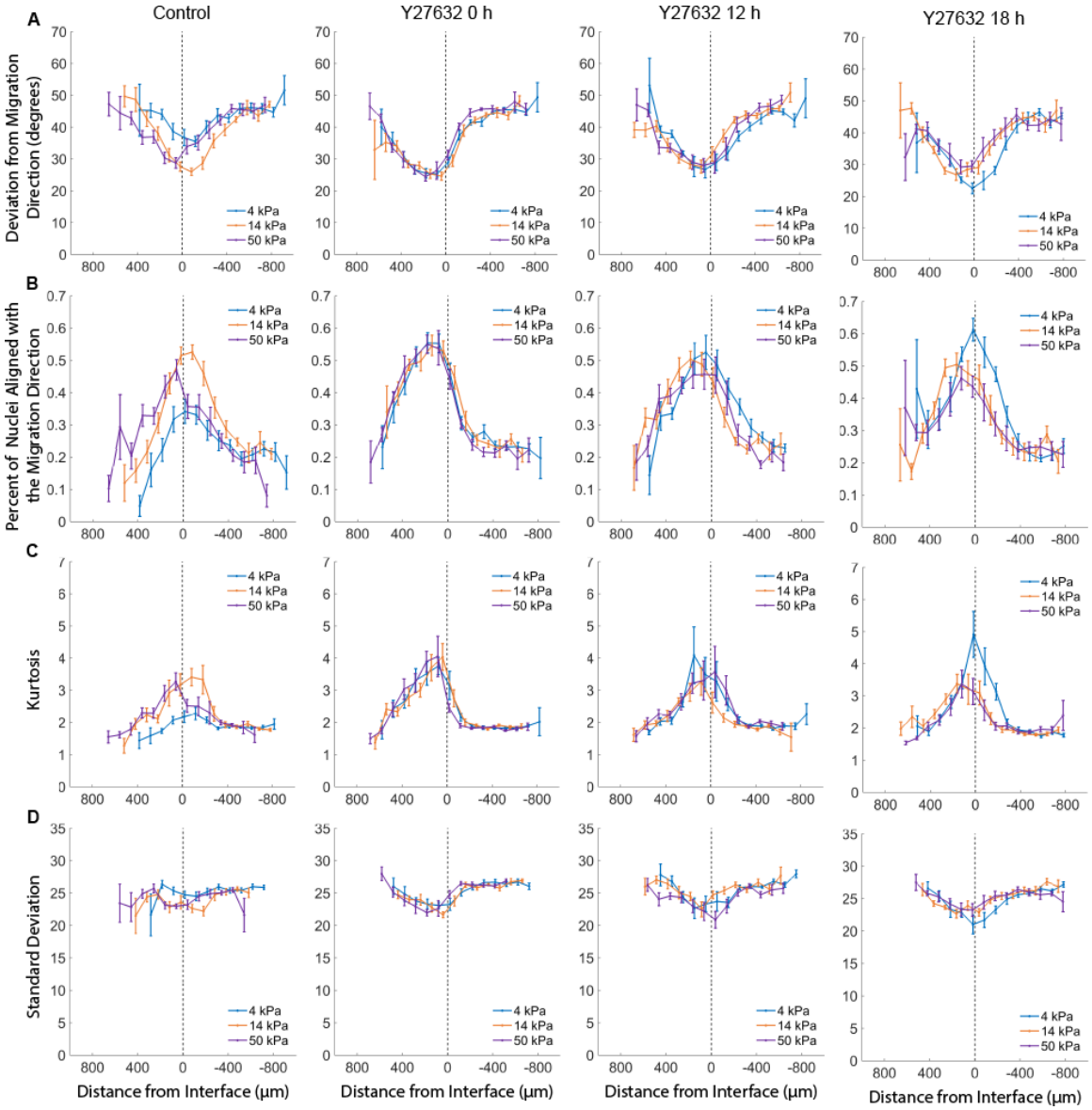

Figure 3.31: Substrate stiffness-induced differences in cells aligned with the migration direction was abolished by 24 hours when a ROCK inhibitor was given for 30 minutes at 0, 12, or 18 hours. Four metrics were used to compare differences in nuclear alignment relative to the migration direction: (A) average angle deviation from the migration direction, (B) percent of nuclei aligned with the migration direction, (C) kurtosis of nuclear angle distribution, and (D) standard deviation of nuclear angle distribution. Along the x-axis, 0 is the original cage position and cells migrate in the positive direction.

3.3.10. Effect of ROCK Inhibition on Fibronectin Fiber Orientation and Length

To determine if ROCK inhibition affects PAEC fibronectin organization, 10 μM Y27632 was added at the 12 hour time point of a 24-hour cage migration assay. This time point was chosen

because it preceded the appearance of fibronectin fibers aligned with the migration direction (24 hours, Fig 3.16). ROCK inhibition had no significant effect on fibronectin fiber alignment on any substrate in the interface and migratory zones (Figure 3.32-3.34). However, the percentage of long fibers (longer than 2.3 μm) was lower on 50 kPa, but not 4 or 14 kPa gels (Figure 3.35). This suggests that ROCK-mediated contractility is required for PAEC on stiff substrates to generate enough tension to elongate fibronectin fibers.

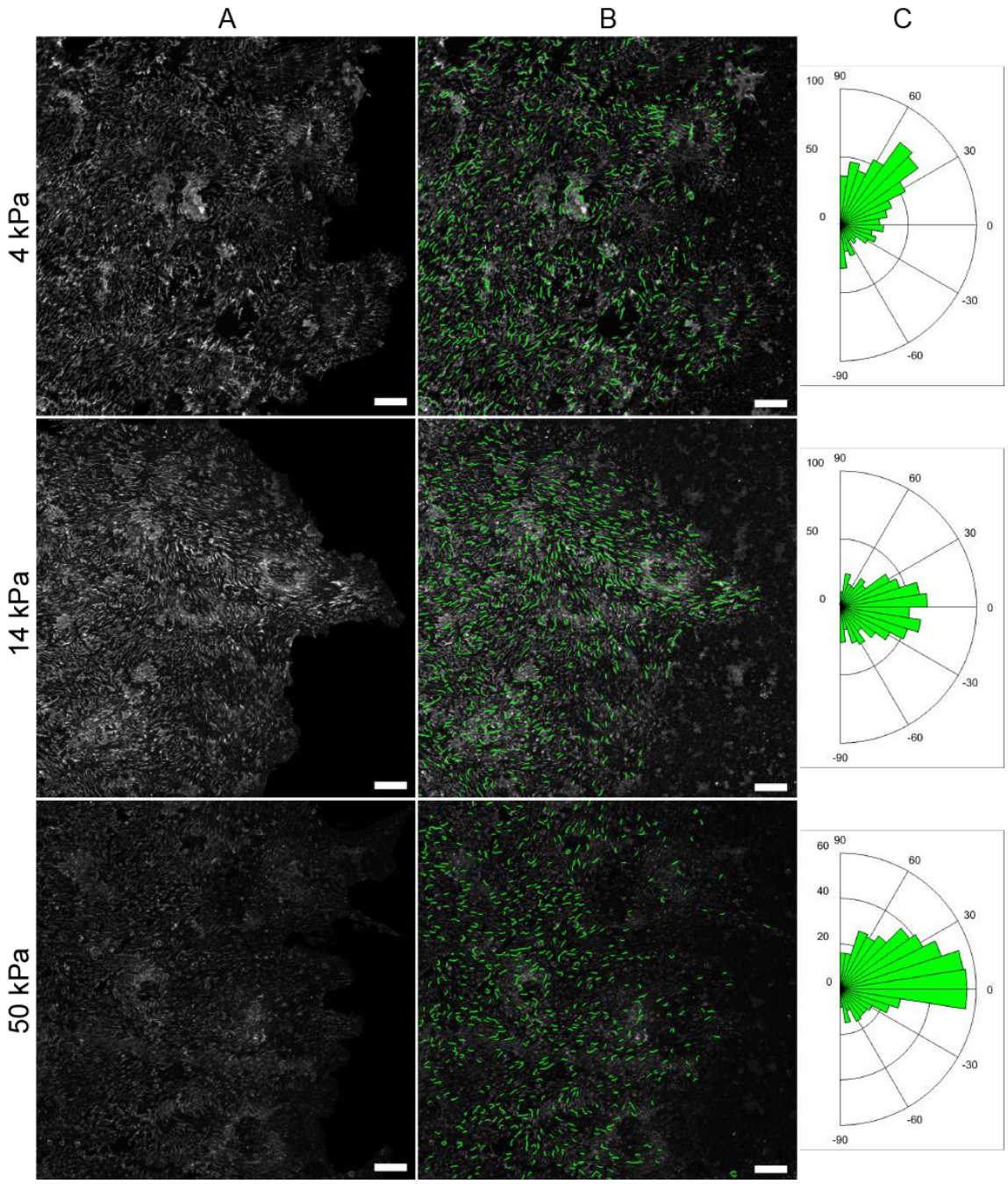

Figure 3.32: Fibronectin fiber alignment did not differ with substrate stiffness in the interface zone at 24 hours when ROCK was inhibited with 10 µM Y27632 for 30 minutes at 12 hours. (A) Confocal microscopy images of fibronectin fibers. (B) MATLAB output showing identified fibers (green) overlaying the original image. (C) Fiber angle distribution. Scale bars = 20 µm.

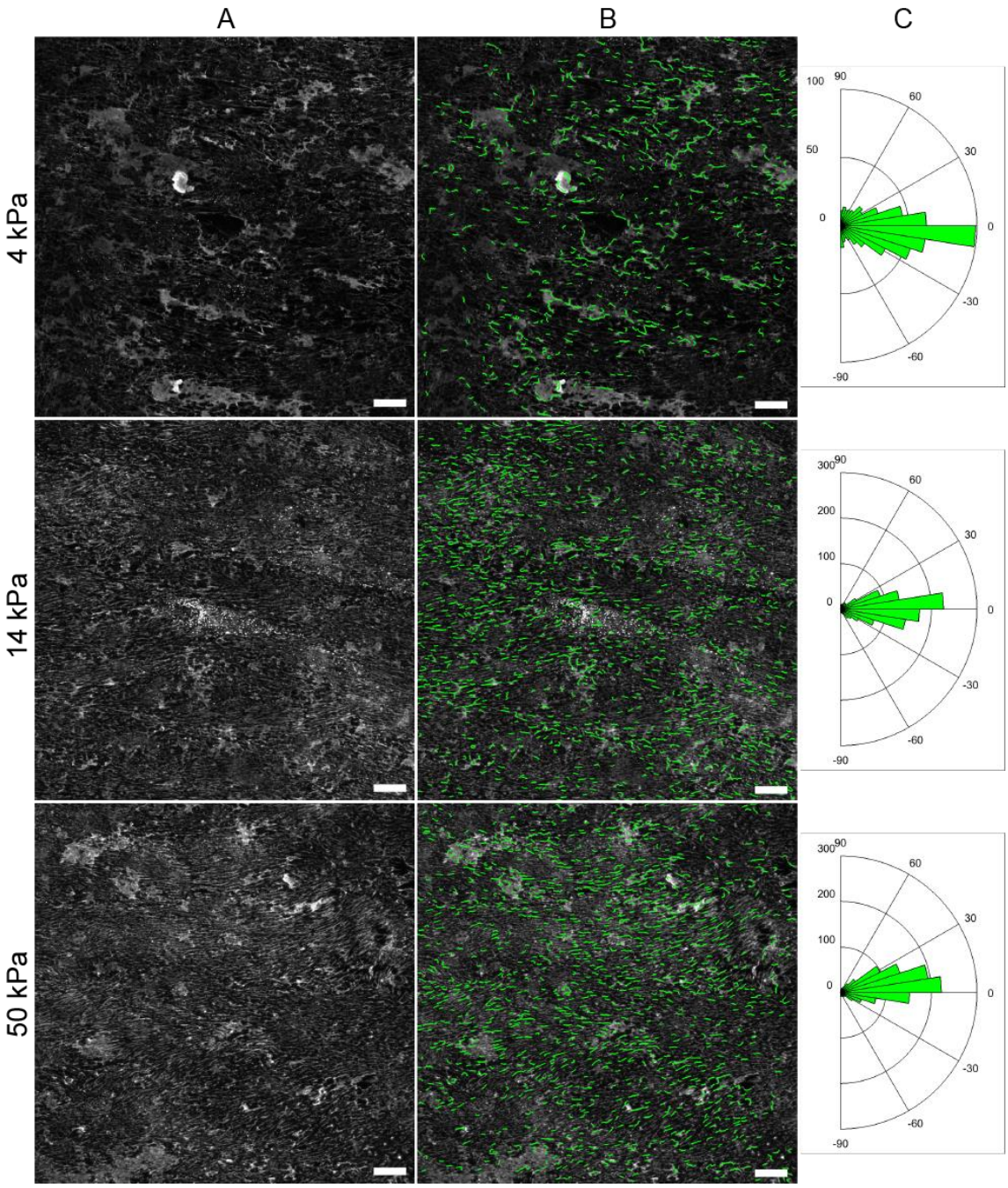

Figure 3.33: Fibronectin fiber alignment did not differ with substrate stiffness in the migratory zone at 24 hours when ROCK was inhibited with 10 µM Y27632 for 30 minutes at 12 hours. (A) Confocal microscopy images of fibronectin fibers. (B) MATLAB output showing identified fibers (green) overlaying the original image. (C) Fiber angle distribution. Scale bars = 20 µm.

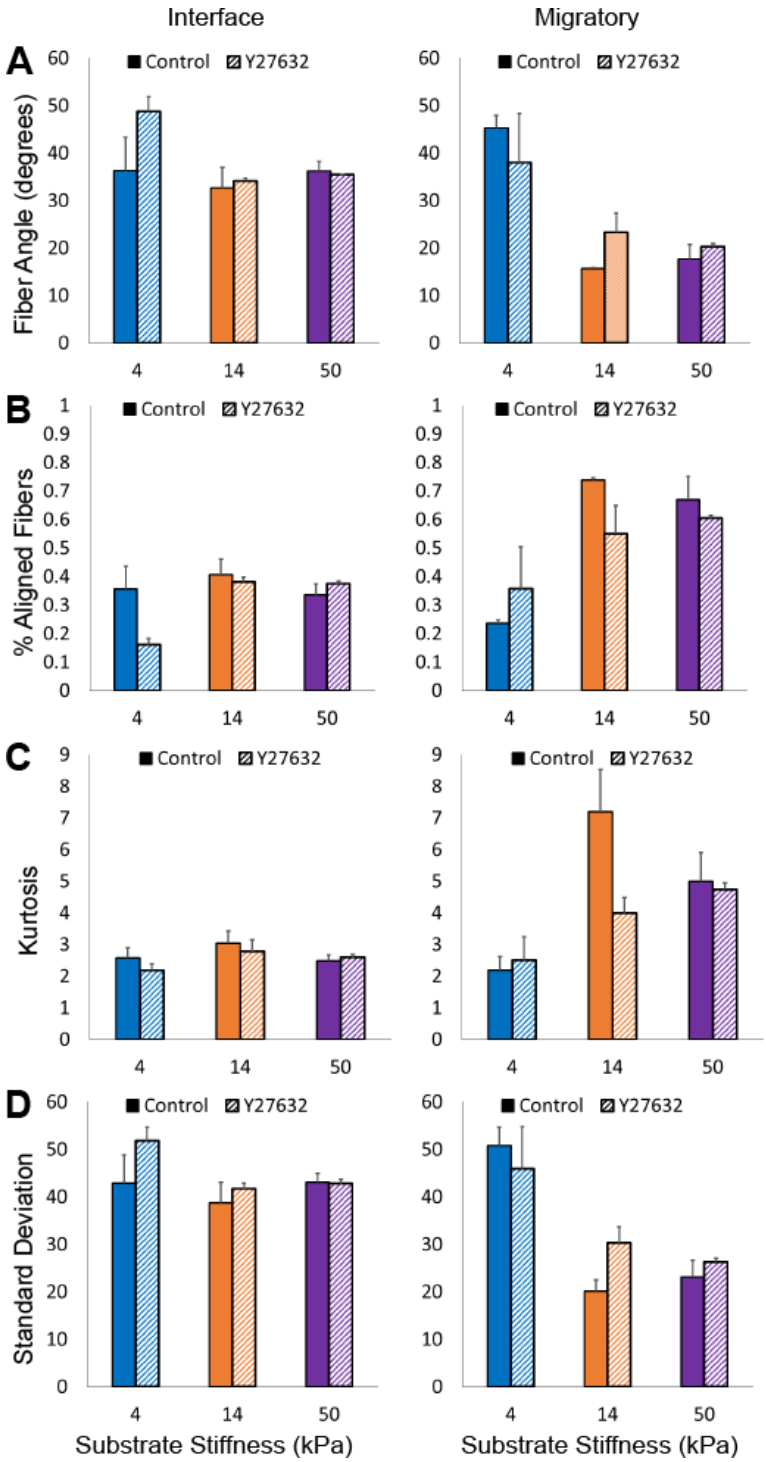

Figure 3.34: Fibronectin fiber alignment did not differ with substrate stiffness in the interface or migratory zone at 24 hours when ROCK was inhibited with 10 µM Y27632 for 30 minutes at 12 hours. (A) Average fiber angle, (B) percent of fibers aligned within 20° of the migration direction, (C) kurtosis of the fiber angle distribution, and (D) standard deviation of the fiber angle distribution for each zones on 4, 14, and 50 kPa gels.

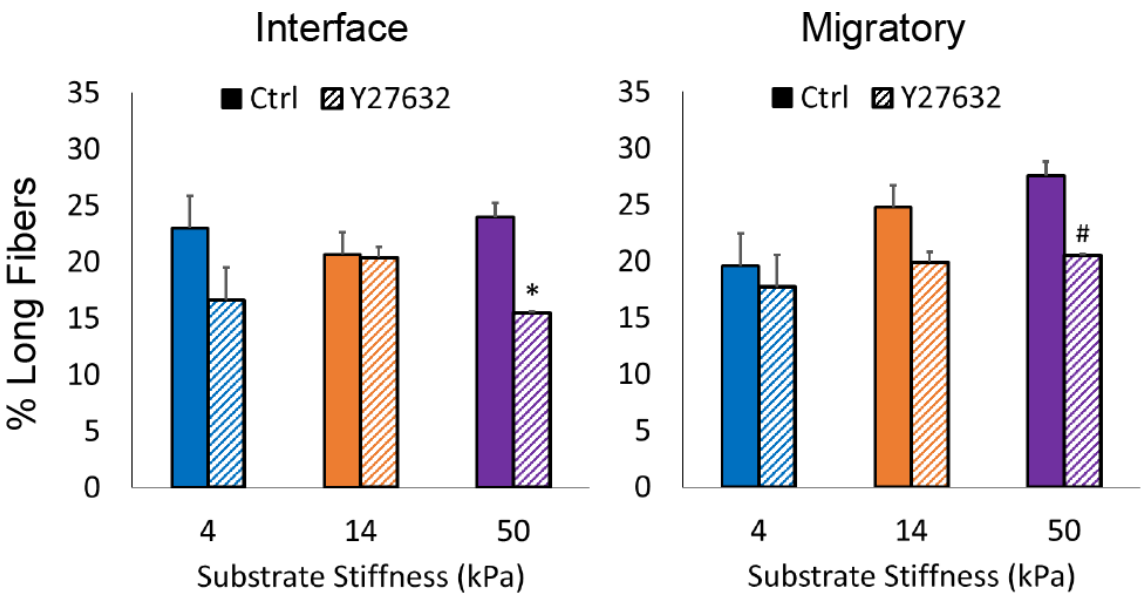

Figure 3.35: Long fibronectin fiber number decreased on 50 kPa, but not on 4 or 14 kPa gels, in response to ROCK inhibition. PAEC were given 10 μM Y27632 for 30 minutes at 12 hours and fixed at 24 hours. Fibronectin fiber length was determined by a custom MATLAB algorithm and the percentage of long fibers, i.e. fibers above 2.3 μm, was measured. #$p < 0.05$; *$p < 0.01$ compared to the untreated control on the same substrate stiffness.

3.3.11. Effect of Fibronectin and α_5 Integrin siRNA Knockdowns on Collective Migration Distance

To further investigate whether fibronectin is essential for mediating stiffness effects on collective migration, fibronectin and α_5 integrin were knocked down using siRNA. $\alpha_5\beta_1$ and $\alpha_V\beta_3$ integrins are the primary integrins that bind to fibronectin.[131, 132] We chose to knock down the α_5 integrin because $\alpha_5\beta_1$ has been shown to be more important for developing stable focal adhesions than the $\alpha_V\beta_3$ integrin. Knockdown efficacy was verified by Western blot (Figure 3.3).

24 hour migration distance was measured in fibronectin or α_5 integrin knockdown PAEC (Figure 3.36). Cells transfected with scrambled siRNA showed increased migration distance with substrate stiffness ($F = 20.64$, $p = 0.003$), as expected. Fibronectin knockdown did not affect migration distance on any substrate (Figure 3.36), but it did abrogate differences among substrate

stiffnesses ($F = 0.73$, $p = 0.51$). However, α_5 integrin knockdown decreased migration distance by 22% and 29% on 14 and 50 kPa gels, respectively, and also abrogated differences among substrate stiffnesses ($F = 0.22$, $p = 0.80$). These results suggest that α_5 integrin, but not fibronectin, is important for mechanotransducing substrate stiffness in collective migration by allowing PAEC to migrate faster on stiffer substrates.

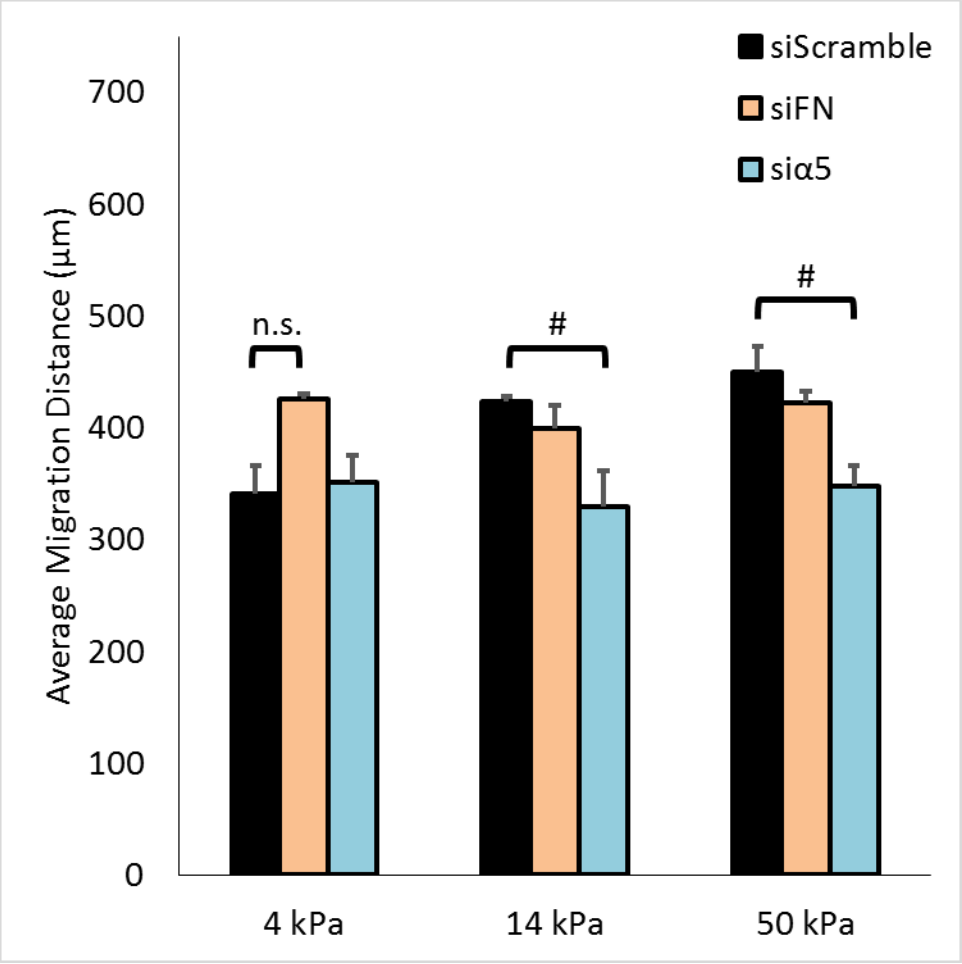

Figure 3.36: Migration distance was impaired in α_5 integrin knockdown PAEC on 14 and 50 kPa gels, but not 4 kPa gels. Fibronectin or α_5 integrin was knocked down in PAEC, which were subsequently measured for migration distance in a 24-hour cage migration assay. #$p < 0.05$; n.s. = not significant ($p > 0.05$).

3.3.12. Effect of Fibronectin and α_5 Integrin siRNA Knockdowns on Cellular Orientation

To determine if fibronectin and/or α_5 integrin are essential for cell alignment within the migratory front, nuclear alignment was measured at 24 hours in fibronectin or α_5 integrin knockdown PAEC (Figure 3.37-3.39). In the absence of fibronectin, the peak in average nuclear angle (Figure 3.40A) and percent of nuclei aligned with the migration direction (Fib. 3.40B) decreased 25% only on 4 kPa substrates at 400-500 μm ($p < 0.05$), but showed no difference from control on 14 kPa and 50 kPa substrates. These data indicate that fibronectin knockdown leads to fewer cells aligned with the migration direction (on softer gels) and high alignment variability in the migratory front (on all gels). This suggests that fibronectin may be a more important cue for cell alignment in the migration direction on softer substrates than on stiff substrates.

When α_5 integrin was knocked down, however, alignment within the migratory front was abolished, resulting in a uniform nuclear angle distribution for each stiffness (Figure 3.37-3.39). On 4 kPa substrates, nuclear alignment decreased by 32-57% from 100-700 μm from the migratory interface with the α_5 integrin knock down ($p < 0.01$). On 14 kPa substrates, nuclear alignment decreased by 32-54% from 300-700 μm from the migratory interface with the α_5 integrin knock down ($p < 0.01$). On 50 kPa substrates, nuclear alignment decreased by 35-44% from 300-700 μm from the migratory interface with the α_5 integrin knock down ($p < 0.05$). This severe reduction in nuclear alignment on all stiffnesses was similar to the alignment of control samples on 4 kPa substrates (Figure 3.6). This suggests that α_5 integrin, likely as part of the $\alpha_5\beta_1$ integrin, is essential to substrate stiffness-dependent cell alignment.

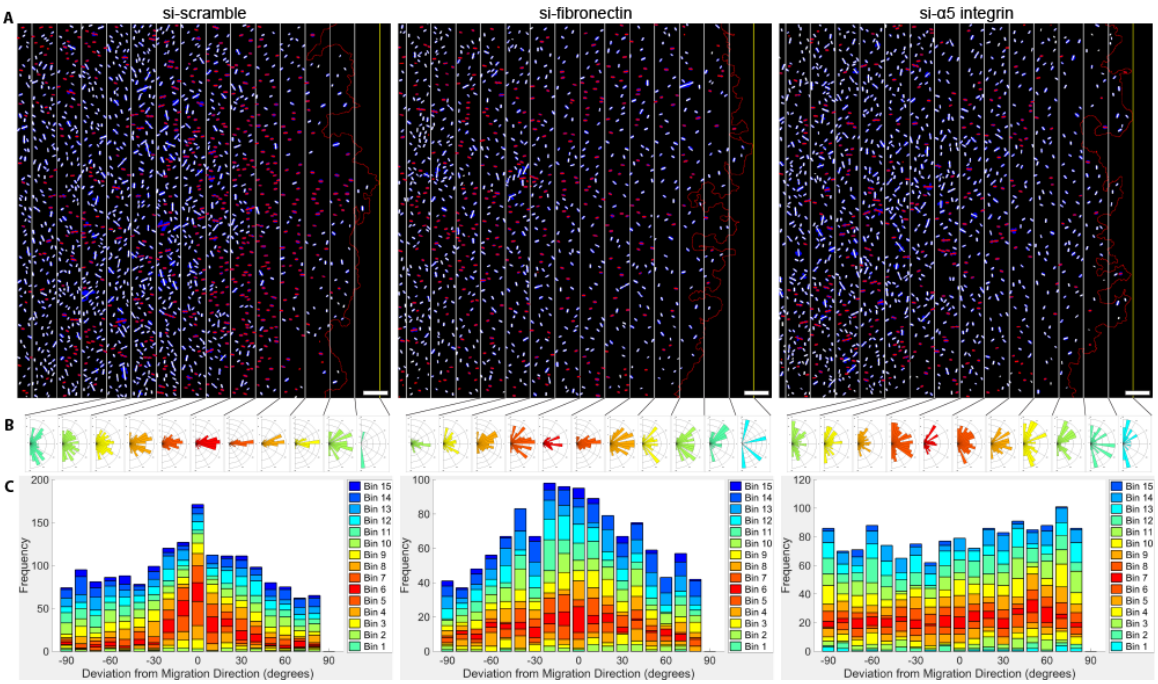

Figure 3.37: On 4 kPa gels, α_5 integrin knockdown abolished cell directedness and fibronectin knockdown decreased alignment in 400-500 µm zones. (A) Nuclei (blue) with short lines (red = within 20° of the global migration direction, white = greater than 20° from the global migration direction) indicating their long axis angle. The global migration direction is perpendicular to the bin lines. (B) Nuclear angle frequency rose plots for each bin. 0° (to the right) represent nuclei with no deviation from the global migration direction. Values ranged from [-90°,90°]. The rose plot for the bin with the highest percentage of aligned nuclei is red. (C) Stacked histograms with a similar color scheme as described in (B). Scale bars and distance between bin lines = 100 µm.

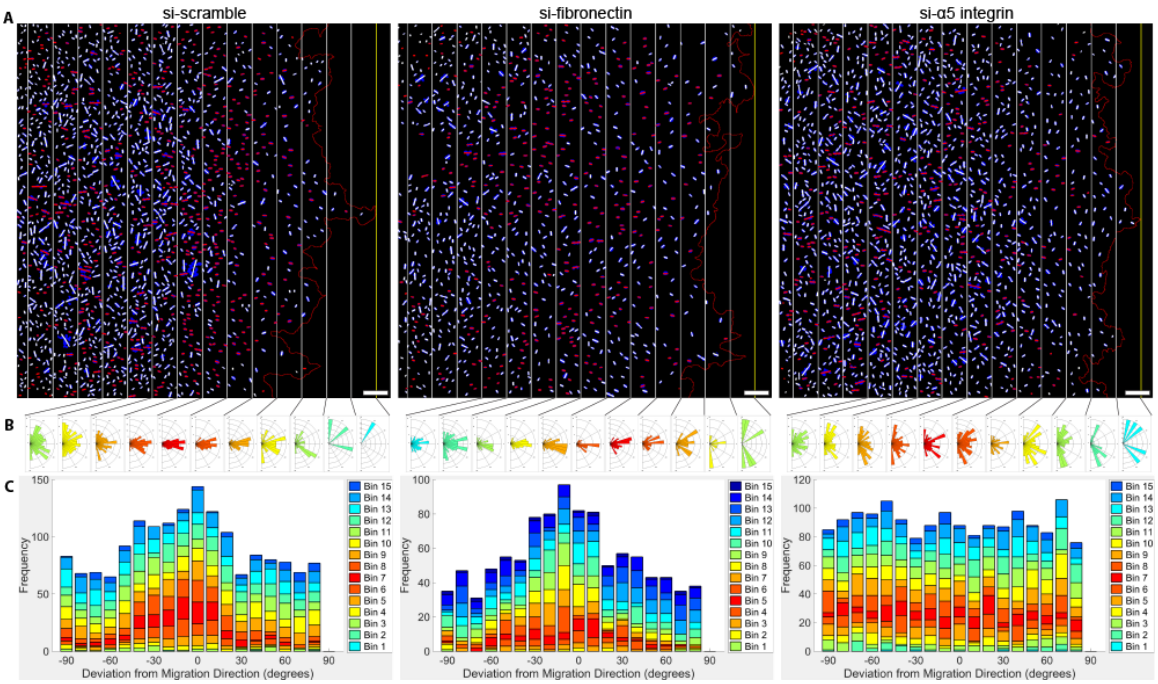

Figure 3.38: On 14 kPa gels, α_5 integrin knockdown abolished cell directedness while fibronectin knockdown had no effect. (A) Nuclei (blue) with short lines (red = within 20° of the global migration direction, white = greater than 20° from the global migration direction) indicating their long axis angle. The global migration direction is perpendicular to the bin lines. (B) Nuclear angle frequency rose plots for each bin. 0° (to the right) represent nuclei with no deviation from the global migration direction. Values ranged from [-90°,90°]. The rose plot for the bin with the highest percentage of aligned nuclei is red. (C) Stacked histograms with a similar color scheme as described in (B). Scale bars and distance between bin lines = 100 µm.

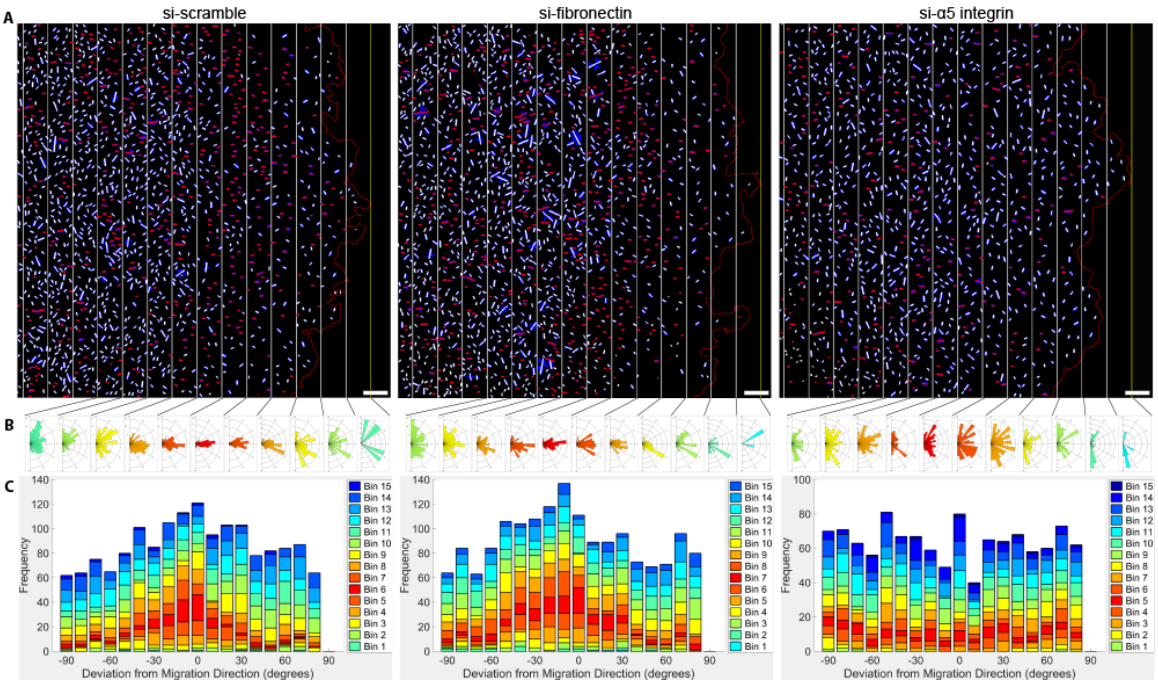

Figure 3.39: On 50 kPa gels, the α_5 integrin knockdown abolished cell directedness while fibronectin knockdown had no effect. (A) Nuclei (blue) with short lines (red = within 20° of the global migration direction, white = greater than 20° from the global migration direction) indicating their long axis angle. The global migration direction is perpendicular to the bin lines. (B) Nuclear angle frequency rose plots for each bin. 0° (to the right) represent nuclei with no deviation from the global migration direction. Values ranged from [-90°,90°]. The rose plot for the bin with the highest percentage of aligned nuclei is red. (C) Stacked histograms with a similar color scheme as described in (B). Scale bars and distance between bin lines = 100 µm.

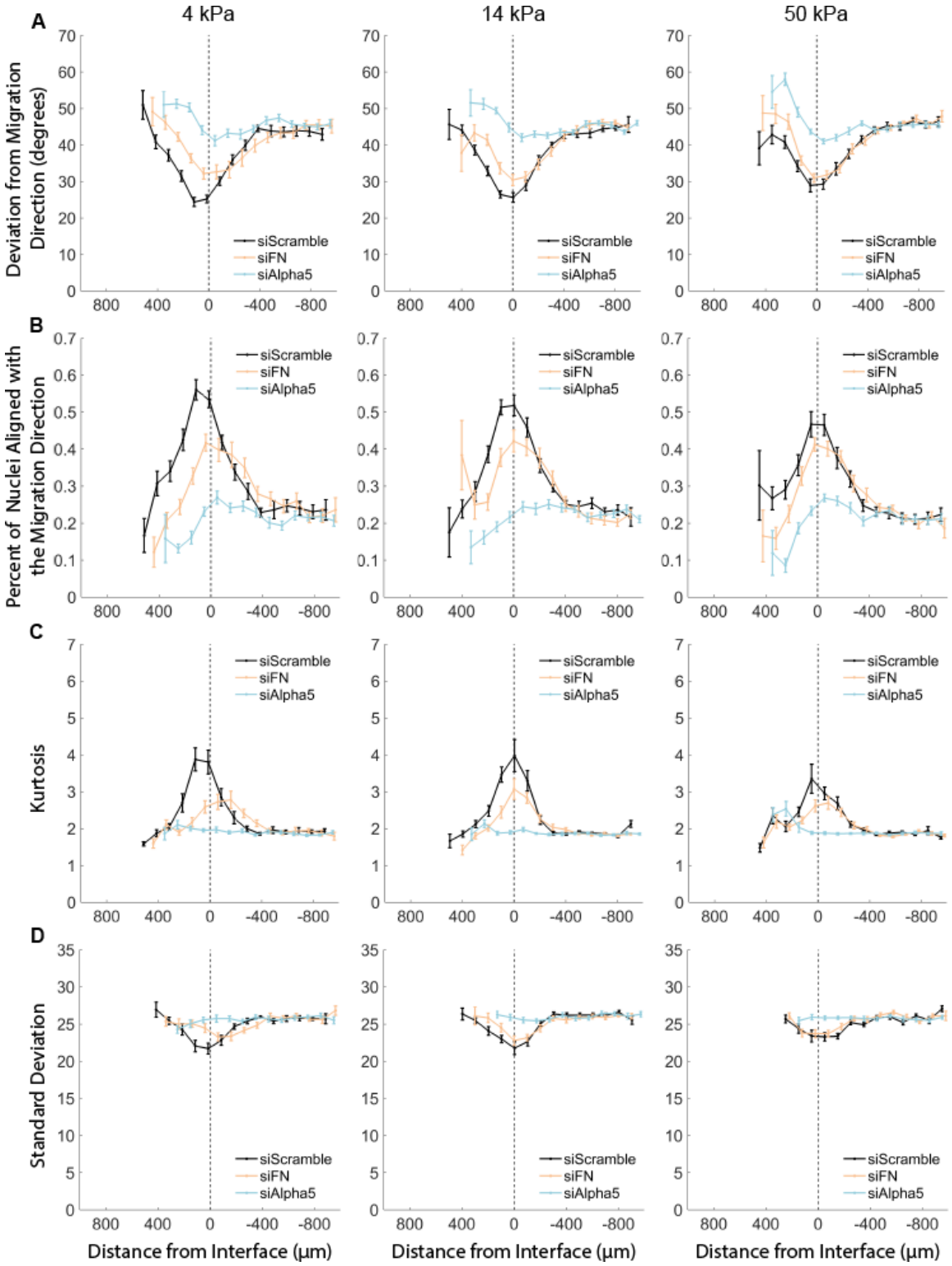

Figure 3.40: PAEC were less aligned with the migration direction with impaired α_5 integrin expression. Four metrics were used to compare differences in nuclear alignment relative to the migration direction: (A) average angle deviation from the migration direction, (B) percent of nuclei aligned with the migration direction, (C) kurtosis of nuclear angle distribution, and (D) standard deviation of nuclear angle distribution. Along the x-axis, 0 is the original cage position and cells migrate in the positive direction.

3.3.13. Effect of Fibronectin and α_5 Integrin siRNA Knockdowns on Cellular Elongation and Area

Cell morphology was measured as previously described in knockdown PAEC that migrated for 24 hours (Figure 3.41). There was no difference in aspect ratio among the transfection groups: si-scramble ($F = 7.12$, $p = 0.07$), si-fibronectin ($F = 4.36$, $p = 0.13$), and si-α_5 integrin ($F = 1.23$, $p = 0.41$) (Figure 3.39B). However, fibronectin and α_5 integrin knockdown significantly decreased cell aspect ratio on 4 and 14 kPa gels, but not 50 kPa gels. The negative control si-scramble PAEC on 14 and 50 kPa gels were larger than PAEC on soft substrates ($F = 80.60$, $p = 0.002$) (Figure 3.41C), as previously shown in Figure 3.11. This effect was lost in si-fibronectin ($F = 5.52$, $p = 0.10$) and si-α_5 integrin ($F = 2.32$, $p = 0.25$) samples. Interestingly, PAEC were larger with impaired fibronectin expression on 4 and 50 kPa gels, but not 14 kPa gels.

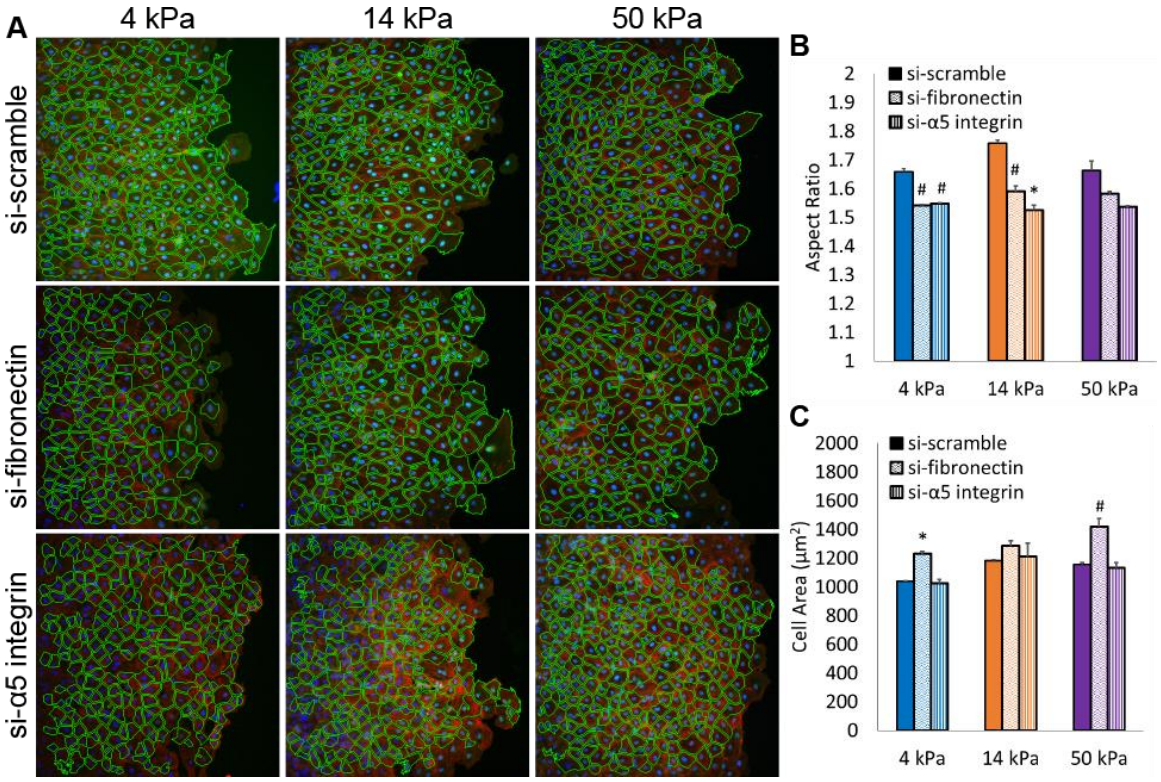

Figure 3.41: PAEC were less more elongated on 4 and 14 but not 50 kPa gels with fibronectin and α_5 integrin knockdown. In addition, cell area increased with fibronectin knockdown on 4 and 50 kPa gels but not 14 kPa gels. (A) Confocal microscopy images of cells fixed and labeled for β-catenin (green), F-actin (red), and nuclei (blue) after 24 hours migration. (B) Green boundaries delineate cell shapes from a custom MATLAB algorithm. Aspect ratio (C) and area (D) of the outlined cells. Scale bars = 50 μm. #$p < 0.05$; *$p < 0.01$; compared to si-scramble samples.

3.3.14. Effect of Fibronectin and α_5 Integrin siRNA Knockdowns on Fibronectin Fiber Angle and Length

Fibronectin fiber angle and length were analyzed in the interface and migratory zones of si-fibronectin and si-α_5 integrin PAEC on 4 and 50 kPa gels (Figure 3.42-3.43, 3.46-3.47). As expected, there were very few fibronectin fibers for the fibronectin knockdown samples. For the α_5 integrin knockdown, fibronectin fibers were present, but individual fiber angles were less aligned with the migration direction than the control. α_5 integrin knockdowns had an average fiber angle more than 1.5 and 2 times the control for 4 and 50 kPa gels, respectively (Figure 3.44). Interestingly, fibers on 50 kPa gels were less aligned than those on 4 kPa gels with α_5 integrin

knocked down. There were 15.2% fewer long fibers in the migratory zone on 4 kPa substrates when α_5 integrin was knocked down, but no differences under any other conditions. All of these trends at the interface were also observed at the migratory zone (Figure 3.46-3.49). These data suggest that α_5 integrin is necessary for aligning fibronectin fibers in the migration direction.

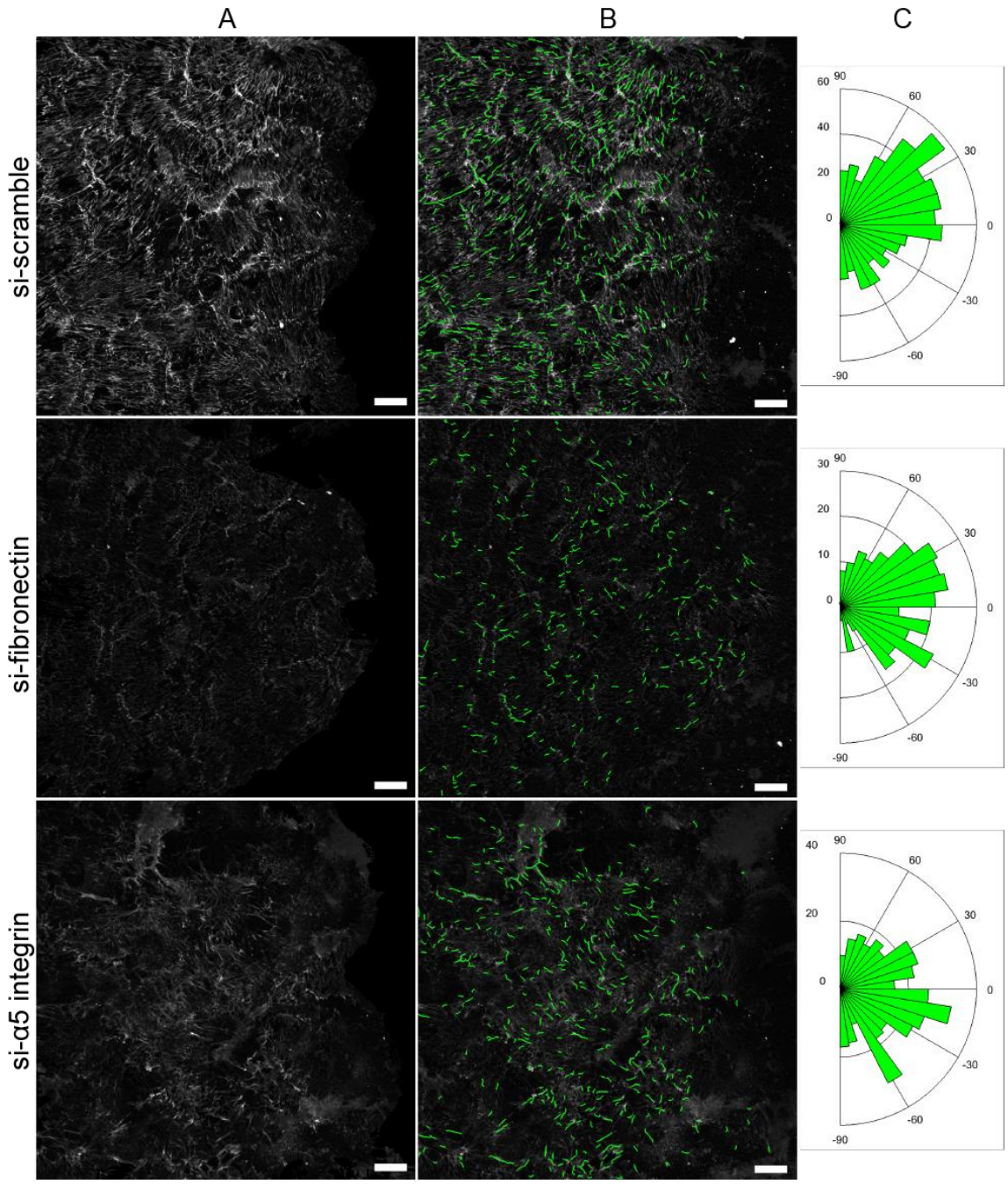

Figure 3.42: Fibronectin fiber alignment was reduced on 4 kPa gels in the interface zone at 24 hours when α_5 integrin, but not fibronectin was knocked down. (A) Confocal microscopy images of fibronectin fibers. (B) MATLAB output showing identified fibers (green) overlaying the original image. (C) Fiber angle distribution. Scale bars = 20 µm.

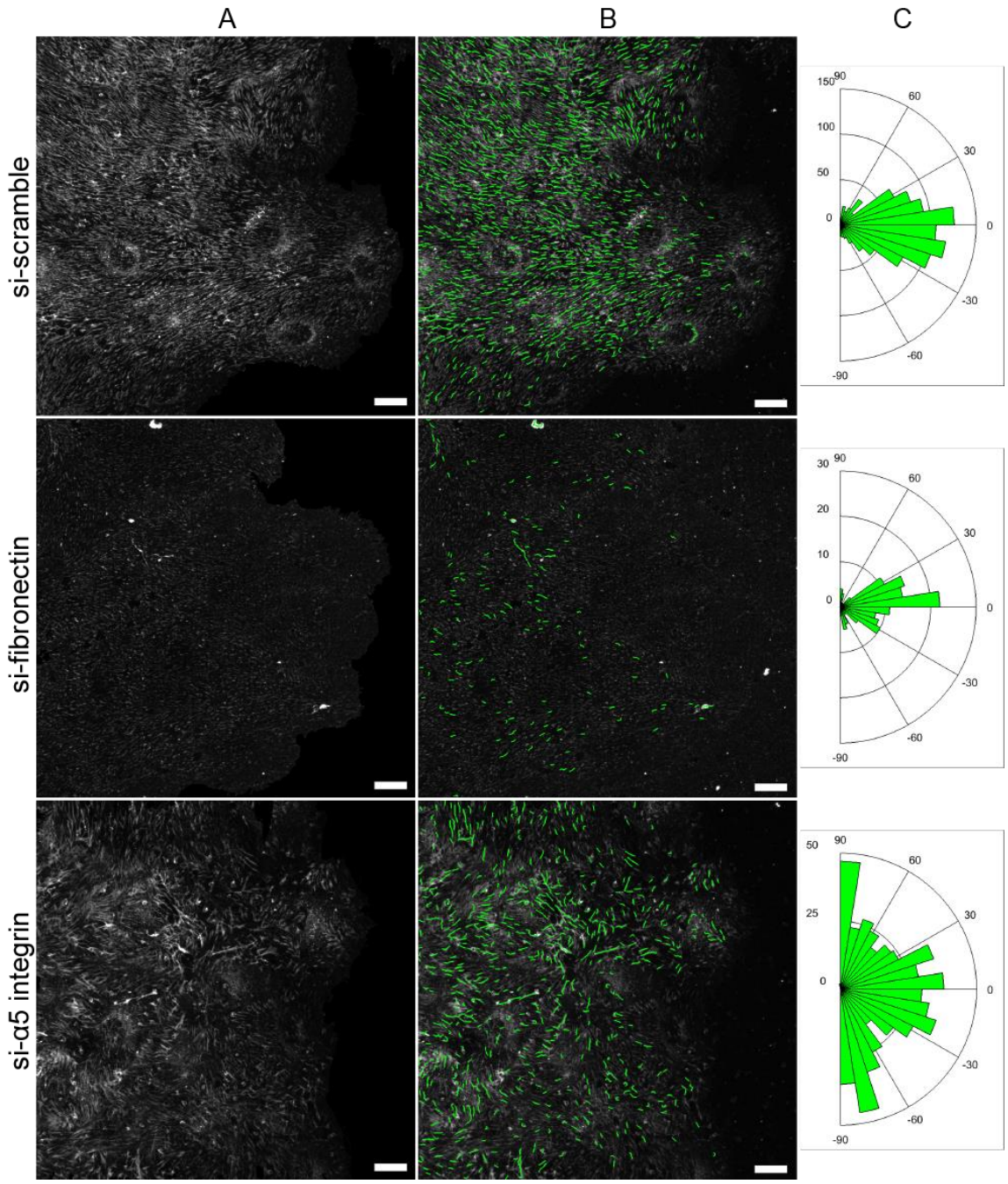

Figure 3.43: Fibronectin fiber alignment was reduced on 50 kPa gels at the interface zone at 24 hours when α_5 integrin, but not fibronectin was knocked down. (A) Confocal microscopy images of fibronectin fibers. (B) MATLAB output showing identified fibers (green) overlaying the original image. (C) Fiber angle distribution. Scale bars = 20 µm.

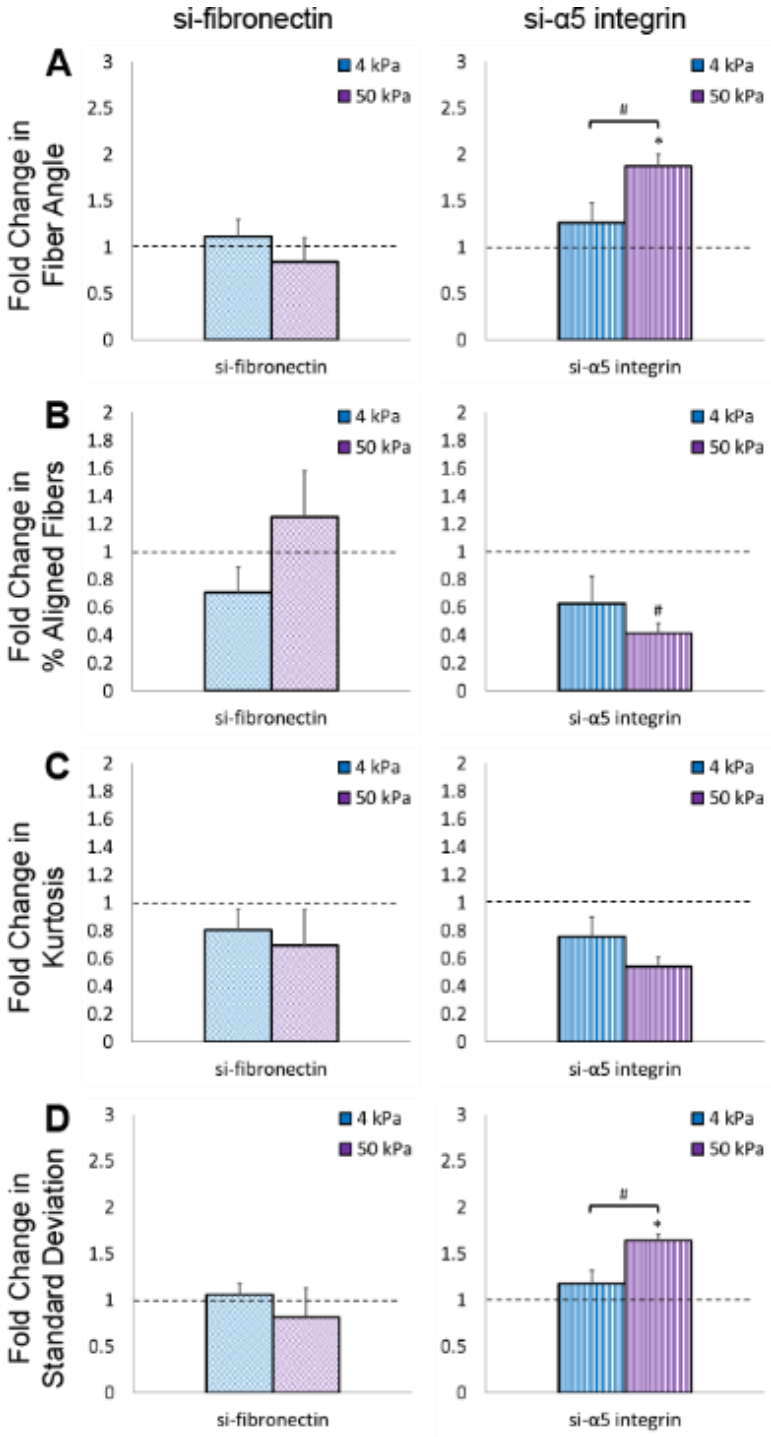

Figure 3.44: Fibronectin fiber alignment was decreased by α_5 integrin but not fibronectin knockdown at the interface at 24 hours. Fold changes compared to si-scramble in (A) average fiber angle, (B) percent of fibers aligned within 20° of the migration direction, (C) kurtosis of the distribution, and (D) standard deviation of the distribution. #$p < 0.05$; *$p < 0.01$; compared to si-scramble unless otherwise noted.

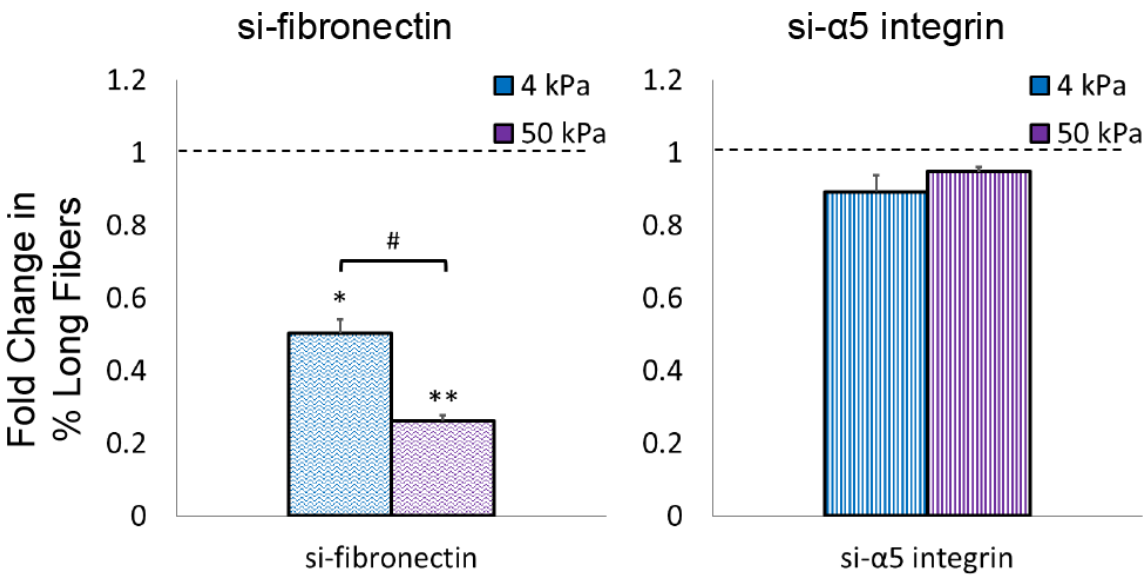

Figure 3.45: There were a reduced number of long fibronectin fibers with the fibronectin knockdown on both stiffnesses at the interface at 24 hours. These graphs represent the fold changes compared to si-scramble in number of long fibers (longer than 2.3 μm).

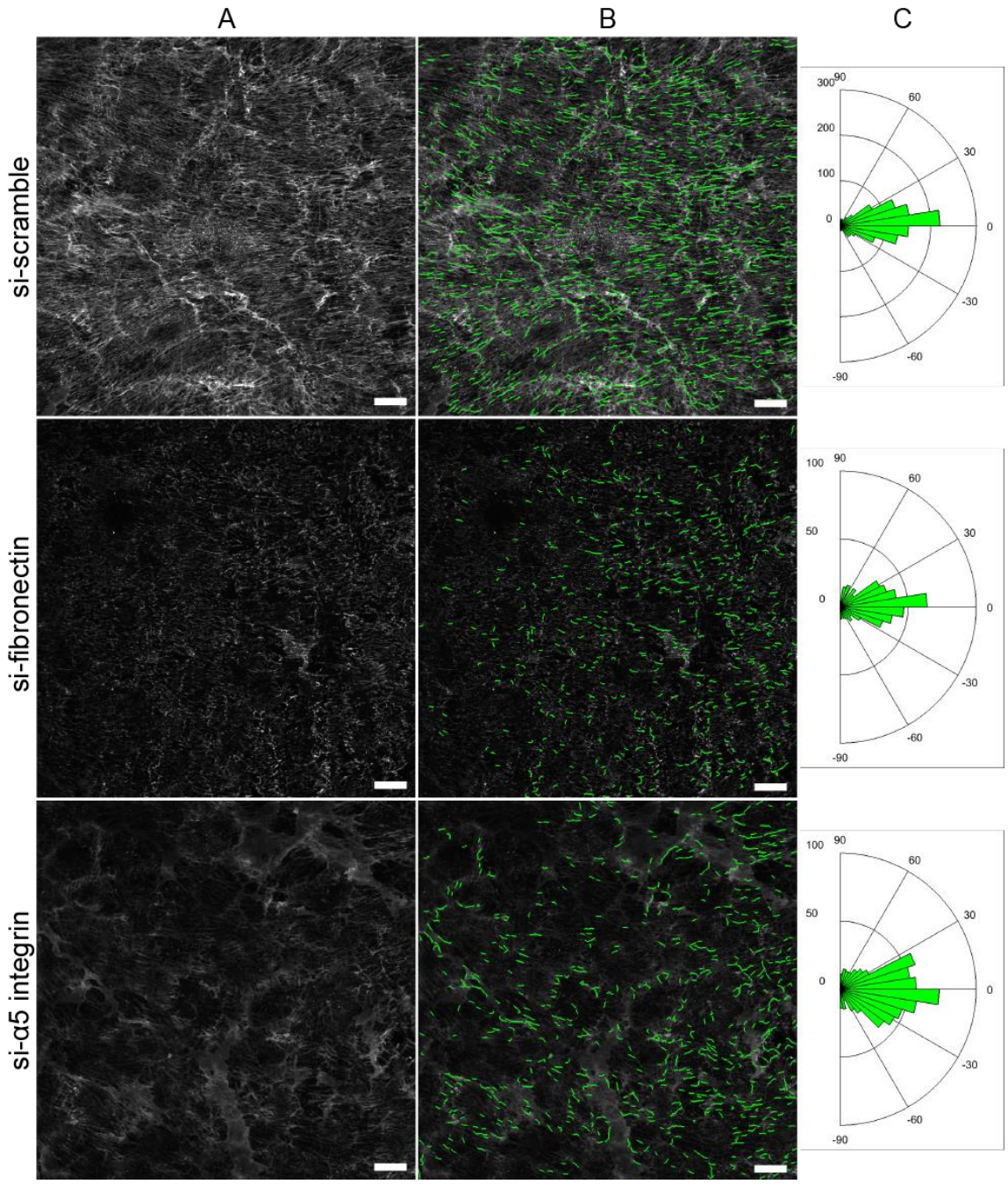

Figure 3.46: Fibronectin fiber alignment was reduced on 4 kPa gels at the migratory zone at 24 hours when α_5 integrin, but not fibronectin was knocked down. (A) Confocal microscopy images of fibronectin fibers. (B) MATLAB output showing identified fibers (green) overlaying the original image. (C) Fiber angle distribution. Scale bars = 20 µm.

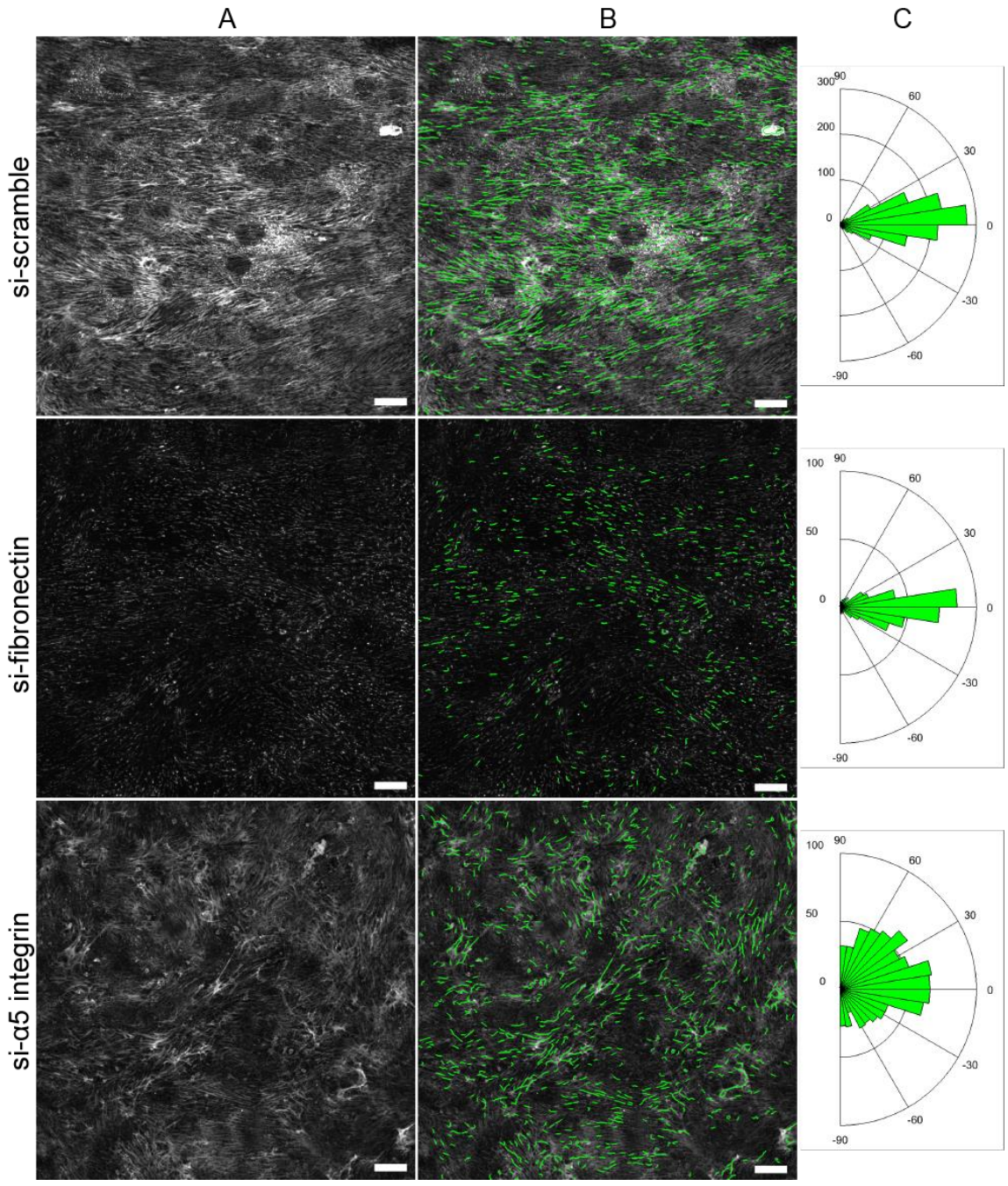

Figure 3.47: Fibronectin fiber alignment was reduced on 50 kPa gels at the migratory zone at 24 hours when α_5 integrin, but not fibronectin was knocked down. (A) Confocal microscopy images of fibronectin fibers. (B) MATLAB output showing identified fibers (green) overlaying the original image. (C) Fiber angle distribution. Scale bars = 20 µm.

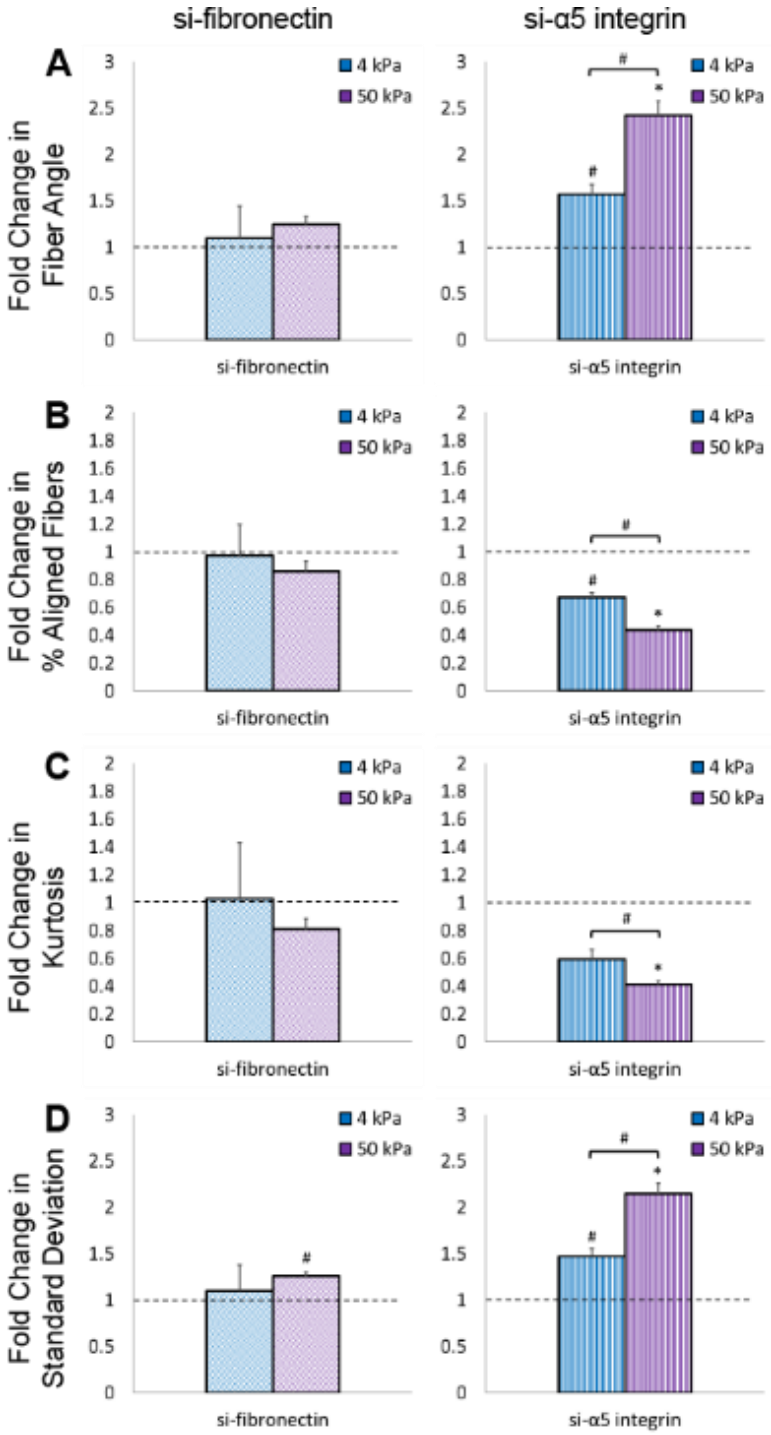

Figure 3.48: Fibronectin fiber alignment in the migratory zone was decreased by α_5 integrin but not fibronectin knockdown at 24 hours. Fold changes compared to si-scramble in (A) average fiber angle, (B) percent of fibers aligned within 20° of the migration direction, (C) kurtosis of the distribution, and (D) standard deviation of the distribution. #$p < 0.05$; *$p < 0.01$; compared to si-scramble unless otherwise noted.

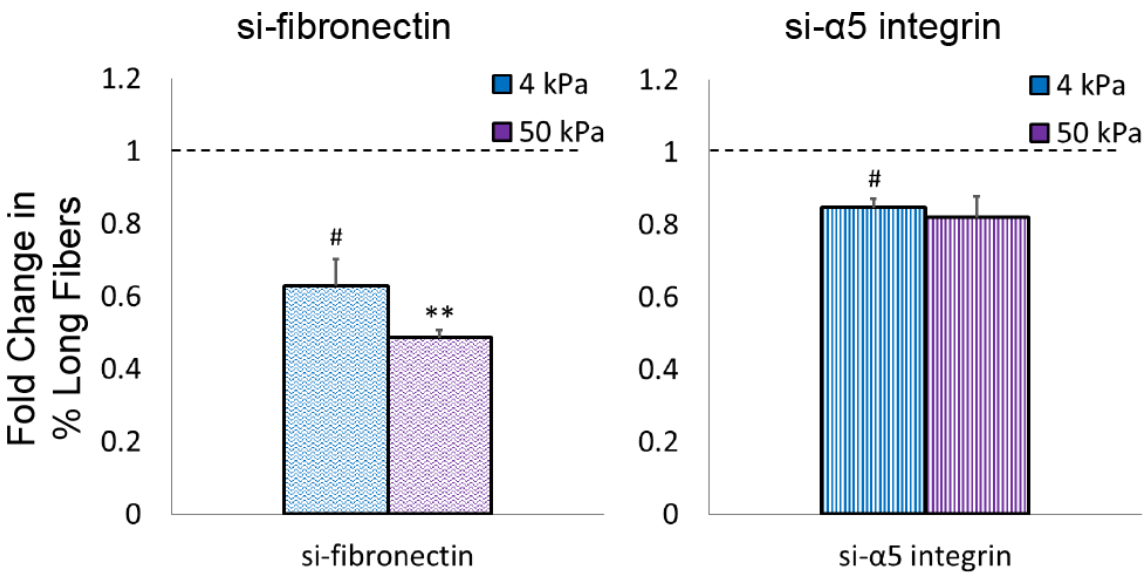

Figure 3.49: There were a reduced number of long fibronectin fibers with the fibronectin knockdown on both stiffnesses at the migratory zone at 24 hours. These graphs represent the fold changes compared to si-scramble in number of long fibers (longer than 2.3 μm).

3.4. Discussion

Collective endothelial cell migration is an important aspect of re-endothelialization after percutaneous intervention, which is essential to preventing re-stenosis. We show that collective endothelial cell migration distance is a function of substrate stiffness, which is often altered in cardiovascular disease. Specifically, PAEC collectively migrated a greater distance with increasing substrate stiffness. We report here that PAEC became most aligned within the migratory front on intermediate stiffness substrates and that this was a function of both time and location within the migratory front. We also report that PAEC were larger and more elongated on intermediate and stiff substrates. In addition, cells were less together on the intermediate and stiff substrates, which resulted in increased cell proliferation. We further showed that ROCK-mediated contractility inhibited collective migration on soft substrates, but not on stiff substrates. We also report that α_5 integrin was essential for enhanced collective migration on stiff substrates. These

findings will help understand factors promoting and preventing endothelial cell collective migration in arterial disease progression after intervention as well as in successful vascularization of tissue-engineered constructs.

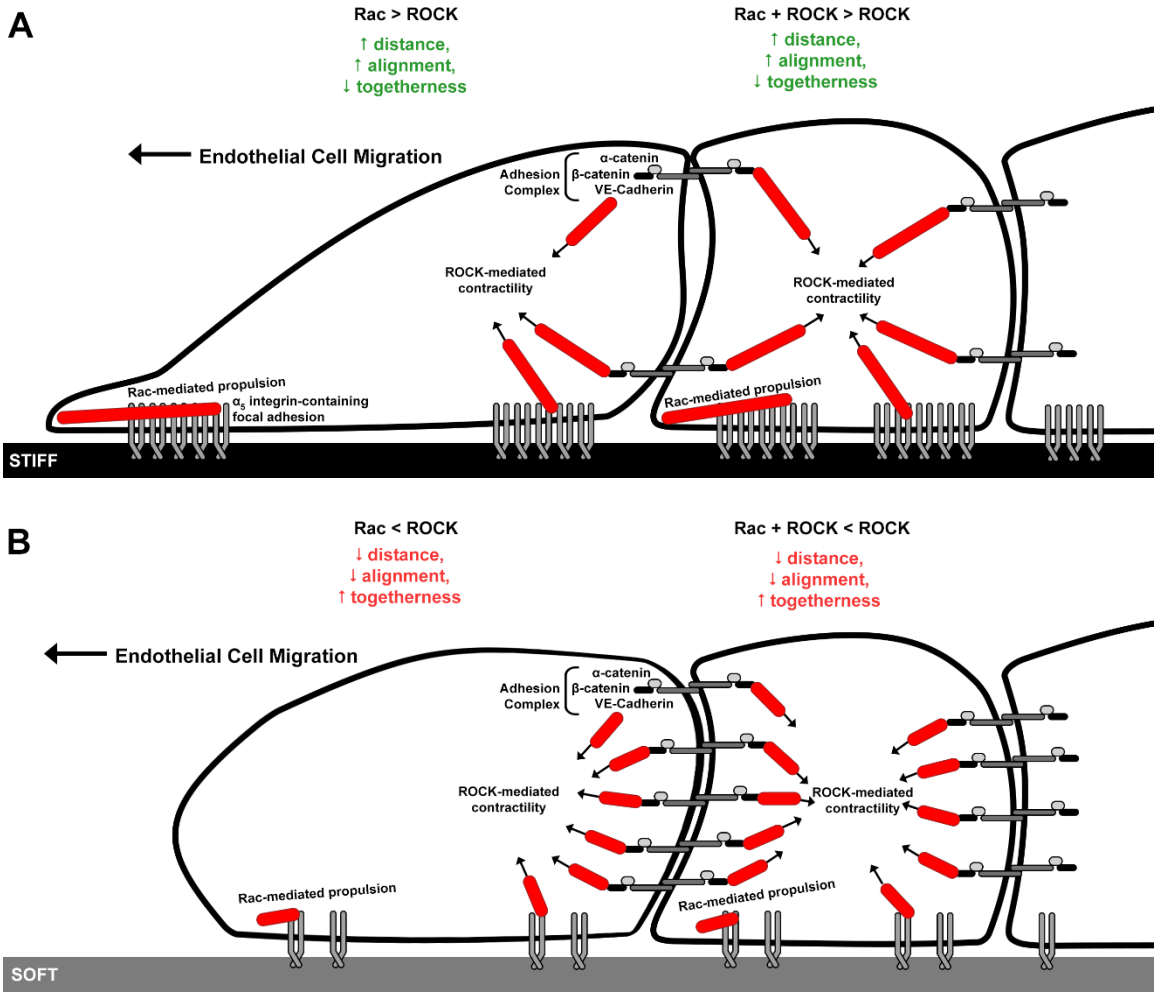

Figure 3.50: Schematic model of collective migration on substrates of varied stiffness. (A) EC on stiff substrates make large and stable α_5-containing focal adhesions that serve as a base for Rac-mediated forward propulsion. This forward propulsion at both the interface and migratory zones overcomes the ROCK-mediated contractility pulling against rear-end focal adhesions and cadherin complexes. EC are more aligned during migration with gaps between focal cadherin complexes. (B) EC on soft substrates do not make focal adhesions, and therefore elicit decreased Rac-mediated propulsion. ROCK-mediated contractility inhibits forward migration distance and alignment with increased cell-cell membrane integrity.

Our data suggest that endothelial cells on stiff substrates collectively migrate farther than cells on soft substrates due to increased Rac over Rho/ROCK signaling (Figure 3.50). Rac localizes to the cell leading edge, where it is activated by the FAK/Src complex[54, 133, 134] in focal adhesions. Activated Rac then mediates forward protrusions by promoting actin polymerization. FAK/Src also activates Rho/ROCK,[54] which pulls on and therefore dismantles polymerized actin bound to focal adhesions.[130] On stiff substrates, Rac dominates over Rho/ROCK at the leading edge because the focal adhesions are larger and more stable. These focal adhesions help Rac polymerize actin to create stable filopodia in the migration direction. These focal adhesions also resist ROCK-induced focal adhesion dismantling. In addition, Rac inhibits Rho/ROCK signaling.[135, 136] Rho/ROCK is therefore inhibited at the leading edge by Rac and is more active at the rear of the cell, where it promotes tail retraction. In our samples, endothelial cells on stiffer substrates likely have more FAK/Src activation to increase both Rac and Rho/ROCK signaling; however, due to larger, more stable focal adhesions on stiff substrates, Rac dominates over Rho/ROCK to promote cell collective migration. This may explain why PAEC migrated farther on stiffer substrates.

Surprisingly, we found that Rho/ROCK inhibition increased cell migration distance on softer substrates. On soft substrates, endothelial cells have lower Rac-induced propulsion and higher Rho/ROCK induced contractility. This Rho/ROCK activity is evenly distributed throughout the cell. When ROCK is inhibited, then Rac can dominate and propel the cell forward so that cell migration distance increases. Since cells on soft substrates already have weaker focal adhesions, or perhaps even only focal contacts, they may not need Rho/ROCK activation to retract the cell tail in cell migration (Figure 3.50).

siRNA knock down of α_5 integrin impaired stiffness-dependent endothelial cell collective migration, with greater impairment in cells on stiffer substrates. This suggests that α_5 may specifically be required to activate Rac at the leading edge to promote propulsion (Figure 3.50).

Of the two primary integrin heterodimers that bind fibronectin, $\alpha_5\beta_1$ but not $\alpha_V\beta_3$ integrin is found in stable focal adhesions[137] required for Rac-mediated actin polymerization. $\alpha_V\beta_3$ integrin is found in focal contacts which are more easily dismantled and have higher turnover rates.[98] We therefore believe that $\alpha_V\beta_3$ integrin is present in probing filopodia whereas $\alpha_5\beta_1$ integrin is present in focal adhesions behind the probing filopodia that represent the direction in which the cell is moving. Therefore $\alpha_V\beta_3$ integrin is likely important for mechanotransduction as the cell explores the environment, whereas $\alpha_5\beta_1$ integrin is critical to cell migration and stable morphological changes in response to substrate stiffness. We show supporting evidence that the requirement for α_5 integrin for Rac activation in PAEC collective migration is dependent on substrate stiffness.

Interestingly, when fibronectin was knocked down, there was minimal change in collective migration regardless of substrate stiffness. This suggests that $\alpha_5\beta_1$ binds to other ligands. $\alpha_5\beta_1$ integrin has specific affinity for the RGD site on fibronectin.[138] RGD sites can also be found on collagens, laminins, and vitronectin. Our substrates were coated with type I collagen. Therefore it is possible that $\alpha_5\beta_1$ integrin binds to RGD sites on collagen or other matrix proteins secreted by the endothelial cells or adsorbed from serum. Alternatively, other integrins may compensate for the loss of $\alpha_5\beta_1$-fibronectin binding in the fibronectin knockdown cells. For example, $\alpha_V\beta_3$ compensates for loss of $\alpha_5\beta_1$ by knockout to maintain cellular adhesion and spreading in murine embryonic cells,[139] and therefore $\alpha_V\beta_3$-vitronectin binding could compensate in collectively migrating EC. However, $\alpha_V\beta_3$ does not form large focal adhesions.[137] $\alpha_2\beta_1$ integrin is the primary integrin for collagen I. However, $\alpha_2\beta_1$ integrin does not activate Rac.[140] Therefore we believe based on our α_5 integrin knockdown experiments that α_5 integrin is binding to ligands other than fibronectin.

While we now show that endothelial cells collectively migrate farther and faster on stiff substrates, others have previously shown that single cells migrate faster on soft substrates.[64]

Single cell motility includes three parts: actin polymerization at the front end, myosin II contractility in the center, and tail retraction at the back end. These three processes cycle in tandem to produce effective motility. Single cells migrate faster on soft substrates because they have a high rate of focal adhesion turnover. In contrast, collective migration requires coordination between focal adhesions and cell-cell junctions. While endothelial cell collective migration has not been studied prior to our work, epithelial cells collectively migrate faster on stiff substrates due to mechanical coupling via cadherins on adjacent cell-cell junctions.[48] These cadherin interactions are critical to cell coordinated movement, and this coordinated movement moves further into the migrating cell monolayer on stiffer substrates. This suggests that these cadherin signals are stronger with substrate stiffness. Therefore neighboring and following cells in collective migration serve as an additional external force that is transduced into an intracellular signal.

This cell-cell junction force enables cells to better coordinate movement, and paradoxically, increase cell migration speed. We believe that Rho/ROCK is critical to the difference in cell migration speed vs. substrate stiffness in individual vs. collective cell migration. In individual cells, Rac propels the cell forward and ROCK mediates tail retraction. Both Rac and ROCK are activated by focal adhesion signaling only. However, in collective cells Rho/ROCK but not Rac is also activated by cell-cell junctions, specifically VE-cadherin. Therefore in collective cell migration on stiff substrates, focal adhesion-activated ROCK and VE-cadherin activated ROCK work together to decrease migration resistance at the cell tail. In collective migration on soft substrates, there is inadequate ROCK activation from either focal adhesions or cell-cell junctions and therefore Rac is highly resisted by the cell tail.

ROCK inhibition increased PAEC collective migration distance on soft, but not the stiffest substrates. In single fibroblasts seeded on glass, blocking ROCK with Y27632 led to tail elongation

without inhibition of forward protrusion, suggesting that myosin II is not required for propulsion but only tail retraction.[141] This group showed that impaired tail retraction results in more elongated and directed fibroblasts during migration. ROCK inhibition has been shown to increase single fibroblast migration speed and directedness.[127, 142] This could explain our findings that PAEC directedness and collective migration distance increase with ROCK inhibition on soft substrates. However, this finding was substrate stiffness dependent. On stiff substrates, PAEC were more aligned in the migration direction, but did not migrate farther when ROCK was inhibited. This may suggest that tail elongation occurs regardless of substrate stiffness.

We observe that endothelial cells do not completely break free from neighboring cells, even on the stiffest substrates. Normal endothelial monolayers maintain cell-cell contacts during migration and it is the loss of cell-cell adhesion that is the principal finding in endothelial cells that have undergone endothelial-to-mesenchymal transition.[143] In many cancerous epithelial cells, the loss of E-cadherin is an early step in becoming an invasive carcinoma and eventually metastasizing.[144] This suggests that in endothelial cells, cadherin-based focal contacts provide greater tension than cell-ECM focal contacts. This ensures that endothelial cells migrate collectively rather than individually.

We report here that endothelial cell were contact inhibited on soft substrates but underwent significant proliferation on intermediate and stiff substrates. In addition, we show that this proliferation is a function of location within the migratory front. Endothelial cells proliferated at a higher rate closer to the interface where there was less cell-cell interaction. Contact inhibition decreases proliferation in confluent endothelial cells, for example in cells that were less sensitive to VEGF-induced mitosis when confluent as compared to sparsely-seeded endothelial cells.[25] In our studies, proliferation likely also contributed to substrate stiffness-dependent collective

migration distance as more endothelial cells were available to populate the migratory front on stiffer substrates.

While our data show novel dependence of endothelial cell collective migration on substrate stiffness, they are not without limitations. We used an *in vitro* two-dimensional model, in which substrate stiffness is varied using elastic rather than viscoelastic polyacrylamide gels. These gels were coated in a single matrix protein, collagen, rather than the rich variety of proteins present in the vascular extracellular matrix. We also did not include other mechanical stimuli, such as fluid flow and cyclic stretch, or other relevant cell types, such as smooth muscle cells and pericytes. Finally, aortic endothelial cells may not show the same response and therefore be relevant to small-vessel phenomena, including angiogenesis. In the future, we hope to conduct similar experiments in animal models, such as elastin insufficient mice which have stiffer vessels.[145]

In conclusion, we provide evidence that α_5 integrin is important for EC propulsion on stiff substrates. Furthermore, we show that ROCK-mediated contractility inhibits collective migration speed on soft substrates. These interesting results show two different mechanisms by which substrate stiffness affects EC collective migration.

4. The Effect of Substrate Stiffness on the Endothelial Response to Exogenous Stimuli in Collective Migration

4.1. Introduction

Substrate stiffness has been shown to affect the cellular response to external stimuli, such as growth factors and cytokines. The mechanical properties of the substrate, primarily transduced through integrin activation, affects how sensitive an endothelial cell is to a particular stimulus. For example, vascular smooth muscle cells exhibit enhanced sensitivity to platelet-derived growth factor on stiff substrates compared to soft substrates, leading to increased proliferation.[146] In addition, the type of integrin activation has been shown to affect crosstalk among growth factor receptors. Angiogenesis induced by fibroblast growth factor-2 (FGF2) and vascular endothelial growth factor (VEGF) has been shown to require $\alpha_V\beta_3$ and $\alpha_V\beta_5$ integrins, respectively.[147]

Endothelial cells are important in initiating and propagating local inflammation after endothelial injury. In response to endothelial injury and the subsequent inflammatory response, activated endothelial cells transport p-selectin from Weibel-Palade bodies (WPBs) near the nucleus to the cell membrane.[148] P-selectin is then expressed on the endothelial cell surface.[149-151] P-selectin expression initiates leukocyte rolling, i.e. the ability for endothelial cells to make low-affinity bonds with white blood cell surface receptors as they move through the vessel. This is the first step in diapedesis, or leukocyte extravasation from inside the vessel to extravascular interstitium.[150]

P-selectin expression at the endothelial cell surface occurs in both acute and chronic phases. The acute phase begins within minutes of activation by thrombin, and p-selectin comes from stored protein in WPBs.[149] The acute phase is initiated by thrombin-induced reactive oxygen species (ROS) in human umbilical vein endothelial cells (HUVEC).[149] ROS are important sources of endothelial damage due to reperfusion injury

after intervention. The chronic phase occurs 4-6 hours after activation and depends on new p-selectin protein synthesis.[149] Generally speaking, continued p-selectin expression at the cell membrane enables atherosclerotic lesion progression.[152] Arterial stiffness is also a risk factor for atherosclerosis.[153] However, the effect of substrate stiffness on endothelial cell p-selectin has not yet been explored.

Endothelial-to-mesenchymal transition (EndMT) is defined as the transdifferentiation of endothelial cells to myofibroblast-like cells,[154] an analogous process to epithelial-to-mesenchymal transition (EMT). EndMT has been of growing interest since it was suggested to contribute to heart valve and cardiac fibrosis.[155] EndMT has also been investigated as a source of cancer-associated fibroblasts.[156] Although evidence suggests that EndMT is harmful in chronic disease states, there may be applications in tissue engineering if we can understand what regulates this process. In addition to myofibroblast-like cells, EndMT has been shown to result in cells that resemble MSCs, which could be subject to further differentiation in a developing organ.[154] Transforming growth factor-β2 (TGF-β2) is one of the primary growth factors to induce EndMT via Smad2/3 signaling.[157] Although TGF-β signaling for MSC differentiation has been shown to be affected by substrate stiffness,[158] how substrate stiffness affects TGF-β2-induced EndMT remains unknown.

Angiogenic growth factors, such as vascular endothelial growth factor (VEGF) and fibroblast growth factor (FGF2), bind to growth factor receptors (GFRs) on the cell surface, which are membrane-bound tyrosine kinase receptors (RTKs). In response to growth factor binding, RTKs become activated and phosphorylate secondary messenger proteins to initiate downstream signaling pathways include Ras/Raf/MAPK, PI3K/Akt, and PIP_3/DAG/PKC. Through these signaling pathways, angiogenic growth factors ultimately promote important cellular processes such as survival, proliferation, and migration.[159]

GFRs exhibit crosstalk with integrins, transmembrane heterodimers that enable cell binding to extracellular matrix proteins. The importance of this crosstalk is evidenced by the finding that exogenous growth factors can only elicit cell survival, proliferation, migration, and differentiation in attached cells.[160] Integrins and GFRs interact both indirectly and through direct activation. For indirect crosstalk, integrin and GFR signaling pathways overlap, primarily through Ras-MEK-MAPK, PI3K-Akt, and Rho pathways. This overlap may enhance intracellular signaling from combined extracellular stimuli. Activated integrins can further activate GFR in the absence of an extracellular growth factor, termed direct activation.[160] Epidermal GFR (EGFR) phosphorylation occurs after $\alpha_V\beta_3$ and β_1 integrin co-clustering with EGFR.[161, 162] $\alpha_V\beta_3$ integrin complexes with and activates platelet-derived GFR (PDGFR).[163] $\alpha_V\beta_3$ also directly activates fibroblast GFR type 1 (FGFR1) upon extracellular exposure to FGF2 and fibrinogen, but not vitronectin.[164]

Substrate stiffness impacts integrin localization and activation, and may also impact growth factor signaling. Stiffer substrates induce larger, stronger focal adhesions and produce a more organized cytoskeleton that transmits larger traction forces throughout the cell.[67] Enhanced integrin recruitment and activation with substrate stiffness leads to increased integrin signaling that in turn affects cell function. ECs, SMCs, fibroblasts, epithelial cells, and glioma cells survive, proliferate, and migrate more on stiff substrates when sparsely cultured,[123, 165-168] but understanding about how cellular functions are affected by substrate stiffness when in monolayers is still lacking. In one study, smooth muscle cell response to PDGF was enhanced on stiff substrates due to PDGFR co-localization with integrins in lipid rafts.[146] Endothelial cells migrate toward growth factor gradients during angiogenesis.[23, 24, 169] However, investigation of how substrate stiffness affects endothelial cell migratory response to pro-angiogenic growth factors has yet to be explored.

We hypothesized therefore that substrate stiffness impacts endothelial cell sensitivity and response to inflammatory stimuli, EndMT stimuli, and pro-migratory growth factors. In this chapter, we investigated the role of substrate stiffness in endothelial cell activation in response to TGF-β, VEGF, and FGF2. We include preliminary data suggesting that substrate stiffness affects expression of the pro-inflammatory marker p-selectin and the EndMT marker α-SMA within the migratory front. We also show that substrate stiffness does not affect the collective migration distance after a one-time globally-available dose of VEGF or FGF2.

4.2. Methods

4.2.1. Polyacrylamide Hydrogels

Polyacrylamide (PA) hydrogels were made as previously described in Chapter 3.

4.2.2. Cell Culture

Porcine aortic endothelial cells (PAEC) were used as previously described in Chapter 3.

4.2.3. Cage Migration Assay

A modified cage assay was implemented as previously described in Chapter 3.

4.2.4. Immunocytochemistry

For fluorescent labeling, samples were prepared as previously described in Chapter 3. Primary antibody solutions were diluted in 1% BSA and include mouse anti-α-SMA (1:250), rabbit anti-VE-cadherin (1:250), and mouse anti-p-selectin (1:250). Samples were incubated overnight at 4°C. After thorough rinsing, samples were incubated with secondary antibody solution

including goat anti-mouse IgG AlexaFluor® 488 (1:250), goat anti-rabbit IgG AlexaFluor® 633 (1:250), rhodamine phalloidin (1:100, F-actin label), and Hoechst 33342 (1:2000, nuclear label) in 1% BSA. After 1 hour at room temperature, samples were rinsed with PBS and stored in PBS at 4˚C until use.

4.2.5. Imaging

Imaging techniques were completed as previously described in Chapter 3.

4.2.6. Image Quantification

All quantification methods were as previously described in Chapter 2.

4.2.7. Statistics

All experiments were done in duplicate or triplicate to confirm findings. Unless otherwise noted, data are represented as mean ± standard error of the mean in order to better reflect the precision of the mean. The mean ± standard error of the mean were calculated from averages of measures from 5+ images per sample from 2+ samples per condition. One-way ANOVA and post-hoc testing (least significance difference) were used to compare metrics across substrate stiffnesses. # denotes p-values less than 0.05, * denotes p-values less than 0.01, ** denotes p-values less than 0.001, and “n.s.” denotes a “non-significant” difference.

4.3. Results

4.3.1. Effect of Substrate Stiffness on P-Selectin Expression

Substrate stiffness effects on endothelial p-selectin expression were assessed using the cage migration assay. PAEC were seeded for 24 hours before being fixed and labeled for p-selectin (Figure 4.1-4.2). Surprisingly, p-selectin was only found in cells on 4 and 50 kPa, but not 14 kPa gels. This was true in both the interface (Figure 4.1) and migratory zones (Figure 4.2). Using a custom MATLAB algorithm to analyze the occupying area and total number of p-selectin granules, we found that PAEC on 14 kPa gels had negligible p-selectin granule area and number. In contrast, cells on both 4 kPa and 50 kPa substrates had p-selectin granules that occupied significantly greater peri-nuclear area than cells on 14 kPa substrates at the interface and migratory zones (Figure 4.3, $F = 10.73$, $p = 0.04$). Cells on 4 and 50 kPa substrates also have 41 and 45 times the number of p-selectin granules compared to 14 kPa substrates at the interface and migratory zones (Figure 4.3, $F = 2097$, $p < 0.0001$). PAEC on the 50 kPa substrates showed similar differences with the 14k Pa substrates. At the confluent zone, PAEC had low levels of p-selectin on all stiffnesses, similar to 14 kPa substrates in the other zones (data not shown).

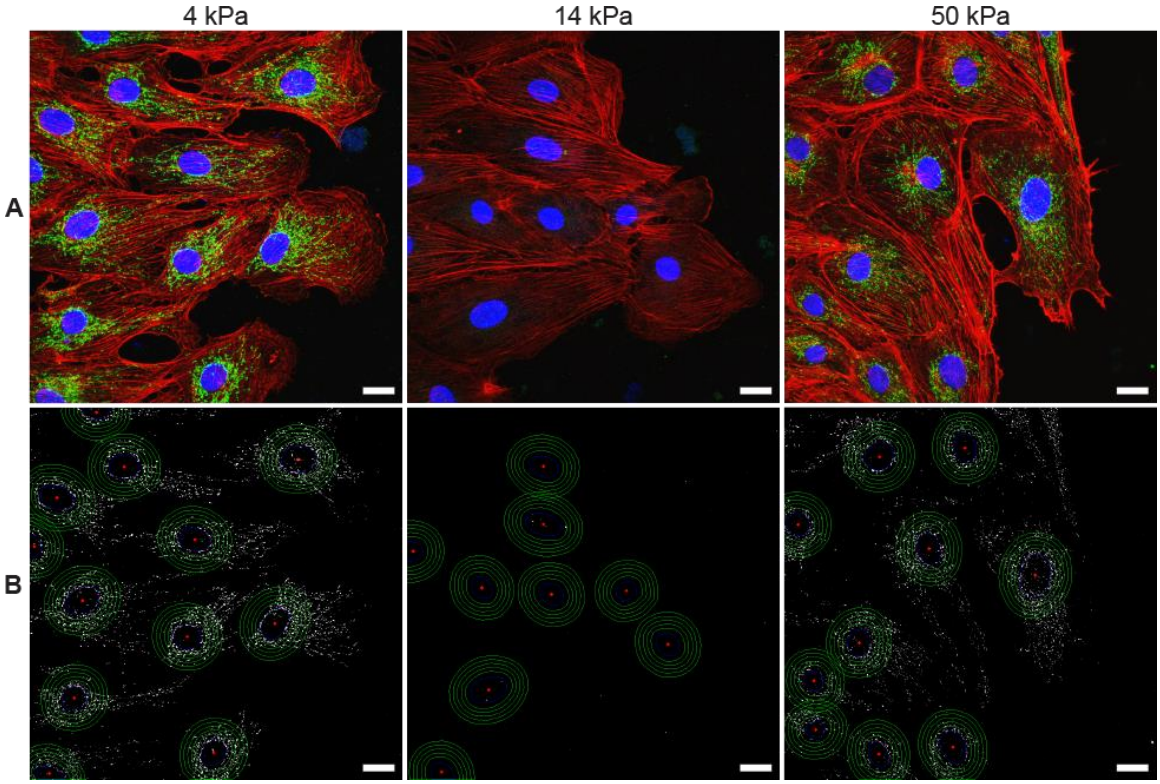

Figure 4.1: PAEC p-selectin expression in the interface zone was higher on 4 and 50 kPa gels as compared to 14 kPa gels. (A) PAEC were fixed after 24 hours in the cage migration assay and labeled for p-selectin (green), F-actin (red), and nuclei (blue). (B) The size and number of p-selectin granules (white) were calculated as a function of distance from the nucleus (green bands). Scale bars = 20 μm.

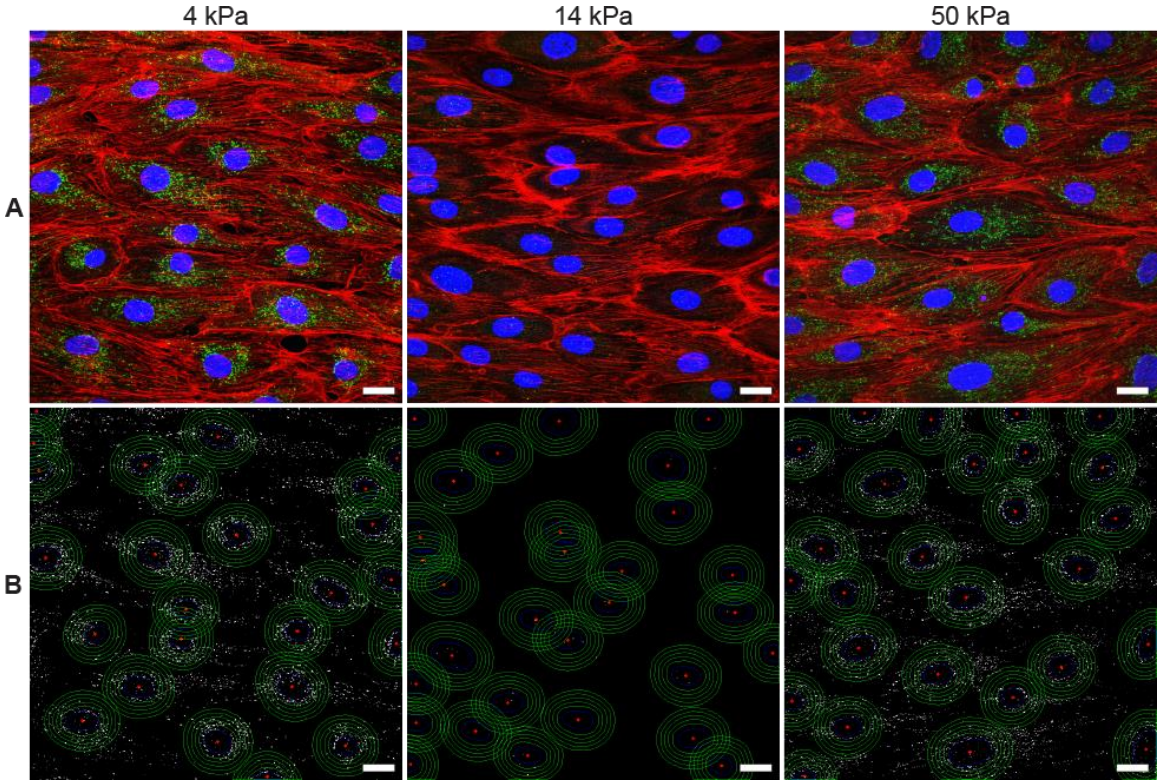

Figure 4.2: PAEC p-selectin expression in the migratory zone was higher on 4 and 50 kPa gels as compared to 14 kPa gels. (A) PAEC were fixed after 24 hours in the cage migration assay and labeled for p-selectin (green), F-actin (red), and nuclei (blue). (B) The size and number of p-selectin granules (white) were calculated as a function of distance from the nucleus (green bands). Scale bars = 20 µm.

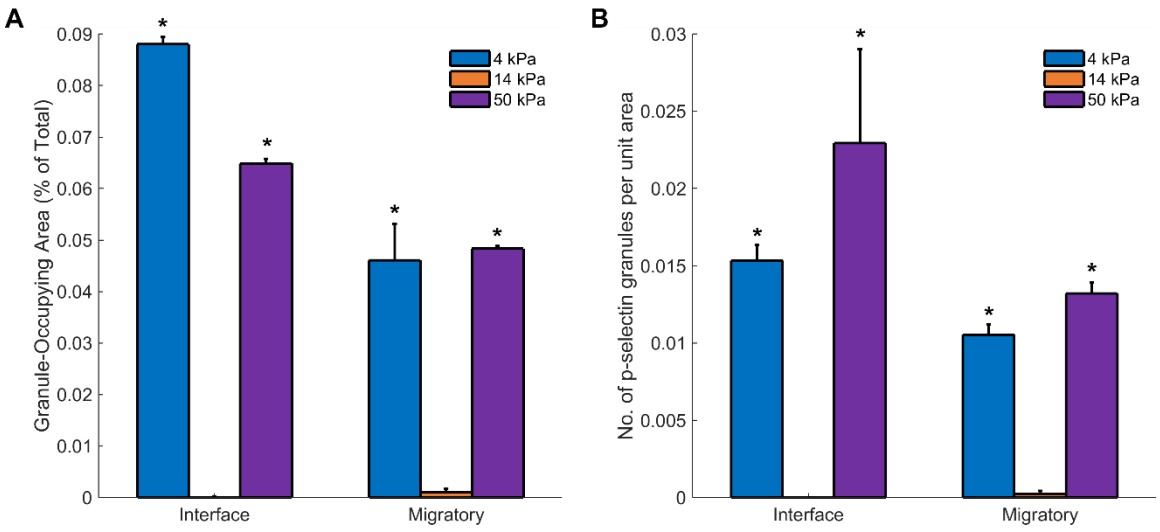

Figure 4.3: PAEC on 4 and 50 kPa gels had larger and more numerous p-selectin granules compared to cells on 14 kPa gels. (A) Area occupied by p-selectin granules within the largest peri-nuclear band divided by total area of the band interior. (B) Number of p-selectin granules per unit area quantified within the largest peri-nuclear band. *$p < 0.01$; compared to 14 kPa substrates.

4.3.2. Effect of Substrate Stiffness on TGF-β-Induced EndMT

To determine if substrate stiffness affects EndMT, α-smooth muscle actin (α-SMA) was measured during endothelial collective migration. PAEC were seeded in a 24 hour cage migration assay. To validate our markers, we found that PAEC with high α-SMA (green arrows, Figure 4.4) had corresponding low VE-cadherin (green arrows, Figure 4.4). The opposite was true for non-transitioned PAEC (red arrows, Figure 4.4), with low α-SMA and high VE-cadherin.

We used TGF-β2 to stimulate EndMT in cells on substrates of varied stiffness to determine how substrate stiffness affects TGF-β2-induced EndMT. PAEC were seeded in the cage migration assay with 10 ng/mL TGF-β2 from 0-24 hours before fixation and labeling for α-SMA (Figure 4.5). A custom MATLAB algorithm was developed to identify which cells within the migratory front were SMA^{+}. Surprisingly, we found that PAEC on 4 kPa gels had approximately triple and double the percentage of SMA+ cells compared to 14 and 50 kPa gels, respectively.

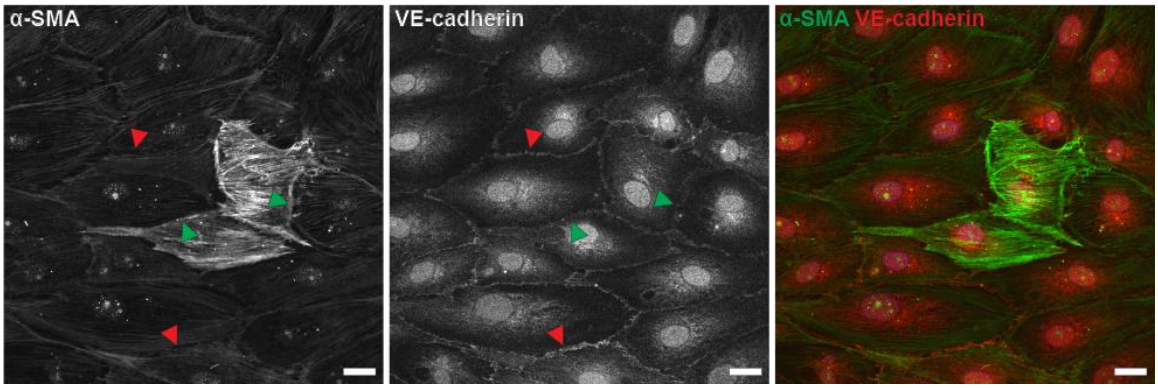

Figure 4.4: PAEC that transdifferentiate into myofibroblast-like cells express higher α-SMA and lower VE-cadherin. Representative image of PAEC with high α-SMA and low VE-cadherin (green arrows), as well as low α-SMA and high VE-cadherin (red arrows). Scale bars = 20 μm.

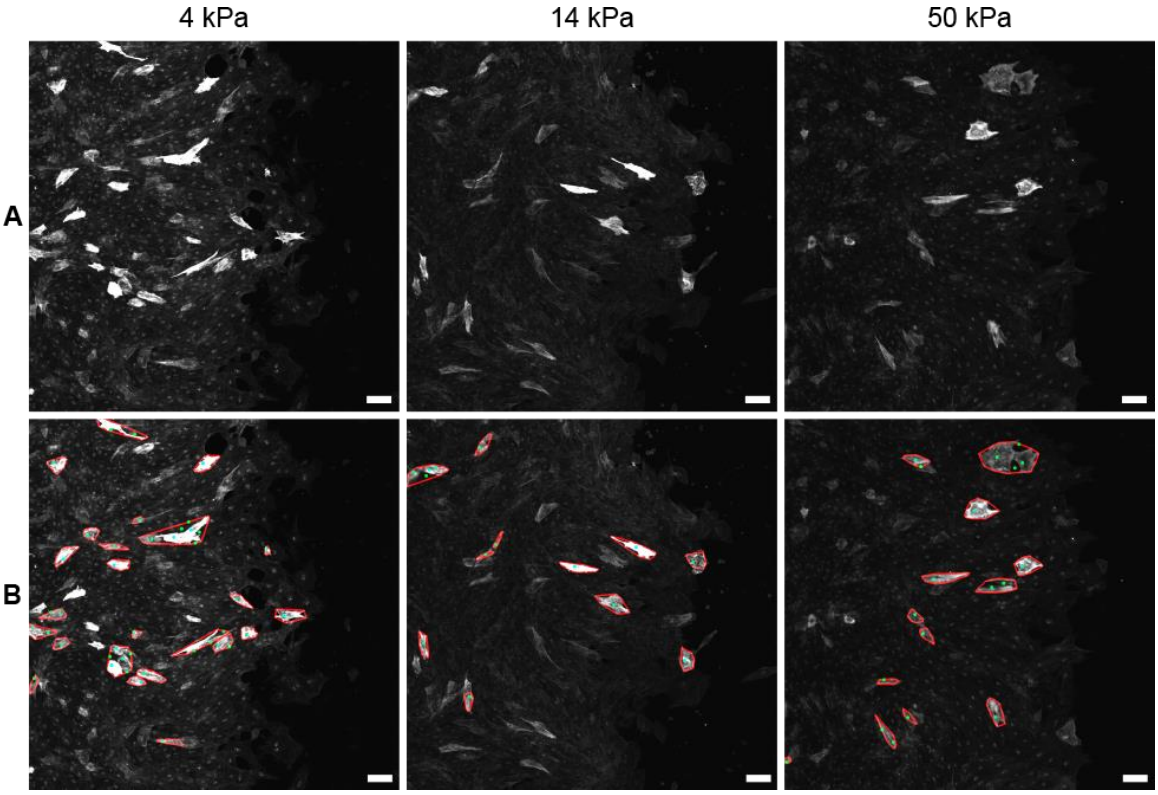

Figure 4.5: TGF-β2-induced EndMT occurred more often on 4 kPa gels as compared to 14 and 50 kPa gels. 10 ng/mL TGF-β2 was added at 0 hours and PAEC were allowed to migrate in the cage migration assay for 24 hours prior to fixation and labeling for α-SMA (white) (A) Representative confocal microscopy images. (B) Images were analyzed using a custom MATLAB algorithm to identify α-SMA-positive cells within the migratory front (red outline). Scale bars = 100 μm.

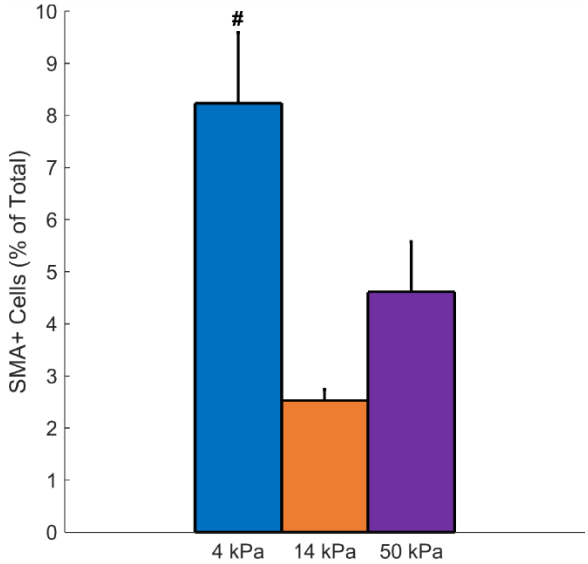

Figure 4.6: TGF-β2-induced EndMT and occurred more on 4 kPa gels as compared to 14 and 50 kPa gels. The percentage of SMA+ cells were quantified. #$p < 0.05$ compared to 14 kPa substrates.

4.3.3. Effect of Pro-Migratory Growth Factors on Collective Migration Distance

Growth factors exhibit signaling cross-talk with integrins. To determine substrate stiffness affects growth factor-integrin cross-talk, we examined two pro-angiogenic growth factors: vascular endothelial growth factor (VEGF) and fibroblast growth factor-2 (FGF2). PAEC were seeded in a 24 hour cage migration assay without any exogenous growth factors or with either 10 ng/mL VEGF or 10 ng/mL FGF2. Average migration distance did not differ with substrate stiffness (Figure 4.7).

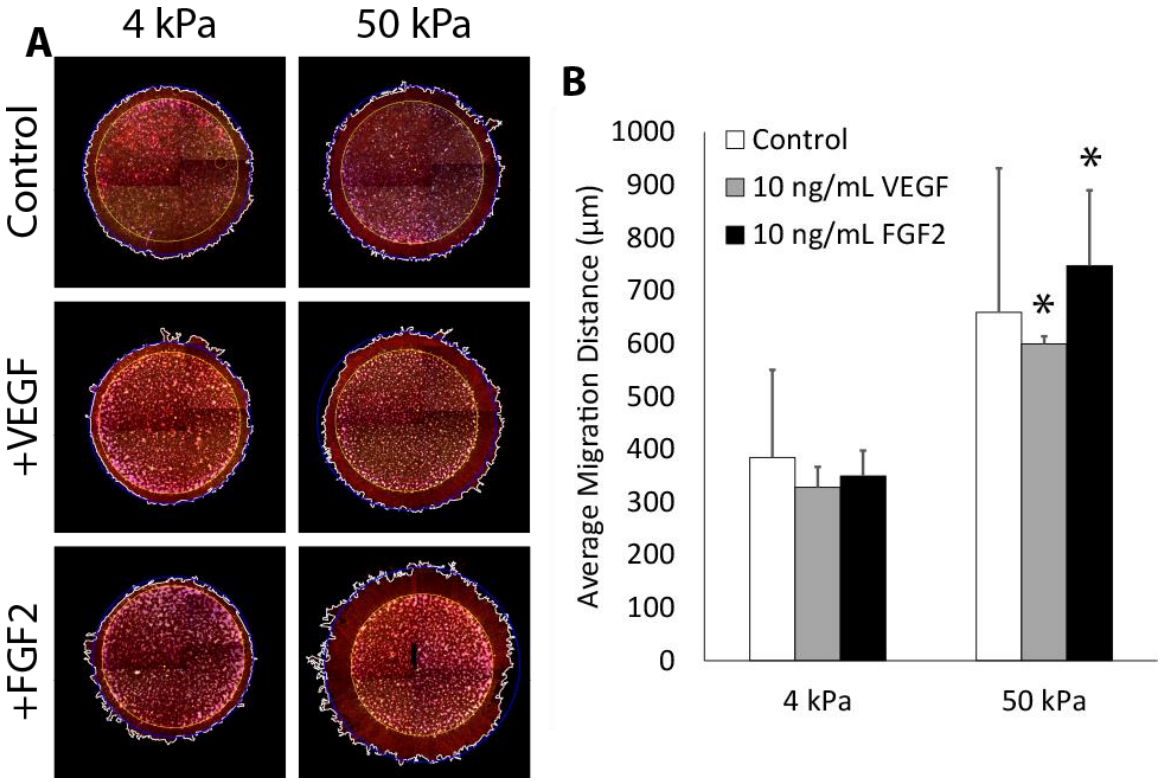

Figure 4.7: Global VEGF and FGF2 did not affect endothelial cell migration distance on substrates of any stiffness. (A) PAEC were seeded in 24 hour cage assays with 10 ng/mL VEGF, 10 ng/mL FGF2, or vehicle. Samples were fixed and labeled for F-actin (red) and nuclei (blue). A custom MATLAB algorithm was used to measure the average migration distance (blue circle) based on the outline of the cell front (white tracing). The average migration distance was the radial difference between the starting position (yellow circle) and the average advancement distance (blue circle). (B) Quantified average migration distance. Scale bars = 500 µm. *$p < 0.01$; compared to soft substrate within the same treatment condition.

4.4. Discussion

In this chapter, we examined how substrate stiffness affects endothelial cell expression of inflammatory markers and endothelial response to growth factors involved in endothelial-to-mesenchymal transition (EndMT) and endothelial cell collective migration.

We show surprising findings that p-selectin expression was greatest on soft and stiff, but not intermediate substrates. This unexpected finding suggests that there may be two different mechanisms by which p-selectin is controlled in response to substrate stiffness. Endothelial cells increase p-selectin expression in response to nitric oxide (NO) inhibitors, suggesting that local NO-derived vasodilation prevents p-selectin expression on endothelium.[148] Endothelial nitric oxide synthase (eNOS) has been shown to become activated through the Rho/ROCK pathway.[170] eNOS has also recently been shown to be activated earlier on soft substrates.[171] It is possible that endothelial cells express more p-selectin via impaired eNOS activation on stiff substrates. This provides evidence that an intermediate may be ideal for developing tissue-engineered substrates as it will lead to a lower level of inflammation.

We report another surprising finding that EndMT may be substrate stiffness dependent. Our preliminary data show that PAEC on soft substrates were more sensitive to TGF-β2 for EndMT induction. Focal adhesion kinase (FAK) is essential for epithelial-to-mesenchymal transition (EMT) in hepatocytes by up-regulating mesenchymal markers and delocalization of E-cadherin.[172] Substrate stiffness has been shown to be a switch for how epithelial cells response to TGF-β; TGF-β increases apoptosis on soft substrates and TGF-β increases EMT on stiff substrates.[173] These findings contradict our preliminary results, which might suggest that endothelial cells behave differently in response to substrate stiffness. Important information about the dynamic nature and reversibility of EndMT remains unknown. PAEC with increased myofibroblastic markers, in our experimental setup, were unable to fully escape their neighboring endothelial cells. It is

classical understanding that EC that undergo EndMT migrate away from a vessel into the interstitium. This may be a limitation with our experimental design.

We report that PAEC did not migrate farther in response to pro-migratory growth factors VEGF and FGF2 when given globally at the beginning of a 24-hour migration period. Most likely this is due to the poor control of the growth factor release profile. VEGF and FGF were given as a bolus dose at one time point rather than continuously released from a source to create a gradient. A more sophisticated model would be required to incorporate controlled growth factor release from a source to the migrating cell population. To this end, we began designing a microfluidic device that would provide a growth factor gradient to PAEC in the cage assay, but it was not fully validated for experimental use. Further work is needed to more accurately recapitulate *in vivo* conditions where cells migrate along chemokine gradients.

These results provide intriguing preliminary data for how substrate stiffness affects EC response to external stimuli. However, the work in this chapter is limited to observational studies without providing insights into possible mechanisms. The 24-hour time point chosen for these studies was based on observations relating to collective migration in Chapter 3. It is likely that these signaling pathways have dynamic effects occurring at much shorter time points. For example, endothelial p-selectin expression has been shown to respond within minutes to an external stimulus.[149] Overall these findings are promising, indicating that substrate stiffness does indeed affect EC response to both inflammation and growth factors.

5. Conclusions and Future Work

5.1. Thesis Summary

Cardiovascular disease remains the number one cause of mortality in the United States and is expected to burden the healthcare system with over $1 billion in costs by 2030.[1] It is therefore imperative that researchers investigate not only the underlying mechanisms of disease initiation and progression but also the mechanisms of post-interventional disease progression. For example, re-stenosis rates after percutaneous intervention with drug-eluting stents remain at about 20% within 5 years,[2] a high rate that is contributing to the exploding healthcare costs.

In this thesis, I investigated the mechanisms by which endothelial cells collectively migrate over substrates of varied stiffness. To accomplish this, I first developed a series of MATLAB image processing tools to automatically extract feature information from collectively migrating endothelial cells. By labeling ubiquitous cell structures, such as nuclei and actin, after cells were seeded in a modified cage assay, I was able to quantify nuclear orientation, cell area, migration distance, and interface roughness. Using other specialized labels, I was able to quantify cell elongation, subcellular compartmentalization, and fiber orientation.

Using these tools, I showed that endothelial cells migrated faster and farther on stiffer substrates. This finding is supported by Ng, *et al.* who showed that breast epithelial cells collectively migrated faster on stiffer substrates.[3] The group also reported increased directedness as we report. This means that endothelial and epithelial tissues show increased migration rate in the context of disease and aging where substrates are stiffer.[4] This increase in migration rate over stiffer tissues may be advantageous to hasten the healing process, particularly in the contexts of re-endothelialization,[5] angiogenesis in wound healing,[6] or neovascularization of an implanted tissue. Epithelial cells can lose their cell-cell contacts in cancer, promoting single cell metastasis rather than collective migration during the epithelial-to-mesenchymal transition.[7] In contrast to

endothelial and epithelial cells, fibroblasts tend to migrate as single cells, but have been shown to exhibit some coordinated movement when confined geometrically.[8] This growing understanding of how substrate stiffness affects collective migration rate will inform clinical therapeutic approaches toward preventing restenosis, promoting wound healing and closure, and limiting tumor growth and metastasis. In addition, vascularization remains the primary challenge to clinically-relevant tissue engineering therapeutics.[9] Creating scaffolds with specific mechanical properties could contribute to faster vascular ingrowth.[10] For example, one approach may be to develop a stiff scaffold that becomes softer like normal tissues over time as it is degraded and replaced by structures secreted and remodeled by cells.

These collective migration processes in endothelial cells required α_5 integrin, a subunit found as a heterodimer with β_1. This integrin has been found to be important in endothelial cell migration. In fact, expression of $\alpha_5\beta_1$ in endothelial cells increases during angiogenesis[11] and mice without α_5 integrin develop irregular vasculature and die within two weeks.[12] It primarily binds to the RGD site of fibronectin, a provisional matrix protein found at sites of acute healing.[13] Our findings are supported by similar studies in human keratinocytes where siRNA knockdown of α_3 integrin impaired collective migration over laminin.[14] We observed that diminished fibronectin did not impact collective migration, suggesting that α_5 integrin may be capable of low-affinity binding to other matrix ligands with RGD sequences. This could be applied to tissue engineered constructs with controlled density and organization of RGD binding sites to promote directed collective migration. Understanding how αVβ3 integrin, another specific integrin found to be upregulated in endothelial cells,[15] impacts collective migration remains unclear.

We showed that endothelial cells on stiffer substrates organized more aligned fibronectin fibers at their basolateral surface; however, this appears to be a result of increased cell alignment rather than the cause of the alignment. Control over fibronectin structure in matrix scaffolds may

still yield effective patterning for collective migration by revealing cryptic integrin binding sites.[16] Endothelial cells migrating on micropatterned collagen-coated PDMS were more directed when gaps between collagen strips were kept below 30 μm.[17] It is possible that the nanoscale fibronectin structure we observed was sufficient for individual cells to distinguish, but too small to cue directional information to groups of cells within a large monolayer. A more complex three-dimensional model that includes pre-patterned matrix fibers could by itself promote directed collective migration that we did not observe in our simplified two-dimensional model.

Although it's been shown that Rho/ROCK signaling mediates tail retraction,[18] but we show that it additionally inhibits forward migration in cells on soft substrates and upon ROCK inhibition, endothelial cells collectively migrated as fast on soft substrates as they do on stiff substrates. Ng, *et al.* showed that myosin II-based contractility is required for transmitting directional cues between epithelial cells, and contraction occurs at cadherin complexes regardless of substrate stiffness.[3] They observed that inhibition of myosin II with blebbistatin yielded slower collective migration of epithelial cells on stiff substrates, similar to that of cells on soft substrates. Whereas they completely impaired the cell contraction apparatus, we inhibited just one known pathway leading to myosin contraction. Taken together, these findings may suggest that cells on stiff substrates utilize signaling pathways other than Rho/ROCK to compensate for its loss, such as MLC kinase (MLCK). MLCK has been shown to be active at the cell periphery near cell-cell junctions, while Rho/ROCK mediates the cell interior and promotes stress fiber formation.[19] Further work to examine MLCK using its specific inhibitor ML-7 would elucidate this possibility.

Our findings suggest that the balance between forward motion mechanisms, including Rac and Cdc42, require some threshold of substrate stiffness to overcome Rho/ROCK-mediated resistance within the cell bound to neighboring cells. Therefore, the forces generates on stiff substrates at cell-matrix junctions are critical to creating force asymmetry within collectively

migrating cells that experience resistive intercellular forces from neighboring cells. The ability for cells to collectively migrate over and heal a site of injury appears to be dependent on their mechanically-tunable ability to collective propel. Recently, it has been hypothesized that collectively migrating cells are not passively pulled by the leading cells at the interface, but rather, they are actively making their own forward protrusions underneath the tail end of cells in front.[20] Our findings suggest that this hypothesis only holds for cells seeded on substrates of sufficiently high stiffness and that below some stiffness threshold, cells may be simply incapable of generating the propulsive forces necessary to overcome neighbor resistance. This may play a role in acute phase injury healing where thromboses or granulation tissue may be too soft to allow endothelialization or epithelialization.[21]

Finally, my preliminary data show that pro-inflammatory p-selectin expression increased on both soft and stiff substrates. The migratory response to globally-available growth factors did not differ with substrate stiffness. These provide important insights into understanding that faster collective migration may not always be better. It is evident that faster collective migration on stiff substrates leads to decreased togetherness within the migratory front and increased levels of pro-thrombotic and pro-inflammatory activated endothelial cells. Nitric oxide has been shown to prevent p-selectin expression.[22, 23] Decreased levels of eNOS in endothelial cells on stiff substrates due to increased Rho/ROCK signaling may explain why they have increase p-selectin expression.[24] P-selectin has also been shown to increase in response to calcium influx that may occur after Rho/ROCK-mediated dismantling of VE-cadherin complexes.[25] Increased expression of p-selectin on soft substrates was surprising. This could be explained by reduced internalization of p-selectin after stimulation, which has been shown to be stiffness-dependent for other adhesive proteins such as integrins.[26] This future work is critical to fully understanding how stiffness-dependent migration rate impacts the state of endothelial thrombogenicity and immunogenicity.

Endothelial-to-mesenchymal transition (EndMT) has been of recent interest as a clinically-relevant source of fibrosis in disease states, including cancer and heart disease.[27-29] We show preliminary evidence that EndMT increased on soft substrates in response to transforming growth factor-β (TGF-β). This differed from our finding that migratory response to globally-available pro-migratory growth factors did not differ with substrate stiffness. This sensitivity to TGF-β-induced EndMT in endothelial cells on soft substrates suggests that there may be inhibitory cross-talk between integrin activation and the TGF-β receptor that does not occur on soft substrates with decreased integrin clustering and activation. This type of growth factor receptor (GFR)-integrin cross-talk has been shown to occur with other receptors, possibly by integrin signaling controlling the rate of GFR internalization.[30] However, a greater understanding of the dynamic and possibly reversible process of EndMT is required to fully understand its impact in stiffness-dependent collectively migrating endothelial cells.

All together, these data suggest an important role for substrate stiffness in endothelial cell collective migration, which will not only elucidate mechanisms of disease progression, but also inform approaches to vascularization of tissue engineered structures. Based on our findings, substrate stiffness at the extremes induces signaling that is deleterious to collective migration, promoting EndMT and subsequent fibrosis as well as an inflammatory response. Therefore, approaches to treating disease by maintaining physiological tissue stiffnesses may be beneficial. During re-endothelialization after percutaneous intervention, for example, it may be helpful to coat a metallic stent with a compliant substrate with an elastic modulus around 14 kPa to maximize collective migration speed to restore a continuous endothelial lumen layer. Furthermore, developing tissue engineered scaffolds with physiologically-similar mechanical properties may limit the inflammatory response and promote host integration. Our studies will

directly inform one of the greatest challenges to tissue engineering, coaxing host blood vessels to fully integrate large pieces of exogenous tissue with angiogenic ingrowth.

5.2. Specific Discoveries

The purpose of this thesis work was to investigate how substrate stiffness affects the complex process of collective migration in endothelial cells. We have report here findings that support our hypothesis that endothelial cell collective migration is a function of substrate stiffness.

In chapter 2, we introduced robust alternatives to overcome challenges associated with measuring confluent cell shape. We specifically measured nuclear alignment as a measure for cell alignment and approximated cell area using a tessellation approach. Algorithms were made to identify fiber-like structures, such as ECM proteins and F-actin stress fibers, for length and angle quantification. Furthermore, punctate granule-like structures, such as focal adhesions and p-selectin granules, were quantified. Although these methods were purposely tailored for our specific application, their underlying algorithms could be applied to measure a variety of features within confluent cell images. This work in developing transparent, automated computational methods was a necessary first step and allows for increased credibility and conclusive power of subsequent findings.

In chapter 3, we discovered that endothelial cells collectively migrate farther on stiffer substrates. We found that this increased collective migration distance was more directed and less together, and the latter finding led to more proliferation. Furthermore, we discovered that directed migration on stiffer substrates requires α_5 integrin as it was abolished when α_5 integrin was knocked down. We discovered that ROCK-mediated contractility prevents endothelial cells from migrating far on soft substrates. We discovered that although collectively migrating

endothelial cells secrete and remodel an extensive fibronectin network, it was not an essential factor for transducing substrate stiffness cues.

In chapter 4, we discovered that substrate stiffness does affect p-selectin expression and TGF-β-induced EndMT in collectively migrating endothelial cells. We further showed that substrate stiffness does not affect collectively migrating endothelial cells responding to a one-time, globally-available dose of either VEGF or FGF2.

5.3. Contributions to the Field

This is the first work to explore collective endothelial cell migration as a function of substrate stiffness. These findings show compelling evidence suggesting that substrate stiffness affects how endothelial cells collectively migrate, which is important in re-endothelialization after percutaneous intervention and in vascularizing tissue-engineered constructs. Specific contributions to the fields of biomedical engineering, vascular biology, tissue engineering, and the larger scientific community include:

Computational image quantification methods for cells in a confluent monolayer. Although the microscope resolution has greatly advanced in recent years, non-computational scientists continue to struggle with extracting quantitative information from high resolution images. Scientists are therefore less able to make meaningful conclusions based on quantitative feature extraction. It is no longer sufficient to simply show an image and make qualitative assessments. Since manual methods of gathering cellular measurements from confluent monolayers are tedious, time-consuming, and riddled with error and bias, new computational approaches were required.

We introduced robust alternatives to overcome challenges associated with extracting features of confluent cells for measurement. Through this work we hoped to provide clear and

comprehensive explanations of our image quantification methods so that other research groups can fully understand the specific measurements we present. We hoped to inspire all biomedical researchers to do quantitative image analyses to reduce human bias and error, and fully explain their methods transparently to increase conclusive power and increase reproducibility. We have specifically added to the pool of image analysis techniques for measuring two-dimensional cell monolayers.

Endothelial cells collectively migrating as a function of substrate stiffness. For nearly 20 years, substrate stiffness had been known to significantly impact almost every cellular function, including migration, proliferation, survival, differentiation, and sensitivity to extracellular cytokines and growth factors. More recently, the research community has accepted that collective vs. single-cell migration are two separate mechanisms by which cells and tissues move. We show that collective migration occurs in endothelial cells and that this complicated, dynamic process of directed and together individual cells within a larger migrating front is dependent upon substrate stiffness.

These findings have important implications in understanding pathogenesis of vascular re-stenosis after percutaneous intervention and stent placement, where the diseased vessel and stent stiffness are increased. This can be further applied to other disease states with both impaired angiogenesis and changes in tissue stiffness, such as non-healing wounds or tumor angiogenesis. Based on this work, therapeutic approaches to promote re-endothelialization and angiogenesis may require more than just VEGF. Future approaches may look to agents that alter substrate stiffness. This work will also inform approaches to tissue engineering, since vascularization of large tissues has been the greatest limiting factor in clinical application. Designing scaffolds with specific stiffnesses will help promote endothelial collective migration for vascular ingrowth.

Endothelial cell response to external stimuli while collective migrating. Crosstalk between integrins and specific growth factors has been shown in a variety of cell types, suggesting a link between substrate stiffness and the cellular response to exogenous stimuli. Our work led to preliminary evidence that substrate stiffness affects the endothelial response to some exogenous stimuli commonly found in the diseased milieu. Specifically, we discovered that soft and stiff but not intermediate substrates elicited elevated p-selectin expression, suggesting that substrate stiffness alone is enough to alter endothelial propensity to contribute to an inflammatory response. We discovered that more TGF-β-induced endothelial-to-mesenchymal transition (EndMT) occurs more on soft substrates. We also have data that suggests EndMT is reversible transdifferentiation within a migratory front. We discovered that substrate stiffness did not affect the endothelial collective migration response to globally-released pro-migratory growth factors VEGF and FGF2.

5.4. Future Work

5.4.1. Evaluate the Importance of Other Cell Contractility Pathways and the $\alpha_V\beta_3$ Integrin in Stiffness-Dependent Endothelial Cell Collective Migration

We investigated how ROCK, fibronectin, and $\alpha_5\beta_1$ integrin are involved in stiffness-dependent collective migration. In order to more fully understand the role of cellular contractility in stiffness-dependent collective migration, blebbistatin, C3 transferase, and EHT 1864 should be used to inhibit myosin II contraction, RhoA activation, and Rac1 activation, respectively. Previous studies show that the $\alpha_V\beta_3$ integrin, another prominent fibronectin receptor, is important for mechanotransduction in migrating cells.[97] Using similar siRNA techniques, the α_V integrin subunit could be knocked down during a cage migration assay.

5.4.2. Investigate Mechanisms Underlying Stiffness-Dependent Expression of P-Selectin

We report preliminary data suggesting that p-selectin is expressed more on soft and stiff, but not intermediate substrates. This intriguing finding could have great implications in vascular disease progression as chronically activated endothelial cells in atherosclerosis may perpetuate a futile inflammatory response in a feed-forward fashion. This observation was seen at only 24 hours, so future studies should include time course experiments to differentiate between an acute and chronic p-selectin response. Tumor necrosis factor α (TNF-α), a cytokine known to elicit p-selectin expression in endothelial cells, can be used as a positive control. Differences in endothelial nitric oxide synthase (eNOS) and nitric oxide (NO) levels as functions of substrate stiffness should be measured as they have been shown to prevent p-selectin expression.[148]

5.4.3. Investigate Mechanisms Underlying Stiffness-Dependent Endothelial-to-Mesenchymal Transition (EndMT)

We report preliminary data suggesting that TGF-β2-induced EndMT occurs more on soft substrates. This intriguing finding suggests antagonistic cross-talk between the integrin and TGF-β receptor signaling pathways. Determining the stiffness-dependency of TGF-β2-induced EndMT would be of high interest as it could contribute to deleterious fibrosis in chronic disease progression. EndMT is a dynamic process that may be completely reversible if endothelial cells are unable to full migrate away from the confluent monolayer. Future studies should account for this, possibly by utilizing porous three-dimensional scaffolds with tunable mechanical properties. PP2, a specific Src inhibitor, could be used to determine if elevated FAK/Src signaling on stiff substrates affects TGF-β2-induced EndMT.

5.4.4. Explore the Impact of Stiffness-Dependent Collective Migration in Three-Dimensional Models and Models Under Physiologic Flow Conditions

Although our model was sufficient to study re-endothelialization as a quasi-two-dimensional process, it would be interesting to study this pathology more specifically by adding metal stent material to the culture conditions. It would be also interesting to learn how substrate stiffness affects endothelial cell collective migration in a three-dimensional scaffold to expand understanding of migration for angiogenesis in various diseases. This would be a more useful model for studying angiogenesis and vascularization for tissue-engineered applications. Recently, phototuning has been used to dynamically alter the stiffness of three-dimensional alginate.[174]

5.4.5. Explore the Impact of Stiffness-Dependent Collective Migration in Animal Models

In order to establish clinical relevance, our *in vitro* findings need to be validated in animal models. A simple approach would be to extract the aorta from young and old mice with presumably soft and stiffer underlying ECM, respectively, and perform an *ex vivo* scratch migration assay. In this experiment, the endothelial lining of explanted aorta would be damaged by a needle prior to incubation and imaging of the wound. Atomic force microscopy would need to be performed on the explants to verify differences in substrate stiffness.

List of References

1. Mozaffarian, D. et al. Heart disease and stroke statistics--2015 update: a report from the American Heart Association. *Circulation* **131**, e29-322 (2015).
2. Farooq, V., Gogas, B.D. & Serruys, P.W. Restenosis: delineating the numerous causes of drug-eluting stent restenosis. *Circulation. Cardiovascular interventions* **4**, 195-205 (2011).
3. Teirstein, P.S. Drug-eluting stent restenosis: an uncommon yet pervasive problem. *Circulation* **122**, 5-7 (2010).
4. Kiemeneij, F. et al. Continued benefit of coronary stenting versus balloon angioplasty: five-year clinical follow-up of Benestent-I trial. *Journal of the American College of Cardiology* **37**, 1598-1603 (2001).
5. Canver, C.C. Conduit options in coronary artery bypass surgery. *Chest* **108**, 1150-1155 (1995).
6. Daneshmand, M.A., Keller, R.S., Canver, M.C., Canver, A.C. & Canver, C.C. Histamine H1 and H2 receptor-mediated vasoreactivity of human internal thoracic and radial arteries. *Surgery* **136**, 458-463 (2004).
7. Malenka, D.J. et al. Comparing long-term survival of patients with multivessel coronary disease after CABG or PCI: analysis of BARI-like patients in northern New England. *Circulation* **112**, I371-376 (2005).
8. van Beusekom, H.M. et al. Long-term endothelial dysfunction is more pronounced after stenting than after balloon angioplasty in porcine coronary arteries. *Journal of the American College of Cardiology* **32**, 1109-1117 (1998).
9. Losordo, D.W., Isner, J.M. & Diaz-Sandoval, L.J. Endothelial recovery: the next target in restenosis prevention. *Circulation* **107**, 2635-2637 (2003).
10. McGill, H.C. et al. Origin of atherosclerosis in childhood and adolescence. *Am J Clin Nutr* **72**, 1307s-1315s (2000).
11. Guyenet, P.G. The sympathetic control of blood pressure. *Nat Rev Neurosci* **7**, 335-346 (2006).
12. Umans, J.G. & Levi, R. Nitric-Oxide in the Regulation of Blood-Flow and Arterial-Pressure. *Annual review of physiology* **57**, 771-790 (1995).
13. Cooke, J.P. & Dzau, V.J. Nitric oxide synthase: Role in the genesis of vascular disease. *Annual review of medicine* **48**, 489-509 (1997).
14. Uematsu, M. et al. Regulation of endothelial cell nitric oxide synthase mRNA expression by shear stress. *Am J Physiol-Cell Ph* **269**, C1371-C1378 (1995).
15. Corson, M.A. et al. Phosphorylation of endothelial nitric oxide synthase in response to fluid shear stress. *Circulation research* **79**, 984-991 (1996).
16. Kiowski, W. et al. Evidence for Endothelin-1-Mediated Vasoconstriction in Severe Chronic Heart-Failure. *Lancet* **346**, 732-736 (1995).
17. Dejana, E., Orsenigo, F. & Lampugnani, M.G. The role of adherens junctions and VE-cadherin in the control of vascular permeability. *Journal of cell science* **121**, 2115-2122 (2008).

18. Muller, W.A. Leukocyte-endothelial-cell interactions in leukocyte transmigration and the inflammatory response. *Trends Immunol* **24**, 327-334 (2003).

19. Mackman, N., Tilley, R.E. & Key, N.S. Role of the extrinsic pathway of blood coagulation in hemostasis and thrombosis. *Arterioscl Throm Vas* **27**, 1687-1693 (2007).

20. van Hinsbergh, V.W.M. The endothelium: vascular control of haemostasis. *Eur J Obstet Gyn R B* **95**, 198-201 (2001).

21. Vallet, B. & Wiel, E. Endothelial cell dysfunction and coagulation. *Crit Care Med* **29**, S36-S41 (2001).

22. Knipe, L. et al. A revised model for the secretion of tPA and cytokines from cultured endothelial cells. *Blood* **116**, 2183-2191 (2010).

23. Isner, J.M. & Asahara, T. Angiogenesis and vasculogenesis as therapeutic strategies for postnatal neovascularization. *Journal of Clinical Investigation* **103**, 1231-1236 (1999).

24. Carmeliet, P. Mechanisms of angiogenesis and arteriogenesis. *Nature medicine* **6**, 389-395 (2000).

25. Dejana, E. Endothelial cell-cell junctions: happy together. *Nature reviews. Molecular cell biology* **5**, 261-270 (2004).

26. Wallez, Y. & Huber, P. Endothelial adherens and tight junctions in vascular homeostasis, inflammation and angiogenesis. *Biochimica et biophysica acta* **1778**, 794-809 (2008).

27. Nelson, C.M. & Chen, C.S. VE-cadherin simultaneously stimulates and inhibits cell proliferation by altering cytoskeletal structure and tension. *Journal of cell science* **116**, 3571-3581 (2003).

28. Nelson, W.J. & Nusse, R. Convergence of Wnt, beta-catenin, and cadherin pathways. *Science* **303**, 1483-1487 (2004).

29. Cara J. Gottardi, B.M.G. Adhesion signaling How beta-catenin interacts with its partners. *Current Biology* **11**, R792-794 (2001).

30. Masckauchan, T.N., Shawber, C.J., Funahashi, Y., Li, C.M. & Kitajewski, J. Wnt/beta-catenin signaling induces proliferation, survival and interleukin-8 in human endothelial cells. *Angiogenesis* **8**, 43-51 (2005).

31. Nelson, W.J. Regulation of cell-cell adhesion by the cadherin-catenin complex. *Biochemical Society transactions* **36**, 149-155 (2008).

32. Broussard, J.A., Webb, D.J. & Kaverina, I. Asymmetric focal adhesion disassembly in motile cells. *Current opinion in cell biology* **20**, 85-90 (2008).

33. Schober, M. et al. Focal adhesion kinase modulates tension signaling to control actin and focal adhesion dynamics. *The Journal of cell biology* **176**, 667-680 (2007).

34. Braren, R. et al. Endothelial FAK is essential for vascular network stability, cell survival, and lamellipodial formation. *The Journal of cell biology* **172**, 151-162 (2006).

35. Friedl, P. & Gilmour, D. Collective cell migration in morphogenesis, regeneration and cancer. *Nature reviews. Molecular cell biology* **10**, 445-457 (2009).

36. Rorth, P. Collective cell migration. *Annual review of cell and developmental biology* **25**, 407-429 (2009).

37. Rorth, P. Fellow travellers: emergent properties of collective cell migration. *EMBO reports* **13**, 984-991 (2012).

38. Lee, J.M., Dedhar, S., Kalluri, R. & Thompson, E.W. The epithelial-mesenchymal transition: new insights in signaling, development, and disease. *The Journal of cell biology* **172**, 973-981 (2006).

39. Gerhardt, H. et al. VEGF guides angiogenic sprouting utilizing endothelial tip cell filopodia. *The Journal of cell biology* **161**, 1163-1177 (2003).

40. Phng, L.K. & Gerhardt, H. Angiogenesis: a team effort coordinated by notch. *Developmental cell* **16**, 196-208 (2009).

41. Jakobsson, L. et al. Endothelial cells dynamically compete for the tip cell position during angiogenic sprouting. *Nature cell biology* **12**, 943-953 (2010).

42. Geudens, I. & Gerhardt, H. Coordinating cell behaviour during blood vessel formation. *Development* **138**, 4569-4583 (2011).

43. Blanco, R. & Gerhardt, H. VEGF and Notch in tip and stalk cell selection. *Cold Spring Harbor perspectives in medicine* **3**, a006569 (2013).

44. Hellstrom, M. et al. Dll4 signalling through Notch1 regulates formation of tip cells during angiogenesis. *Nature* **445**, 776-780 (2007).

45. Stenzel, D. et al. Endothelial basement membrane limits tip cell formation by inducing Dll4/Notch signalling in vivo. *EMBO reports* **12**, 1135-1143 (2011).

46. Bindschadler, M. & McGrath, J.L. Sheet migration by wounded monolayers as an emergent property of single-cell dynamics. *Journal of cell science* **120**, 876-884 (2007).

47. Farooqui, R. & Fenteany, G. Multiple rows of cells behind an epithelial wound edge extend cryptic lamellipodia to collectively drive cell-sheet movement. *Journal of cell science* **118**, 51-63 (2005).

48. Ng, M.R., Besser, A., Danuser, G. & Brugge, J.S. Substrate stiffness regulates cadherin-dependent collective migration through myosin-II contractility. *The Journal of cell biology* **199**, 545-563 (2012).

49. Wegener, K.L. & Campbell, I.D. Transmembrane and cytoplasmic domains in integrin activation and protein-protein interactions (review). *Molecular membrane biology* **25**, 376-387 (2008).

50. Giancotti, F.G. & Ruoslahti, E. Integrin signaling. *Science* **285**, 1028-1032 (1999).

51. Zaidel-Bar, R., Ballestrem, C., Kam, Z. & Geiger, B. Early molecular events in the assembly of matrix adhesions at the leading edge of migrating cells. *Journal of cell science* **116**, 4605-4613 (2003).

52. Hytonen, V.P. & Vogel, V. How force might activate talin's vinculin binding sites: SMD reveals a structural mechanism. *PLoS computational biology* **4**, e24 (2008).

53. Vicente-Manzanares, M., Choi, C.K. & Horwitz, A.R. Integrins in cell migration--the actin connection. *Journal of cell science* **122**, 199-206 (2009).

54. Mitra, S.K. & Schlaepfer, D.D. Integrin-regulated FAK-Src signaling in normal and cancer cells. *Current opinion in cell biology* **18**, 516-523 (2006).

55. Schlaepfer, D.D., Mitra, S.K. & Ilic, D. Control of motile and invasive cell phenotypes by focal adhesion kinase. *Biochimica et biophysica acta* **1692**, 77-102 (2004).

56. Hu, B. et al. Angiopoietin 2 induces glioma cell invasion by stimulating matrix metalloprotease 2 expression through the alphavbeta1 integrin and focal adhesion kinase signaling pathway. *Cancer research* **66**, 775-783 (2006).

57. Huveneers, S. & Danen, E.H. Adhesion signaling - crosstalk between integrins, Src and Rho. *Journal of cell science* **122**, 1059-1069 (2009).

58. Webb, D.J. et al. FAK-Src signalling through paxillin, ERK and MLCK regulates adhesion disassembly. *Nature cell biology* **6**, 154-161 (2004).

59. Shen, Q., Rigor, R.R., Pivetti, C.D., Wu, M.H. & Yuan, S.Y. Myosin light chain kinase in microvascular endothelial barrier function. *Cardiovascular research* **87**, 272-280 (2010).

60. Amano, M. et al. Formation of actin stress fibers and focal adhesions enhanced by Rho-kinase. *Science* **275**, 1308-1311 (1997).

61. Levental, I., Georges, P.C., Janmey P.A. Soft biological materials and their impact on cell function. *Soft matter* **3**, 299-306 (2007).

62. Kawasaki, T., Sasayama, S., Yagi, S., Asakawa, T. & Hirai, T. Noninvasive Assessment of the Age-Related-Changes in Stiffness of Major Branches of the Human Arteries. *Cardiovascular research* **21**, 678-687 (1987).

63. Benetos, A. et al. Influence of age, risk factors, and cardiovascular and renal disease on arterial stiffness: Clinical applications. *Am J Hypertens* **15**, 1101-1108 (2002).

64. Pelham, R.J., Jr. & Wang, Y. Cell locomotion and focal adhesions are regulated by substrate flexibility. *Proceedings of the National Academy of Sciences of the United States of America* **94**, 13661-13665 (1997).

65. Tse, J.R. & Engler, A.J. Preparation of hydrogel substrates with tunable mechanical properties. *Current protocols in cell biology / editorial board, Juan S. Bonifacino ... [et al.]* **Chapter 10**, Unit 10 16 (2010).

66. Bhana, B. et al. Influence of substrate stiffness on the phenotype of heart cells. *Biotechnology and bioengineering* **105**, 1148-1160 (2010).

67. Discher, D.E., Janmey, P. & Wang, Y.L. Tissue cells feel and respond to the stiffness of their substrate. *Science* **310**, 1139-1143 (2005).

68. Janmey, P.A. & Weitz, D.A. Dealing with mechanics: mechanisms of force transduction in cells. *Trends in biochemical sciences* **29**, 364-370 (2004).

69. Janmey, P.A., Winer, J.P., Murray, M.E. & Wen, Q. The hard life of soft cells. *Cell motility and the cytoskeleton* **66**, 597-605 (2009).

70. Chen, C.S., Mrksich, M., Huang, S., Whitesides, G.M. & Ingber, D.E. Geometric control of cell life and death. *Science* **276**, 1425-1428 (1997).

71. Yeung, T. et al. Effects of substrate stiffness on cell morphology, cytoskeletal structure, and adhesion. *Cell motility and the cytoskeleton* **60**, 24-34 (2005).

72. Solon, J., Levental, I., Sengupta, K., Georges, P.C. & Janmey, P.A. Fibroblast adaptation and stiffness matching to soft elastic substrates. *Biophysical journal* **93**, 4453-4461 (2007).

73. Leipzig, N.D. & Shoichet, M.S. The effect of substrate stiffness on adult neural stem cell behavior. *Biomaterials* **30**, 6867-6878 (2009).

74. Olsen, A.L. et al. Hepatic stellate cells require a stiff environment for myofibroblastic differentiation. *American journal of physiology. Gastrointestinal and liver physiology* **301**, G110-118 (2011).

75. Birukova, A.A. et al. Endothelial barrier disruption and recovery is controlled by substrate stiffness. *Microvascular research* **87**, 50-57 (2013).

76. Kim, J.H., Dooling, L.J. & Asthagiri, A.R. Intercellular mechanotransduction during multicellular morphodynamics. *Journal of the Royal Society, Interface / the Royal Society* **7 Suppl 3**, S341-350 (2010).

77. Trepat X, W.M., Angelini TE, Millet Emil, Weitz DA, Butler JP, Fredberg JJ Physical forces during collective cell migration. *Nature Physics* **5**, 426-430 (2009).

78. Liu, Z. et al. Mechanical tugging force regulates the size of cell-cell junctions. *Proceedings of the National Academy of Sciences of the United States of America* **107**, 9944-9949 (2010).

79. Dembo, M. & Wang, Y.L. Stresses at the cell-to-substrate interface during locomotion of fibroblasts. *Biophysical journal* **76**, 2307-2316 (1999).

80. Lo, C.M., Wang, H.B., Dembo, M. & Wang, Y.L. Cell movement is guided by the rigidity of the substrate. *Biophysical journal* **79**, 144-152 (2000).

81. Tambe, D.T. et al. Collective cell guidance by cooperative intercellular forces. *Nature materials* **10**, 469-475 (2011).

82. Trepat, X. & Fredberg, J.J. Plithotaxis and emergent dynamics in collective cellular migration. *Trends in cell biology* **21**, 638-646 (2011).

83. Trepat, X., Chen, Z. & Jacobson, K. Cell migration. *Comprehensive Physiology* **2**, 2369-2392 (2012).

84. Ilina, O. & Friedl, P. Mechanisms of collective cell migration at a glance. *Journal of cell science* **122**, 3203-3208 (2009).

85. Londono, C. et al. Nonautonomous contact guidance signaling during collective cell migration. *Proceedings of the National Academy of Sciences of the United States of America* **111**, 1807-1812 (2014).

86. Provenzano, P.P., Inman, D.R., Eliceiri, K.W., Trier, S.M. & Keely, P.J. Contact guidance mediated three-dimensional cell migration is regulated by Rho/ROCK-dependent matrix reorganization. *Biophysical journal* **95**, 5374-5384 (2008).

87. Lee, P., Lin, R., Moon, J. & Lee, L.P. Microfluidic alignment of collagen fibers for in vitro cell culture. *Biomedical microdevices* **8**, 35-41 (2006).

88. Kim, D.H. et al. Mechanosensitivity of fibroblast cell shape and movement to anisotropic substratum topography gradients. *Biomaterials* **30**, 5433-5444 (2009).

89. Jaffe, E.A. & Mosher, D.F. Synthesis of fibronectin by cultured human endothelial cells. *The Journal of experimental medicine* **147**, 1779-1791 (1978).

90. Clark, R.A. et al. Fibronectin and fibrin provide a provisional matrix for epidermal cell migration during wound reepithelialization. *The Journal of investigative dermatology* **79**, 264-269 (1982).

91. Clark, R.A. et al. Blood vessel fibronectin increases in conjunction with endothelial cell proliferation and capillary ingrowth during wound healing. *The Journal of investigative dermatology* **79**, 269-276 (1982).

92. Stupack, D.G. & Cheresh, D.A. ECM remodeling regulates angiogenesis: endothelial integrins look for new ligands. *Science's STKE : signal transduction knowledge environment* **2002**, pe7 (2002).

93. Mosher, D.F., Fogerty, F.J., Chernousov, M.A. & Barry, E.L. Assembly of fibronectin into extracellular matrix. *Annals of the New York Academy of Sciences* **614**, 167-180 (1991).

94. Singh, P., Carraher, C. & Schwarzbauer, J.E. Assembly of fibronectin extracellular matrix. *Annual review of cell and developmental biology* **26**, 397-419 (2010).

95. Magnusson, M.K. & Mosher, D.F. Fibronectin: structure, assembly, and cardiovascular implications. *Arteriosclerosis, thrombosis, and vascular biology* **18**, 1363-1370 (1998).

96. Friedland, J.C., Lee, M.H. & Boettiger, D. Mechanically activated integrin switch controls alpha5beta1 function. *Science* **323**, 642-644 (2009).

97. Roca-Cusachs, P., Gauthier, N.C., Del Rio, A. & Sheetz, M.P. Clustering of alpha(5)beta(1) integrins determines adhesion strength whereas alpha(v)beta(3) and talin enable mechanotransduction. *Proceedings of the National Academy of Sciences of the United States of America* **106**, 16245-16250 (2009).

98. Woods, A.J., White, D.P., Caswell, P.T. & Norman, J.C. PKD1/PKCmu promotes alphavbeta3 integrin recycling and delivery to nascent focal adhesions. *The EMBO journal* **23**, 2531-2543 (2004).

99. Smith, M.L. et al. Force-induced unfolding of fibronectin in the extracellular matrix of living cells. *PLoS biology* **5**, e268 (2007).

100. Legant, W.R., Chen, C.S. & Vogel, V. Force-induced fibronectin assembly and matrix remodeling in a 3D microtissue model of tissue morphogenesis. *Integrative biology : quantitative biosciences from nano to macro* **4**, 1164-1174 (2012).

101. Klotzsch, E. et al. Fibronectin forms the most extensible biological fibers displaying switchable force-exposed cryptic binding sites. *Proceedings of the National Academy of Sciences of the United States of America* **106**, 18267-18272 (2009).

102. Little, W.C., Smith, M.L., Ebneter, U. & Vogel, V. Assay to mechanically tune and optically probe fibrillar fibronectin conformations from fully relaxed to breakage. *Matrix biology : journal of the International Society for Matrix Biology* **27**, 451-461 (2008).

103. Leiss, M., Beckmann, K., Giros, A., Costell, M. & Fassler, R. The role of integrin binding sites in fibronectin matrix assembly in vivo. *Current opinion in cell biology* **20**, 502-507 (2008).

104. Halliday, N.L. & Tomasek, J.J. Mechanical properties of the extracellular matrix influence fibronectin fibril assembly in vitro. *Experimental cell research* **217**, 109-117 (1995).

105. Ohashi, T., Kiehart, D.P. & Erickson, H.P. Dual labeling of the fibronectin matrix and actin cytoskeleton with green fluorescent protein variants. *Journal of cell science* **115**, 1221-1229 (2002).

106. Bosman, F.T. & Stamenkovic, I. Functional structure and composition of the extracellular matrix. *The Journal of pathology* **200**, 423-428 (2003).

107. Cardona, A. & Tomancak, P. Current challenges in open-source bioimage informatics. *Nature methods* **9**, 661-665 (2012).

108. Lee, R.M., Kelley, D.H., Nordstrom, K.N., Ouellette, N.T. & Losert, W. Quantifying stretching and rearrangement in epithelial sheet migration. *New journal of physics* **15** (2013).

109. Coomber, B.L. & Gotlieb, A.I. In vitro endothelial wound repair. Interaction of cell migration and proliferation. *Arteriosclerosis* **10**, 215-222 (1990).

110. Dolle, J.P., Rezvan, A., Allen, F.D., Lazarovici, P. & Lelkes, P.I. Nerve growth factor-induced migration of endothelial cells. *The Journal of pharmacology and experimental therapeutics* **315**, 1220-1227 (2005).

111. Dixit, P., Hern-Anderson, D., Ranieri, J. & Schmidt, C.E. Vascular graft endothelialization: comparative analysis of canine and human endothelial cell migration on natural biomaterials. *Journal of biomedical materials research* **56**, 545-555 (2001).

112. Stelzer, E.H.K. Contrast, resolution, pixelation, dynamic range and signal-to-noise ratio: fundamental limits to resolution in fluorescence light microscopy. *J Microsc-Oxford* **189**, 15-24 (1998).

113. Otsu, N. A threshold selection method from gray-level histograms. *IEEE Transactions on Systems, Man, and Cybernetics* **9**, 62-66 (1979).

114. Michel, R., Steinmeyer, R., Falk, M. & Harms, G.S. A new detection algorithm for image analysis of single, fluorescence-labeled proteins in living cells. *Microscopy research and technique* **70**, 763-770 (2007).

115. Khalil, A.A. & Friedl, P. Determinants of leader cells in collective cell migration. *Integrative biology : quantitative biosciences from nano to macro* **2**, 568-574 (2010).

116. Friedl, P., Wolf, K. & Lammerding, J. Nuclear mechanics during cell migration. *Current opinion in cell biology* **23**, 55-64 (2011).

117. Levy, J.R. & Holzbaur, E.L. Dynein drives nuclear rotation during forward progression of motile fibroblasts. *Journal of cell science* **121**, 3187-3195 (2008).

118. Orsulic, S., Huber, O., Aberle, H., Arnold, S. & Kemler, R. E-cadherin binding prevents beta-catenin nuclear localization and beta-catenin/LEF-1-mediated transactivation. *Journal of cell science* **112 (Pt 8)**, 1237-1245 (1999).

119. Aurenhammer, F. Voronoi diagrams -- A survey of a fundamental geometric data structure. *ACM Coputing Surveys* **23**, 345-405 (1991).

120. Duyckaerts, C. & Godefroy, G. Voronoi tessellation to study the numerical density and the spatial distribution of neurones. *Journal of chemical neuroanatomy* **20**, 83-92 (2000).

121. Cavalcanti-Adam, E.A. et al. Cell spreading and focal adhesion dynamics are regulated by spacing of integrin ligands. *Biophysical journal* **92**, 2964-2974 (2007).

122. Lacayo, C.I. et al. Emergence of large-scale cell morphology and movement from local actin filament growth dynamics. *PLoS biology* **5**, e233 (2007).

123. Klein, E.A. et al. Cell-cycle control by physiological matrix elasticity and in vivo tissue stiffening. *Current biology : CB* **19**, 1511-1518 (2009).

124. Lamalice, L., Le Boeuf, F. & Huot, J. Endothelial cell migration during angiogenesis. *Circulation research* **100**, 782-794 (2007).

125. Mitchison, T.J. & Cramer, L.P. Actin-based cell motility and cell locomotion. *Cell* **84**, 371-379 (1996).

126. Pankov, R. et al. A Rac switch regulates random versus directionally persistent cell migration. *The Journal of cell biology* **170**, 793-802 (2005).

127. Totsukawa, G. et al. Distinct roles of MLCK and ROCK in the regulation of membrane protrusions and focal adhesion dynamics during cell migration of fibroblasts. *The Journal of cell biology* **164**, 427-439 (2004).

128. Worthylake, R.A. & Burridge, K. RhoA and ROCK promote migration by limiting membrane protrusions. *Journal of Biological Chemistry* **278**, 13578-13584 (2003).

129. Mitra, S.K., Hanson, D.A. & Schlaepfer, D.D. Focal adhesion kinase: In command and control of cell motility. *Nat Rev Mol Cell Bio* **6**, 56-68 (2005).

130. Friedl, P. & Wolf, K. Plasticity of cell migration: a multiscale tuning model. *The Journal of cell biology* **188**, 11-19 (2010).

131. Dzamba, B.J., Jakab, K.R., Marsden, M., Schwartz, M.A. & DeSimone, D.W. Cadherin adhesion, tissue tension, and noncanonical Wnt signaling regulate fibronectin matrix organization. *Developmental cell* **16**, 421-432 (2009).

132. Li, F., Redick, S.D., Erickson, H.P. & Moy, V.T. Force measurements of the alpha5beta1 integrin-fibronectin interaction. *Biophysical journal* **84**, 1252-1262 (2003).

133. Hsia, D.A. et al. Differential regulation of cell motility and invasion by FAK. *The Journal of cell biology* **160**, 753-767 (2003).

134. Hood, J.D. & Cheresh, D.A. Role of integrins in cell invasion and migration. *Nature reviews. Cancer* **2**, 91-100 (2002).

135. Sanz-Moreno, V. et al. Rac activation and inactivation control plasticity of tumor cell movement. *Cell* **135**, 510-523 (2008).

136. Riento, K. & Ridley, A.J. Rocks: multifunctional kinases in cell behaviour. *Nature reviews. Molecular cell biology* **4**, 446-456 (2003).

137. Zamir, E. et al. Dynamics and segregation of cell-matrix adhesions in cultured fibroblasts. *Nature cell biology* **2**, 191-196 (2000).

138. van der Flier, A. & Sonnenberg, A. Function and interactions of integrins. *Cell and tissue research* **305**, 285-298 (2001).

139. Yang, J.T. & Hynes, R.O. Fibronectin receptor functions in embryonic cells deficient in alpha 5 beta 1 integrin can be replaced by alpha V integrins. *Molecular biology of the cell* **7**, 1737-1748 (1996).

140. Mettouchi, A. et al. Integrin-specific activation of Rac controls progression through the G(1) phase of the cell cycle. *Molecular cell* **8**, 115-127 (2001).

141. Guo, W.H. & Wang, Y.L. A three-component mechanism for fibroblast migration with a contractile cell body that couples a myosin II-independent propulsive anterior to a myosin II-dependent resistive tail. *Molecular biology of the cell* **23**, 1657-1663 (2012).

142. Chang, S.S., Guo, W.H., Kim, Y. & Wang, Y.L. Guidance of cell migration by substrate dimension. *Biophysical journal* **104**, 313-321 (2013).

143. Potenta, S., Zeisberg, E. & Kalluri, R. The role of endothelial-to-mesenchymal transition in cancer progression. *British journal of cancer* **99**, 1375-1379 (2008).

144. Beavon, I.R.G. The E-cadherin-catenin complex in tumour metastasis: structure, function and regulation. *Eur J Cancer* **36**, 1607-1620 (2000).

145. Osei-Owusu, P. et al. Altered reactivity of resistance vasculature contributes to hypertension in elastin insufficiency. *American journal of physiology. Heart and circulatory physiology* **306**, H654-666 (2014).

146. Brown, X.Q. et al. Effect of substrate stiffness and PDGF on the behavior of vascular smooth muscle cells: implications for atherosclerosis. *Journal of cellular physiology* **225**, 115-122 (2010).

147. Friedlander, M. et al. Definition of 2 Angiogenic Pathways by Distinct Alpha(V) Integrins. *Science* **270**, 1500-1502 (1995).

148. Armstead, V.E. et al. Regulation of P-selectin expression in human endothelial cells by nitric oxide. *The American journal of physiology* **273**, H740-746 (1997).

149. Takano, M. et al. Rapid upregulation of endothelial P-selectin expression via reactive oxygen species generation. *American journal of physiology. Heart and circulatory physiology* **283**, H2054-2061 (2002).

150. Petri, B. & Bixel, M.G. Molecular events during leukocyte diapedesis. *The FEBS journal* **273**, 4399-4407 (2006).

151. Konstantopoulos, K., Kukreti, S. & McIntire, L.V. Biomechanics of cell interactions in shear fields. *Advanced drug delivery reviews* **33**, 141-164 (1998).

152. Collins, R.G. et al. P-selectin or intercellular adhesion molecule (ICAM)-1 deficiency substantially protects against atherosclerosis in apolipoprotein E-deficient mice. *Journal of Experimental Medicine* **191**, 189-194 (2000).

153. Zieman, S.J., Melenovsky, V. & Kass, D.A. Mechanisms, pathophysiology, and therapy of arterial stiffness. *Arterioscl Throm Vas* **25**, 932-943 (2005).

154. Yu, W. et al. The endothelial-mesenchymal transition (EndMT) and tissue regeneration. *Current stem cell research & therapy* **9**, 196-204 (2014).

155. Mai, J. et al. Dyssynchronous pacing triggers endothelial-mesenchymal transition through heterogeneity of mechanical stretch in a canine model. *Circulation journal : official journal of the Japanese Circulation Society* **79**, 201-209 (2015).

156. Potenta, S., Zeisberg, E. & Kalluri, R. The role of endothelial-to-mesenchymal transition in cancer progression. *British journal of cancer* **99**, 1375-1379 (2008).

157. Cooley, B.C. et al. TGF-beta signaling mediates endothelial-to-mesenchymal transition (EndMT) during vein graft remodeling. *Science translational medicine* **6**, 227ra234 (2014).

158. Park, J.S. et al. The effect of matrix stiffness on the differentiation of mesenchymal stem cells in response to TGF-beta. *Biomaterials* **32**, 3921-3930 (2011).

159. Turner, N. & Grose, R. Fibroblast growth factor signalling: from development to cancer. *Nature reviews. Cancer* **10**, 116-129 (2010).

160. Ivaska, J. & Heino, J. Cooperation between integrins and growth factor receptors in signaling and endocytosis. *Annual review of cell and developmental biology* **27**, 291-320 (2011).

161. Moro, L. et al. Integrin-induced epidermal growth factor (EGF) receptor activation requires c-Src and p130Cas and leads to phosphorylation of specific EGF receptor tyrosines. *The Journal of biological chemistry* **277**, 9405-9414 (2002).

162. Moro, L. et al. Integrins induce activation of EGF receptor: role in MAP kinase induction and adhesion-dependent cell survival. *The EMBO journal* **17**, 6622-6632 (1998).

163. Schneller, M., Vuori, K. & Ruoslahti, E. Alphavbeta3 integrin associates with activated insulin and PDGFbeta receptors and potentiates the biological activity of PDGF. *The EMBO journal* **16**, 5600-5607 (1997).

164. Sahni, A. & Francis, C.W. Stimulation of endothelial cell proliferation by FGF-2 in the presence of fibrinogen requires alphavbeta3. *Blood* **104**, 3635-3641 (2004).

165. Wang, H.B., Dembo, M. & Wang, Y.L. Substrate flexibility regulates growth and apoptosis of normal but not transformed cells. *American journal of physiology. Cell physiology* **279**, C1345-1350 (2000).

166. Ulrich, T.A., de Juan Pardo, E.M. & Kumar, S. The mechanical rigidity of the extracellular matrix regulates the structure, motility, and proliferation of glioma cells. *Cancer research* **69**, 4167-4174 (2009).

167. Saunders, R.L. & Hammer, D.A. Assembly of Human Umbilical Vein Endothelial Cells on Compliant Hydrogels. *Cellular and molecular bioengineering* **3**, 60-67 (2010).

168. Gray, D.S., Tien, J. & Chen, C.S. Repositioning of cells by mechanotaxis on surfaces with micropatterned Young's modulus. *Journal of biomedical materials research. Part A* **66**, 605-614 (2003).

169. Tonnesen, M.G., Feng, X. & Clark, R.A. Angiogenesis in wound healing. *The journal of investigative dermatology. Symposium proceedings / the Society for Investigative Dermatology, Inc. [and] European Society for Dermatological Research* **5**, 40-46 (2000).

170. Ming, X.F. et al. Rho GTPase/Rho kinase negatively regulates endothelial nitric oxide synthase phosphorylation through the inhibition of protein kinase B/Akt in human endothelial cells. *Molecular and cellular biology* **22**, 8467-8477 (2002).

171. Kohn, J.C. et al. Cooperative effects of matrix stiffness and fluid shear stress on endothelial cell behavior. *Biophysical journal* **108**, 471-478 (2015).

172. Cicchini, C. et al. TGFbeta-induced EMT requires focal adhesion kinase (FAK) signaling. *Experimental cell research* **314**, 143-152 (2008).

173. Leight, J.L., Wozniak, M.A., Chen, S., Lynch, M.L. & Chen, C.S. Matrix rigidity regulates a switch between TGF-beta1-induced apoptosis and epithelial-mesenchymal transition. *Molecular biology of the cell* **23**, 781-791 (2012).

174. Stowers, R.S., Allen, S.C. & Suggs, L.J. Dynamic phototuning of 3D hydrogel stiffness. *Proceedings of the National Academy of Sciences of the United States of America* **112**, 1953-1958 (2015).

Appendix

A. Custom MATLAB Scripts and Functions

```
function [image,background] = gaussFilter(im,iterations,HSIZE,SIGMA)

switch nargin
    case 1
        iterations = 50;
        HSIZE = [5 5];
        SIGMA = 0.75;
    case 2
        HSIZE = [5 5];
        SIGMA = 0.75;
    case 3
        SIGMA = 0.75;
    otherwise
end

background = im;
for i=1:1:iterations
    lowPassFilter = fspecial('gaussian',HSIZE,SIGMA);
    background = imfilter(background,lowPassFilter,'replicate');
end

image = im - background;
```

```
function [image] = medianFilter(im,iterations,nhood)

switch nargin
    case 1
        iterations = 1;
        nhood = [3 3];
    case 2
        nhood = [3 3];
    otherwise
end

image = im;
for i = 1:iterations
    image = medfilt2(image,nhood);
end
```

Vita

Adam Charles Canver
325 N. 15th Street, Apt. 1409 • Philadelphia, PA 19102
acanver@gmail.com

EDUCATION

Drexel University College of Medicine, Philadelphia, PA 2009-present *(expected 2017)*

MD USMLE Step 1 – Pass, June 2011

PhD Biomedical Engineering, June 2015

Advisor: Alisa Morss Clyne, PhD

Johns Hopkins University, Baltimore, MD 2005-2009

BS Biomedical Engineering, Computer Science; Minor: Psychology

RESEARCH EXPERIENCE

PhD Candidate

Advisor: Alisa Morss Clyne, PhD, Cardiovascular Biomechanics Lab 2011-2015
Dept. of Mechanical Engineering & Mechanics, Drexel University, Philadelphia, PA

Research Assistant

Advisor: Peter I. Lelkes, PhD, Cell Tissue Eng. and Regenerative Medicine Lab 2010
School of Biomedical Engineering, Drexel University, Philadelphia, PA

Advisor: Anthony Lowman, PhD, Biomaterials and Drug Delivery Lab 2009
Department of Chemical Engineering, Drexel University, Philadelphia, PA

Advisor: Shelly E. Sakiyama-Elbert, PhD, Cell and Tissue Engineering Lab 2008
Dept. of Biomedical Engineering, Washington University in St. Louis, St. Louis, MO

Advisor: Jennifer H. Elisseeff, PhD, Biomaterials and Tissue Engineering Lab 2005-2009
Dept. of Biomedical Engineering, Johns Hopkins University, Baltimore, MD

Advisor: Wilfredo Colón, PhD 2004
Dept. of Chemistry and Chemical Biology, Rensselaer Polytechnic Institute, Troy, NY

Advisor: Mani A. Daneshmand, MD 2003
Center for Cardiovascular Sciences, Albany Medical College, Albany, NY

PUBLICATIONS (*FIRST AUTHOR)

1. Canver MC, **Canver AC***, Revere K, Amado D, Bennett J, Chung DC. Novel mathematical algorithm for pupillometric data analysis. Computer Methods and Programs in Biomedicine, 2013. **113**(1): 221-5.

2. Salgam A, Perets A, **Canver AC**, Li HL, Kollins K, Cohen G, Fischer I, Lazarovici P, Lelkes PI. Angioneural crosstalk in scaffolds with oriented microchannels for regenerative spinal cord injury repair. Journal of Molecular Neuroscience, 2012. **49**(2): 334-46.

3. Varghese S, Hwang NS, Ferran A, Hillel A, Theprungsirikul P, **Canver AC**, Zhang Z, Gearhart J, Elisseeff J. Engineering musculoskeletal tissues with human embryonic germ cell derivatives. Stem Cells, 2010. **28**(4): 765-74.

4. Varghese S, Hwang NS, **Canver AC**, Theprungsirikul P, Lin DW, Elisseeff JH. Chondroitin sulfate based niches for chondrogenic differentiation of mesenchymal stem cells. Matrix Biology, 2008. **27**(1): 12-21.

5. Hwang NS, Varghese S, Lee HJ, Theprungsirikul P, **Canver AC**, Sharma B, Elisseeff JH. Response to zonal chondrocytes to extracellular matrix-hydrogels. FEBS Letters, 2007. **581**(22): 4172-78.

6. Hwang NS, Varghese S, Theprungsirikul P, **Canver AC**, Elisseeff JH. Enhanced chondrogenic differentiation of murine embryonic stem cells in hydrogels with glucosamine. Biomaterials, 2006. **27**(36): 6015-23.

7. Varghese S, Theprungsirikul P, Ferran A, Hwang NS, **Canver AC**, Elisseeff JH. Chondrogenic differentiation of human embryonic germ cell derived cells in hydrogels. Proceedings of the 28th IEEE, 2006. **1**: 2643-6.

8. Daneshmand MA, Keller RS, Canver MC, **Canver AC**, Canver CC. Histamine H1 and H2 receptor-mediated vasoreactivity of human internal thoracic and radial arteries. Surgery, 2004. **136**(2): 458-63.

ABSTRACTS AND POSTER PRESENTATIONS

1. **Canver AC**, Ngo O, Morss Clyne A. Substrate stiffness impacts endothelial cell collective migration for angiogenesis. 2013 Biomedical Engineering Society Annual Conference; Sept. 25-28, 2013; Seattle, WA.

2. Canver MC, Revere K, Ying GS, **Canver AC**, Bennett J, Chung DC. Impairment of pupillary light responses in murine models of retinal degeneration. Association for Research in Vision and Ophthalmology Annual Conference; May 2-6, 2010; Fort Lauderdale, FL.

3. Canver MC, **Canver AC**, Revere KE, Amado D, Bennett J, Chung DC. Algorithm for pupillometric data analysis. Proceedings of the 36th IEEE Annual Northeast Bioengineering Conference; Mar. 26-28, 2010; New York, NY.

4. **Canver AC**, Johnson PJ, Sakiyama-Elbert SE. Differentiation of embryonic stem cells into functional motor neurons for spinal cord injury. 2008 Biomedical Engineering Society Annual Conference; Oct. 1-4, 2008; St. Louis, MO.

5. **Canver AC**, Johnson PJ, Sakiyama-Elbert SE. Differentiation of embryonic stem cells into functional motor neurons for spinal cord injury. Biomedical Research Fellowship Poster Session; Aug. 1, 2008; St. Louis, MO.

6. Varghese S, **Canver AC**, Theprungsirikul P, Hwang NS, Ferran A, Elisseeff JH. Osteogenic differentiation of human embryonic germ cell derivatives. 2006 Biomedical Engineering Society Annual Conference; Oct. 11-14, 2006; Chicago, IL.

7. **Canver AC**, Varghese S, Hwang NS, Lin DW, Elisseeff JH. Enhanced chondrogenesis of mesenchymal stem cells in chondroitin sulfate-based hydrogels. Howard Hughes Summer Research Fellowship Poster Session; Aug. 3, 2006; Baltimore, MD.
8. Varghese S, Hwang NS, **Canver AC**, Shamblott M, Gearhart J, Elisseeff JH. Musculoskeletal differentiation of embryonic germ cell derived stem cells. 2006 Gordon Research Conference, Musculoskeletal Biology and Bioengineering; Jul. 23-28, 2006; Proctor Academy, Andover, NH.
9. Chung JF, Yang H, Zhang H, **Canver AC**, Breneman C, Colón W. ALS-related misfolding of superoxide dismutase and design of potential therapeutics. Rensselaer Polytechnic Institute Inaugural Day of the Biotechnology Science Center; Sep. 9-10, 2004; Troy, NY.
10. Daneshmand MA, Keller RS, Canver MC, **Canver AC**, Canver CC. Histamine H1 and H2 receptor-mediated vasoreactivity of human internal thoracic and radial arteries. The 62nd Annual Meeting of the Society of University Surgeons; Feb. 8-11, 2004; St. Louis, MO.

TEACHING/MENTORING EXPERIENCE

Teaching Assistant, Department of Computer Science, Drexel University 2014-present

Teaching Assistant, Dept. of Mechanical Engineering & Mechanics, Drexel University 2013
Problem-Based Learning (PBL) Curriculum Workshop – Completed June 2013

Head Resident Assistant
Drexel University 2014-present

Resident Assistant
Drexel University, 1-time RA of the Year 2010-2014
Johns Hopkins University 2007-2009

Teaching Assistant, Department of Computer Science, Johns Hopkins University 2007-2009

MEDICAL EXPERIENCE

Clinical Clerkship, Dept. of Medicine, Abington Memorial Hosp., Abington, PA 2010

Hopkins Emergency Response Organization, Johns Hopkins University 2006-2009

Emergency Department Volunteer, Johns Hopkins Hospital, Baltimore, MD 2006

PROFESSIONAL EXPERIENCE

Institutional Review Board, Review Board Member, Univ. of Pennsylvania 2013-present

Drexel University Graduate Student Association
Webmaster 2014-present
Vice-President of Student Affairs 2013-2014

Drexel University Biomedical Engineering Graduate Association, Webmaster 2012-2013

Medical Device Design Team, Team Leader, Johns Hopkins University 2007-2009

Leader of five-member design team aimed to develop (1) a novel expandable interbody fusion cage for the treatment of vertebral disc disease and (2) a novel non-invasive device to assess left ventricular end diastolic pressure

Biomedical Engineering Society JHU Chapter, President, Johns Hopkins Univ. 2006-2009

Hopkins Undergraduate Research Journal, Editor-in-Chief, Johns Hopkins Univ. 2005-2009

Medical Office Clerk, Tri-City Cardiology, Cohoes, NY Summers 2003-2005

GRANTS/FELLOWSHIPS/SCHOLARSHIPS

Resident Advisor Scholarship, Full Room and Stipend, Drexel University 2010-present

MD/PhD Fellowship, Full Tuition and Stipend, Drexel Univ. Coll. of Medicine 2009-present

Biomedical Research Fellowship, Washington Univ. in St. Louis, St. Louis, MO 2008

$17,000 E-Team Grant, Nat. Coll. Inventors & Innovators Alliance, Hadley, MA 2007-2008

Resident Advisor Scholarship, Full Room and Board, Johns Hopkins University 2007-2009

Howard Hughes Summer Research Fellowship, Johns Hopkins University 2006

Bloomberg Scholarship, Full Tuition, Johns Hopkins University 2005-2009

HONORS/AWARDS

Student Excellence Award for Leadership and Service, Johns Hopkins University 2008

Biomedical Engineering Distinguished Service Award, Johns Hopkins University 2007

SKILLS

Programming: languages (Java, C/C++); MATLAB; web design (CSS/HTML, PHP, SQL, JavaScript); computer-aided design (Pro/Engineer); statistical analysis (SPSS)

Laboratory: sterile 2D and 3D cell culture techniques, tissue sectioning, histological staining, immunofluorescence labeling, polymerase chain reaction, gel electrophoresis, Western blot, light/fluorescent/confocal microscopy, live cell imaging

Applications: Adobe applications (Photoshop, Illustrator, Dreamweaver, Premiere, Acrobat); Microsoft Office (Word, Excel, PowerPoint)

This page was left intentionally blank.